

Laminar burning velocities of methane-hydrogen-air mixtures

Hermanns, R.T.E.

DOI:
[10.6100/IR630126](https://doi.org/10.6100/IR630126)

Published: 01/01/2007

Document Version

Publisher's PDF, also known as Version of Record (includes final page, issue and volume numbers)

Please check the document version of this publication:

- A submitted manuscript is the author's version of the article upon submission and before peer-review. There can be important differences between the submitted version and the official published version of record. People interested in the research are advised to contact the author for the final version of the publication, or visit the DOI to the publisher's website.
- The final author version and the galley proof are versions of the publication after peer review.
- The final published version features the final layout of the paper including the volume, issue and page numbers.

[Link to publication](#)

Citation for published version (APA):

Hermanns, R. T. E. (2007). Laminar burning velocities of methane-hydrogen-air mixtures Eindhoven: Technische Universiteit Eindhoven DOI: 10.6100/IR630126

General rights

Copyright and moral rights for the publications made accessible in the public portal are retained by the authors and/or other copyright owners and it is a condition of accessing publications that users recognise and abide by the legal requirements associated with these rights.

- Users may download and print one copy of any publication from the public portal for the purpose of private study or research.
- You may not further distribute the material or use it for any profit-making activity or commercial gain
- You may freely distribute the URL identifying the publication in the public portal ?

Take down policy

If you believe that this document breaches copyright please contact us providing details, and we will remove access to the work immediately and investigate your claim.

Laminar Burning Velocities of Methane-Hydrogen-Air Mixtures

PROEFSCHRIFT

ter verkrijging van de graad van doctor aan de
Technische Universiteit Eindhoven, op gezag van de
Rector Magnificus, prof.dr.ir. C.J. van Duijn, voor een
commissie aangewezen door het College voor
Promoties in het openbaar te verdedigen
op maandag 22 oktober 2007 om 16.00 uur

door

Roy Theodorus Elisabeth Hermanns

geboren te Beesel

Dit proefschrift is goedgekeurd door de promotor:

prof.dr. L.P.H. de Goey

Copromotor:

dr.ir. R.J.M. Bastiaans

Copyright © 2007 by R.T.E. Hermanns

All rights reserved. No part of this publication may be reproduced, stored in a retrieval system, or transmitted, in any form, or by any means, electronic, mechanical, photocopying, recording, or otherwise, without the prior permission of the author.

Printed by Universal Press, Veenendaal.

A catalogue record is available from the Eindhoven University of Technology Library

ISBN: 978-90-386-1127-3

Voor Marja

Contents

I	Introduction	I
1.1	Background	I
1.2	Laminar Adiabatic Burning Velocity	2
1.3	Scientific Background	4
1.4	Purpose of this Research	6
1.5	Research Tools used in this Thesis	6
1.6	Outline of this Thesis	7
2	Numerical Combustion Modelling	9
2.1	Governing Equations	9
2.2	Combustion Reaction Mechanisms	16
3	Heat Flux Method	21
3.1	Introduction	21
3.2	The Heat Flux Burner	25
3.3	Typical Laminar Burning Velocity Measurement	29
4	Experimental Results	35
4.1	Introduction	35
4.2	Hydrogen-Oxygen-Nitrogen Flames	37
4.3	Methane-Hydrogen-Air Flames	42
4.4	Temperature Dependency of Methane-Hydrogen-Air Flames	51
4.5	Conclusions	56
5	Numerical Results	59
5.1	Introduction	59
5.2	Hydrogen-Oxygen-Nitrogen Flames	60
5.3	Methane-Hydrogen-Air Flames	65
5.4	Methane-Hydrogen-Air Flames at Increased Unburnt Gas Temperatures	73

5.5	Summary	77
6	Asymptotic Theory for Stoichiometric Methane-Hydrogen-Air Flames	79
6.1	Introduction	79
6.2	Analysis of the Asymptotic Structure of Methane-Hydrogen-Air Flames . .	91
6.3	Results and Analysis	97
6.4	Discussion	101
6.5	Conclusions	101
7	Concluding Remarks	103
A	Combustion Reaction Mechanism	107
B	Gas Flow Control	109
B.1	Mass Flow Controller Setpoints	109
B.2	Mass Flow Controller Calibration	110
C	Background of the Heat Flux Method	111
C.1	Freely Propagating Flames	111
C.2	Adiabatic Burner Stabilised Flames	112
D	Temperature of the Burnerplate	115
D.1	Temperature Dependency of the Heat Conductivity	115
D.2	Axial Temperature Dependency	116
E	Tabulated Laminar Burning Velocity Results	119
E.1	Hydrogen-Oxygen-Nitrogen Flames	119
E.2	Methane-Hydrogen-Air Flames	121
E.3	Methane-Hydrogen-Air Flames at Increased Unburnt Temperature	123
	Nomenclature	125
	Bibliography	127
	Abstract	137
	Samenvatting	139
	Curriculum Vitae	141
	Dankwoord	143

Introduction

In this chapter, the topic of the research - laminar burning velocities of methane hydrogen air flames - is introduced. The background of this research is presented in the first part of this chapter. After that an overview of the importance of the laminar burning velocity, is put into a broader scope. In the remaining part of this chapter, the objectives and the approach of the research are shown, followed by an outline of the thesis.

1.1 Background

In a future sustainable energy infrastructure, hydrogen is likely to be an important energy carrier. An advantage of hydrogen in burning situations is that there is no emission of carbon dioxide, as in the case when fossil fuels are burnt. One of the possibilities to contribute to a sustainable environment is by adding hydrogen step-wise to the natural gas infrastructure. Since the natural gas grid in the Netherlands is very well accessible for industry and households, it is an opportunity to contribute in this way to a transition to hydrogen economy. The step-wise addition of hydrogen enables a *gradual* transition from the current fossil-fuel based economy to a future sustainable hydrogen economy. The possibilities of such a step-wise addition are currently studied in the EET-project¹, 'Greening of Gas'. Part of the project research was carried out at the Technische Universiteit Eindhoven, resulting in this thesis. Here we focus on the combustion of natural gas - hydrogen mixtures during the gradual transition from natural gas to hydrogen. More knowledge of this kind of mixtures is needed for a safe transition to natural gas hydrogen mixtures. The combustion of gas mixtures with current burner systems is developed or tuned for a specific natural gas composition, and its typical variations which are likely to occur. Generally, natural gas is a mixture of several hydrocarbon gases like CH₄, C₂H₆ and 'inert' gases like N₂ and CO₂. The

1. The project is funded by 'Economie Ecologie en Technologie' (EET), the Netherlands

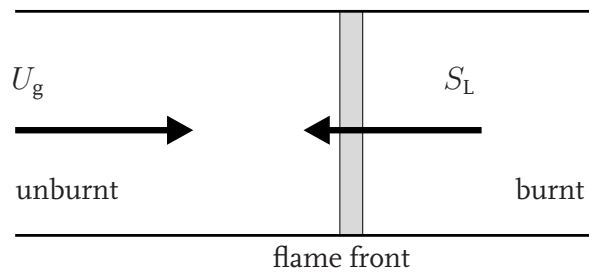


Figure 1.1: Freely propagating one-dimensional adiabatic flame.

main component in 'Groningen natural gas' is methane with an average concentration of 81.3 vol%. For natural gas combustion the design rules for combustion devices are quite clear. However, when adding hydrogen² to the natural gas these consequences are unclear. It is likely that properties related to the safety of burner devices are changed, e.g. ignition delay time, flame blow off and flame flash back. Of course, it is quite laborious to test every single combustion device in the Netherlands. The available devices range from domestic burners, appearing for instance in central heating systems or cookers, to industrial systems, like gas turbines. It ranges from various hydrogen contents of laminar or turbulent systems, and from atmospheric to high pressure systems with preheated gas. The resulting burning properties related to the safety of burner devices have to be known for a broad range. Hence, fundamental knowledge of methane-hydrogen-air burning properties is needed to deliver new data for a safe transition to hydrogen enriched mixtures. Among these burning properties the laminar burning velocity is one of the key parameters. This parameter is elaborated in the next section.

1.2 Laminar Adiabatic Burning Velocity

In this section one of the key parameter in combustion research is addressed: the laminar burning velocity. This section is divided into three parts. In the first part the definition of this laminar burning velocity is introduced. It is followed by an overview of the parameters which can influence and disturb this laminar burning velocity. In the second part the importance of this burning velocity related to the safety and stability of burning devices is addressed briefly. The last part of this section shows that the laminar burning velocity is also relevant for turbulent combustion modelling.

The laminar adiabatic burning velocity is only unambiguously defined in a one-dimensional (1D) situation. In figure 1.1 a freely propagating 1D flame is shown. A fuel-oxidiser mixture enters the system at the unburnt side with velocity U_g . A flame front propagates with velocity S_L in the unburnt mixture. The flame will remain at a fixed position in space only when the gas velocity U_g equals the laminar adiabatic burning velocity S_L exactly. When the heat generated by the chemical reactions is transferred completely to the gas mixture (i.e. there are no heat losses), this flame is called an *adiabatic*

2. In this project the focus is on hydrogen addition, although the problems are similar when adding for example biogas to the natural grid.

flame. In order to determine the laminar adiabatic burning velocity the flame should (ideally) fulfil two requirements:

- 1D, and thus flat and stretchless,
- no heatloss, and thus adiabatic.

Phenomena like flame cooling and flame stretch have an important influence on the burning velocity [66, 74]. For example, to fix the flame at a certain position, a flame is stabilised on a burner, which is only possible when U_g is lower than S_L . This implies heat loss of the flame to the burner and therefore does not represent the adiabatic state anymore. On the other hand flames like free spherical expanding flames, do not stabilise on a burner and can be seen as adiabatic flames. The flame front surface of these spherical flames is increasing in time indicating that the flame front is stretched while expanding, thereby disturbing the flame also. The desired state to measure the laminar adiabatic burning velocity is difficult to accomplish. Only one requirement, either stretchless or adiabatic, is satisfied by most existing measurement methods as can be seen in chapter 3.

The laminar burning velocity for a given gas composition is dependent on the initial conditions of the mixture. In general the initial conditions are the unburnt gas temperature T_u , the fuel equivalence ratio ϕ (the ratio between fuel and oxidiser in the mixture) and the pressure p_u . However, in this thesis the focus is on methane-hydrogen mixtures. As a result an additional property is needed to define the laminar burning velocity which is the amount of hydrogen in the fuel mixture n_{H_2} . This indicates that S_L used in this thesis is a function of the initial properties:

$$S_L = f(\phi, n_{H_2}, T_u, p_u). \quad (1.1)$$

The laminar burning velocity is an important property for several reasons, some of them will be addressed in the remaining part of this section.

Knowledge of the laminar burning velocity becomes important in the trade-off between combustion stability and pollutant emissions. For example at very fuel lean conditions the laminar burning velocity decreases sharply and the flame is becoming less stable due to the partial or complete quenching (blow-out) of flames. This affects the emissions of carbon-monoxide and unburnt hydrocarbons. Hence, in lean premixed combustion a choice has to be made, in determining how lean one should operate. There is a trade-off between low pollutant emissions by operating at very lean conditions and a higher power output at slightly richer conditions. A higher power output gives more carbon monoxide and unburnt hydrocarbon emissions by avoiding flame quenching. Also related to the stability of flames is the so-called flash back phenomenon. In combustion systems flash back is a dangerous aspect which can for example occur when operating a system in a modulated manner, e.g. by changing the equivalence ratio, altering fuel composition or preheating of the fuel. By modulating the burner in this way the laminar burning velocity can vary significantly. This can result in a situation where the laminar burning velocity becomes substantial smaller than the unburnt gas velocity and blow-off can occur.

The laminar burning velocity is also an important parameter in turbulent combustion modelling. Often turbulence models assume that combustion takes place in the so-called flamelet regime [81]. Such flames can be considered as a front which is locally propagating as a stretched laminar flame. This flame stretching due to turbulence increases the

flame surface which results in an increase of the (turbulent) burning velocity. For very low turbulent velocities the ratio between turbulent and laminar burning velocities S_t/S_L increases almost linearly with the ratio u'/S_L [59]. For stronger turbulence and thus higher u' the turbulent burning velocity S_t increases less fast with u' or can even decrease [59]. This can be explained by increased flame quenching of the flame due to locally highly stretched flames. Here, the production of flame surface is competing with local flame quenching. This different behaviour at various turbulence intensities demands for different modelling approaches. However, Lipatnikov and Chomiak [70] showed in a comprehensive evaluation of turbulent premixed combustion models that the laminar burning velocity is commonly considered as an essential parameter characterising the turbulent burning velocity.

1.3 Scientific Background

This section gives an overview of the current status of the research on laminar burning velocities of methane-hydrogen-air mixtures. This overview is divided into three parts. In the first part experiments available in literature are briefly discussed. The second part gives the current status of combustion reaction mechanisms regarding hydrogen enriched methane-air mixtures. The last part describes a short overview of the modelling of flame properties.

Experiments

During the last decades significant progress is achieved in the understanding of methane as well as hydrogen flames. This is accomplished by improving the experimental methods, flame models and combustion reaction mechanisms to determine flame properties, like species concentration profiles and ignition delay times. While the combustion characteristics of *pure* mixtures of methane-air and hydrogen-air have been extensively studied over the years, the knowledge regarding the combustion of mixtures containing both methane *and* hydrogen is limited. The existing experimental flame studies on the effect of hydrogen addition to natural gas or methane are mainly restricted to ignition delay measurements or quantification of emissions, see Fotache et al. [32], Fukutani and Kunioshi [34], Lifshitz et al. [69], Karim et al. [57], Bell and Gupta [5]. Several authors measured the laminar burning velocity in the past, e.g. Haniff et al. [43], Yu et al. [116] and recently Halter et al. [42] and Huang et al. [52]. However, these measurements (as will be shown in this thesis) show a rather large scatter so therefore accurate measurements are needed to determine more accurate laminar burning velocities for different hydrogen contents in methane. A similar kind of scatter in the data was found earlier in the eighties for methane-air flames, where the experimental results of the maximum laminar burning velocity varied roughly between 34 cm/s and 45 cm/s. Nowadays, experimental results reveal a value of 36 ± 1 cm/s as the maximum laminar burning velocity of methane-air flames.

Experimental data available in literature are often determined at ambient conditions. In gas turbines however conditions are different: increased unburnt gas temperature and

increased pressure. Measurements of laminar burning velocities at situations relevant for gas turbine conditions can be found in literature for methane-air [25, 39, 42, 45, 54] or hydrogen-air mixtures [26, 54, 107]. However, the mixtures considered here, hydrogen enriched methane-air, show some lack of data. Halter et al. [42] presented recently laminar burning velocities at increased pressures. Measurements at increased unburnt temperature are available from several authors however only for pure methane-air mixtures or pure hydrogen-air mixtures.

Combustion Reaction Mechanisms

Correct predictions with reliable combustion reaction mechanisms are suitable to assist studies in order to make a safe transition to a future hydrogen economy possible. Over the years several reaction mechanisms have been developed for methane-air combustion, e.g. GRI-mech [11, 97], Konnov's mechanism [60], and the Leeds methane oxidation mechanism [53]. However, in recent studies [61] it became clear that the frequent extensions and adaptations of the existing reaction mechanisms for more complex fuels resulted in a decreasing accuracy of the hydrogen-oxidation sub-mechanism. This introduced a renewed interest in this important sub-mechanism, which can be denoted as the core of all oxidation reaction mechanisms [110]. The majority of the methane-air combustion reaction mechanisms has not yet been adapted to these new insights and it might be that these complex mechanisms are not able to predict proper flame behaviour when a significant amount of hydrogen is added to the mixture. New data will be needed to validate these mechanisms. One option is to perform new experiments to determine the laminar burning velocity. This property is widely used to validate combustion reaction mechanisms.

Models

As a consequence of the considerable amount of progress in the knowledge of combustion kinetics, the numerical computation of flames with detailed kinetics has become common [109]. Some combustion reaction mechanisms with *complete* kinetics include even more than a few hundred species and several thousands of elementary reactions. However, this enormous amount of information which becomes available is of little use to the understanding of the fundamental parameters that influence the basic flame behaviour. A clear description of the basic flame structure explaining for example the increase in burning velocity when adding hydrogen, is not available. However, in the case of pure methane or pure hydrogen combustion the situation is different, here several models have been developed to gain more insight concerning the basic flame structure of these flames. For example Evans [30] gives an extensive review of the classical laminar flame models. More recent models are for example the asymptotic theory of Peters and Williams for methane-air flames [82] and a model developed by Seshadri, Peters and Williams [94] for pure hydrogen flames. Both models start from a detailed reaction mechanism and reduce this mechanism systematically to a simplified one by trying not to lose too much information regarding the fundamental flame properties. Göttgens et al. [38] used another approach and provided analytical expressions for the burning velocity and flame thickness of hydrogen and methane flames. In order to get

an adequate physical insight in the behaviour when hydrogen is added to methane, these kind of models should be adapted to methane-hydrogen mixtures.

1.4 Purpose of this Research

When hydrogen is added to the Dutch natural gas grid influences the behaviour of combustion devices will be affected. In order to make a safe transition to a hydrogen based energy economy more knowledge of methane-hydrogen-air mixtures is needed. Proper design and operation of practical combustors requires that key flame properties, such as the laminar burning velocity, are well known under the applied combustion conditions. The objectives of this research are:

- Deliver accurate experimental laminar burning velocity data;
- Validate numerical reaction mechanisms using the laminar burning velocity data;
- Gain more insight in the effects which affect key flame properties like laminar burning velocity, flame temperatures, flame thickness when adding hydrogen to a methane-air mixture;

1.5 Research Tools used in this Thesis

Throughout this thesis three main research tools will be used. One is an experimental method to determine the laminar burning velocities accurately: the heat flux method. The data measured with this heat flux method, will be used to validate combustion reaction mechanisms. This is done by using the second tool: a numerical 1D flame code called CHEM1D. This code is developed to determine flame properties like the laminar burning velocity by using combustion reaction mechanisms. The third tool is an asymptotic theory which will be used to describe the basic phenomena occurring when applying hydrogen enrichment to methane-air flames. These three tools, - an experimental, numerical and theoretical one - will be explained in detail in this thesis. They will be used to determine laminar burning velocities over a wide range of settings.

Investigated Parameter Range

Firstly pure hydrogen flames at ambient conditions will be investigated. However, in these flames the oxygen content is artificially lowered to about 10 mol% in order to reduce the laminar burning velocities to gas velocities which can be used with the heat flux method. Secondly, the burning velocities of hydrogen enriched methane-air flames are investigated at ambient conditions. The equivalence ratio is varied between $\phi \approx 0.6$ and 1.5. The hydrogen enrichment is set at 0, 10, 20, 30 and 40 mol% in the fuel. Finally, we address the laminar burning velocities of methane-hydrogen-air flames with increased unburnt gas temperatures for flames with an equivalence ratio of 0.8, 1.0 and 1.2. for a hydrogen enrichment 0, 10, 20 and 30 mol% of hydrogen addition to the fuel is not determined with the heat flux method. The unburnt gas temperature is varied between 298 and 450

K. The laminar burning velocity data for the mentioned unburnt gas temperatures are determined experimentally. Numerically the laminar burning velocity analysis is extended to more or less gas turbine conditions ($T_u \approx 500$ K). Since the asymptotic theory is only valid for stoichiometric flames these flames are only taken into account in the corresponding parts of this thesis.

1.6 Outline of this Thesis

The next chapter provides some background information about the equations which govern the flames of interest. Also in this chapter the CHEM1D numerical flame code [16] is introduced. This code will be used to determine flame properties with several numerical combustion reaction mechanisms, e.g. GRI-mech 3.0 [97]. The chapter concludes with an overview of some commonly used combustion reaction mechanisms. Based on this overview a set of reaction mechanisms is selected. This set will be used in the rest of this thesis: the experiments performed with the heat flux burner will be compared with these combustion reaction mechanisms. The experimental setup used in this thesis is presented in chapter 3. This setup is used to determine laminar burning velocities of methane-hydrogen-air mixtures and hydrogen-oxygen-nitrogen mixtures using the heat flux method. In chapter 3 the background of this method is explained, including error-estimates and an overview of the reproducibility of the measurements. Furthermore, this chapter presents a brief summary of some other experimental methods for determining laminar burning velocities. This serves as a basis when comparing the determined heat flux results in chapter 4 with data of other authors. In chapter 5, the heat flux data presented in the previous chapter, are compared with results obtained for several combustion reaction mechanisms calculated using the package CHEM1D. These latter two chapters show new experimental data of laminar burning velocities for hydrogen enriched methane-air flames and an overview of the performance of recently introduced combustion reaction mechanisms. In chapter 6 an asymptotic theory for methane-hydrogen-air flames is introduced. This theory will be used to describe and explain the change of burning velocity when adding hydrogen to a methane-air mixture and can give information on the mechanism that causes the changes. Finally, in chapter 7 the conclusions and discussion are presented.

Numerical Combustion Modelling

The relations characterising reactive flow systems are formulated in this chapter. Chemically reacting flows are governed by a set of equations describing the conservation of mass, momentum, energy and chemical components. In the end these equations are written in the form in which they are implemented in the 1D flamecode CHEM1D. Finally, the last part of this chapter gives an overview of combustion reaction mechanisms which are capable to describe flame properties of methane-hydrogen-air mixtures is given. From these reaction mechanisms a subset is selected which is used in the rest of this thesis.

2.1 Governing Equations

This section deals with the governing equations concerning the combustion of gases. Besides this, the governing equations will be used in the next chapter to explain the heat flux method and they are used in chapter 6 as a basis for the analysis of the asymptotic structure of methane-hydrogen-air flames. The governing equations for modelling reactive flow systems are derived in many books, e.g. [64, 85, 110, 113]. Here, in the first subsection a general set of conservation equations of mass, momentum, species mass fractions and enthalpy is introduced. Subsequently state equations for specific enthalpy and density are presented; followed by transport and chemistry models.

2.1.1 General Conservation Equations

The conservation of mass is expressed by the general continuity equation,

$$\frac{\partial \rho}{\partial t} + \nabla \cdot (\rho \mathbf{u}) = 0, \quad (2.1)$$

where ρ is the mixture mass density and $\mathbf{u} = (u, v, w)^T$ the gas mixture velocity. The conservation of momentum, with no body forces other than gravity, is covered by

$$\frac{\partial \rho \mathbf{u}}{\partial t} + \nabla \cdot (\rho \mathbf{u} \mathbf{u}) = \nabla \cdot \mathbf{\Pi} + \rho \mathbf{g}, \quad (2.2)$$

where $\mathbf{\Pi}$ is the stress-tensor, and \mathbf{g} the acceleration due to gravity. The stress-tensor consists of a hydrodynamic and viscous part: $\mathbf{\Pi} = -p\mathbf{I} + \boldsymbol{\tau}$ in which p is the pressure, \mathbf{I} the unit tensor and $\boldsymbol{\tau}$ the viscous stress-tensor.

The equation describing the conservation of energy is written in terms of specific enthalpy h ,

$$\frac{\partial \rho h}{\partial t} + \nabla \cdot (\rho \mathbf{u} h) = \frac{\partial p}{\partial t} + \mathbf{u} \cdot \nabla p + \boldsymbol{\tau} : (\nabla \mathbf{u}) - \nabla \cdot \mathbf{q}, \quad (2.3)$$

with \mathbf{q} the total heat flux. The term $\boldsymbol{\tau} : (\nabla \mathbf{u})$ represents the enthalpy production due to viscous effects.

When chemical reactions are to be considered, conservation equations for the species mass fractions Y_i are used. They are defined as $Y_i = \rho_i / \rho$ with ρ_i the density of species i . The density of the mixture ρ is related to the density of the various species by $\rho = \sum_{i=1}^{N_s} \rho_i$, with N_s the number of species. This leads to a conservation equation for every species mass fraction in the mixture,

$$\frac{\partial \rho Y_i}{\partial t} + \nabla \cdot (\rho \mathbf{u} Y_i) + \nabla \cdot (\rho \mathbf{U}_i Y_i) = \dot{\omega}_i, \quad i \in [1, N_s], \quad (2.4)$$

with \mathbf{U}_i is the diffusion velocity of species i . The chemical source term $\dot{\omega}_i$ in this equation, is characteristic for the reactive nature of the flow. Note that equation (2.4) together with the continuity equation equation (2.1) gives an over-complete system, so instead of N_s only $N_s - 1$ equations in (2.4) have to be solved. The mass fraction of one of the species can be computed using the following constraint:

$$\sum_{i=1}^{N_s} Y_i = 1. \quad (2.5)$$

An abundant species, e.g. nitrogen, is commonly chosen for this species. By definition chemical reactions are mass conserving, so therefore the following relations hold:

$$\sum_{i=1}^{N_s} \rho Y_i \mathbf{U}_i = 0, \quad \text{and} \quad \sum_{i=1}^{N_s} \dot{\omega}_i = 0. \quad (2.6)$$

Finally, state equations are needed to complete the set of differential equations (2.2)-(2.4). The first state equation introduces the specific enthalpy h as a function of temperature T . This relation is given by

$$h = \sum_{i=1}^{N_s} Y_i h_i, \quad \text{with} \quad h_i = h_i^{\text{ref}} + \int_{T^{\text{ref}}}^T c_{p_i}(T) dT, \quad (2.7)$$

and holds for perfect gases. In this equation h_i represents the enthalpy of species i and h_i^{ref} the formation enthalpy of species i at a reference value for the temperature T^{ref} and

c_{p_i} the specific heat capacity at constant pressure of species i . The mixture heat capacity is defined by

$$c_p = \sum_{i=1}^{N_s} Y_i c_{p_i}. \quad (2.8)$$

The species heat capacity c_{p_i} is commonly tabulated in polynomial form [14]. In most combustion problems the mixture and its components are considered to behave as perfect gases. The ideal-gas law relates the density, temperature and pressure to each other by

$$\rho = \frac{p\bar{M}}{RT}, \quad (2.9)$$

with R the universal gas constant and \bar{M} the mean molar mass. This \bar{M} can be determined from

$$\bar{M} = \left(\sum_{i=1}^{N_s} \frac{Y_i}{M_i} \right)^{-1}, \quad (2.10)$$

where M_i is the molar mass of species i .

Summarising: a set of $N_s + 7$ equations is needed, being the conservation equations of mass (2.1), momentum (2.2) and enthalpy (2.3), a mass balance for every species (2.4), and two state equations, ((2.7) and (2.9)). This set of equations describes the evaluation of $N_s + 7$ variables: $\rho, \mathbf{u}, p, T, h$ and N_s species mass fractions Y_i . In order to solve this set of differential equations additional expressions are required for $\boldsymbol{\tau}, \mathbf{q}, \mathbf{U}_i$ and $\dot{\omega}_i$. In the next subsection expressions and models for almost all properties are presented only the expression for $\dot{\omega}_i$ is given in 2.1.3.

2.1.2 Molecular Transport Fluxes

Characterising the molecular transport of species, momentum and energy in a multi-component gaseous mixture requires the evaluation of diffusion coefficients, viscosity's, thermal conductivities and thermal diffusion coefficients. The kinetic theory does not provide explicit expressions [28] for the transport coefficients. To obtain these coefficients for detailed transport models a large linear system of equations has to be solved [28]. Solving this system can be CPU extensive. Depending on the use of the results it is often advantageous to make simplifications to reduce the computational costs. Examples of these simplifications are the constant Lewis numbers approximation for diffusion and Wilke's approximation [111] for the approximation of viscosity. Unless otherwise mentioned in this thesis detailed transport equations [6, 51] are used to solve the multi-component species properties.

Starting with the viscous stress tensor $\boldsymbol{\tau}$ which is determined from the kinetic gas theory, derived for example by Hirschfelder et al. [51], and is given by

$$\boldsymbol{\tau} = \left(\kappa - \frac{2}{3}\eta \right) (\nabla \cdot \mathbf{u}) \mathbf{I} - \eta (\nabla \mathbf{u} + (\nabla \mathbf{u})^T), \quad (2.11)$$

where η is the mean dynamic viscosity of the mixture and κ the volumetric viscosity. Generally, the volume viscosity is neglected in flame simulations [110].

The heat flux vector \mathbf{q} , e.g. [64, 110, 113], is given by

$$\mathbf{q} = -\lambda' \nabla T + \rho \sum_{i=1}^{N_s} \mathbf{U}_i Y_i h_i - p \sum_{i=1}^{N_s} D_i^T \mathbf{d}_i + \mathbf{q}_R, \quad (2.12)$$

where the first term of this equation represents the conduction term represented by the thermal conductivity λ' and the temperature gradient, the second term represents transport of energy by mass diffusion, the last term \mathbf{q}_R is the gas radiative heat flux vector. The term with the D_i^T represents the so called Dufour effect (change in temperature due to a species gradients). The vector \mathbf{d}_i incorporates the effects of various gradients and external forces [113] and can be expressed as:

$$\mathbf{d}_i = \nabla X_i + (X_i - Y_i) \frac{\nabla p}{p} + \frac{\rho}{p} \sum_{k=1}^{N_s} Y_i Y_k (\mathbf{b}_k - \mathbf{b}_i), \quad i \in [1, N_s], \quad (2.13)$$

with $X_i = Y_i \bar{M} / M_i$ the mole fraction of species i , D_{ik} the multi-component diffusion coefficients, D_i^T the thermal diffusion coefficients, \mathbf{b}_i the body force on a molecule. This body force per unit mass is often assumed the same for each species and the last term in the previous equation becomes zero.

To be able to solve the conservation equations an expression for the flux term \mathbf{U}_i is needed. Following from the kinetic theory of gases, see e.g. [6, 28, 51], \mathbf{U}_i is given by

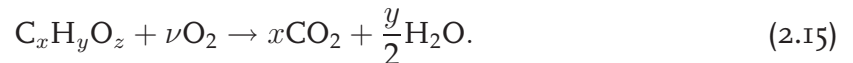
$$\mathbf{U}_i = - \sum_{k=1}^{N_s} D_{ik} \mathbf{d}_i - D_i^T \frac{\nabla T}{T}, \quad i \in [1, N_s], \quad (2.14)$$

The term with the thermal diffusion coefficient in equation (2.14) is known as the Soret-effect (or the thermal diffusion effect). This term describes the effect that due to a temperature gradient lighter species tend to go to parts of the flame where the temperature is higher; whereas heavier species tend to go to colder parts of the flame [112].

In this thesis the diffusion coefficient D_{ik} , the thermal diffusion coefficient D_i^T , the shear viscosity η and the partial thermal conductivity λ' are tabulated. The equations (2.11)-(2.14) are solved with the EGLIB library [29]. This transport library uses the method proposed by Ern and Giovangigli [28, 29] to solve this set of equations in an efficient manner.

2.1.3 Combustion Chemistry

At the start of this section the reactive flow equations have been introduced. An essential property in reactive flows is the chemical source term. This source term $\dot{\omega}_i$ appearing in the species balance equation (2.4) is not specified yet. It describes the rate of change of a chemical component due to chemical reactions. Sometimes the complete conversion of hydrocarbons into reactants is presented by a global reaction in molar form, and can be written as



Here ν is the stoichiometric fraction, $\nu = x + y/4 - z/2$, indicating the number of moles of oxygen are needed for a complete conversion of one mole of hydrocarbons into

products: carbon-dioxide and water. This global reaction only predicts the major species. Generally, in a combustion process various intermediate species are formed. To be able to predict these species in a flame the global reaction is build up from a large number of intermediate steps, also known as elementary reactions. Each elementary reaction can be written as,

$$\sum_{i=1}^{N_s} \nu'_{ij} \mathcal{A}_i \rightleftharpoons \sum_{i=1}^{N_s} \nu''_{ij} \mathcal{A}_i, \quad j \in [1, N_r] \quad (2.16)$$

with N_r the number of (elementary) reactions and \mathcal{A}_i a chemical component i , e.g. CH_4 , H_2O or HCN . Furthermore, ν'_{ij} and ν''_{ij} denote the number of molecules of type i that are consumed and produced with the elementary reaction j . A typical elementary reaction is the reaction of hydroxy radicals (OH) with molecular hydrogen (H_2) forming water (H_2O) and hydrogen atoms (H),



This reaction is considered a forward one as indicated by the arrow. The corresponding reaction rate representing this reaction $r_{j,f}$ is proportional to the concentration of the reactants,

$$r_{j,f} = k_{j,f} \prod_{i=1}^{N_s} n_i^{\nu'_{ij}}, \quad (2.18)$$

with the concentration $n_i = \rho Y_i / M_i$ of species i and $k_{j,f}$ the reaction coefficient of reaction j . The subscript f indicates that the forward reaction is considered. The reaction rate coefficient is usually written in Arrhenius form [110],

$$k_{j,f} = AT^b \exp(-E_a/RT), \quad (2.19)$$

with A and b reaction constants and E_a the activation energy. In general the species may also react in the opposite direction,



Now, the rate of change of this reverse reaction can be determined analogous to the forward reaction rate. The resulting overall reaction rate for reaction j is given by

$$r_j = r_{j,f} - r_{j,b} = k_{j,f} \prod_{i=1}^{N_s} n_i^{\nu'_{ij}} - k_{j,b} \prod_{i=1}^{N_s} n_i^{\nu''_{ij}}, \quad j \in [1, N_r]. \quad (2.21)$$

The reaction rate of the backward reaction $k_{j,b}$ can be obtained using the equilibrium constant $k_{j,\text{eq}}(p, T) = k_{j,f}/k_{j,b}$, which is well defined by the thermodynamic properties of the chemical components that are involved in this reaction [102]. Finally the chemical source term of species i is given by

$$\dot{\omega}_i = M_i \sum_{j=1}^{N_r} (\nu''_{ij} - \nu'_{ij}) r_j, \quad i \in [1, N_s], \quad (2.22)$$

Now the chemical source term can be evaluated for every reaction when the reactions and their reaction rate constants A, b and E_a are known in equation (2.19) and (2.21).

These constants are commonly listed in so-called combustion reaction mechanisms. An example of such a mechanism is shown in Appendix A. Several research groups provide reaction mechanisms for natural gas or hydrogen gas combustion, e.g. [11, 61, 97]. In this research recent methane combustion reaction mechanisms are used which describe several hundreds of elementary reactions using typically 50 species. In section 2.2 some combustion mechanisms are discussed briefly. The governing equations which are used in this thesis are formulated in their final form in the remaining part of this section.

2.1.4 Equations Used in the Remainder of this Thesis

The equations presented in the previous sections are put into a 1D formulation and simplified with a commonly used combustion approximation for low Mach number reactive flows [13]. In this thesis the typical gas velocities considered are much smaller than the speed of sound. Typical Mach numbers in the unburnt mixture for the investigated laminar flames are $Ma_u = S_L/c = \mathcal{O}(10^{-3})$, with c the speed of sound. By integrating the momentum equation (2.2), from unburnt to burnt mixture (neglecting gravity and viscosity) and using $c = \sqrt{(c_p/c_v)p/\rho}$ for the speed of sound, the following relation is found:

$$\frac{p_u - p_b}{p_u} = \frac{c_p}{c_v} \left(\frac{\rho_u}{\rho_b} \right) Ma_u^2, \quad (2.23)$$

with c_v the specific heat capacity at constant volume. The subscripts u and b refer to the unburnt and burnt mixture respectively. To estimate the pressure drop over the flame $c_p/c_v \approx 1.3$ and $\rho_u/\rho_b \approx 7$ are used, resulting in $(p_u - p_b)/p_u = \mathcal{O}(10^{-5})$ for the weak deflagration flames investigated in this thesis. Clearly, only a small error is made when replacing the spatial pressure p in equation (2.9) with the ambient pressure p_0 . Equation (2.9) then becomes,

$$\rho = \frac{p_0 \bar{M}}{RT}. \quad (2.24)$$

Hence, the pressure in the energy equation (2.3) can be treated as spatially constant. The energy dissipation by viscous forces in the energy equation (2.3) can be neglected as well [64]. As a consequence the governing equations can be simplified by omitting the momentum equation (2.2).

The 1D flat flames investigated in the present research are stationary flames, which means that the terms involving the $\partial/\partial t$ are zero. So the conservation equations which will be used in the remainder of this thesis become:

$$\frac{\partial}{\partial x} (\rho u) = 0, \quad (2.25)$$

$$\frac{\partial}{\partial x} (\rho u h) = \frac{\partial}{\partial x} \left(\frac{\lambda'}{c_p} \frac{\partial h}{\partial x} \right) - \frac{\partial}{\partial x} \left(\rho \sum_{i=1}^{N_s} U_i Y_i h_i \right) + \frac{\partial}{\partial x} \left(p \sum_{i=1}^{N_s} D_i^T d_i \right), \quad (2.26)$$

$$\frac{\partial}{\partial x} (\rho u Y_i) + \frac{\partial}{\partial x} (\rho U_i Y_i) = \dot{\omega}_i, \quad i \in [1, N_s - 1], \quad (2.27)$$

This system of conservation equations uses the equations (2.7), (2.8), (2.10), (2.24) and (2.22) to determine the enthalpy, specific heat capacity, mean molar mass, density and

chemical source, respectively. The fluxes are determined with the equations mentioned in subsection 2.1.2. The system is closed with the constraints:

$$\begin{aligned} Y_{N_s} &= 1 - \sum_{i=1}^{N_s-1} Y_i, \\ \sum_{i=1}^{N_s} \rho Y_i U_i &= 0, \\ \sum_{i=1}^{N_s} \dot{\omega}_i &= 0. \end{aligned} \quad (2.28)$$

The obvious choice for this N_s species is the one that is present in abundance; in our case this is nitrogen. Note that the flame properties solved with CHEM1D are determined with both the Dufour effect (in the heat flux vector of equation (2.12)) and the Soret effect (in equation (2.14)) taken into account.

Computational Strategy

The computational strategy to solve the differential equations (2.25) - (2.27) is addressed here. CHEM1D uses an exponential finite volume discretisation in space and the nonlinear differential equations are solved with a fully implicit, modified Newton method [100]. There are fundamentally two mathematical approaches for solving this set of differential equations to determine the laminar burning velocity. One uses a transient method and the other solves the steady-state boundary value problem directly. The transient method is time consuming and not used unless otherwise mentioned. The steady-state boundary value method uses a frame of reference which is moving equally to the laminar burning velocity by fixing the temperature at a certain spatial coordinate. Now, the mass flow rate ρu is a variable instead of a given parameter and the mass flow rate becomes an eigenvalue of the set of differential equations. The resulting mass flow rate equals the mass flow rate of an laminar adiabatic flame, resulting in $\rho_u u_u = \rho_u S_L$. This procedure is introduced by Smooke et al. [99] and implemented in CHEM1D. An adaptive gridding procedure is also implemented to increase accuracy in the flame front [100]. This adaptive gridding places most ($\approx 80\%$) of the gridpoints in the area with the largest gradients (flame front). To solve the set of differential equations boundary conditions for species and enthalpy have been used at the unburnt and burnt side of the flame. At the unburnt side a Dirichlet type of boundary condition is used:

$$\begin{aligned} x = -\infty : \quad & h = h_u \\ & Y_i = Y_{i,u}, \end{aligned} \quad (2.29)$$

whereas at the burnt side Neumann type boundary conditions are used:

$$\begin{aligned} x = \infty : \quad & \frac{\partial h}{\partial x} = 0 \\ & \frac{\partial Y_i}{\partial x} = 0. \end{aligned} \quad (2.30)$$

Typical domain dimensions for methane-hydrogen-air flames are from $x = -2$ to 10 cm and 300 gridpoints. For hydrogen-oxygen-nitrogen flames the domain is taken smaller,

typically from $x = -1$ to $x = 5$ cm and using 300 gridpoints, because of the thinner flames and steeper gradients occurring in this kind of flames. This number of gridpoints is suitable enough to have a stable converged solution when using the exponential discretisation scheme.

2.2 Combustion Reaction Mechanisms

In order to determine 1D flame properties, like the laminar burning velocity, with the package CHEM1D a combustion reaction mechanism for a given set of species is required. In literature several combustion reaction mechanisms can be found, often developed for specific situations, e.g. hydrogen flames, ignition phenomena or diffusion flames. In this section several combustion mechanisms (post-2000 work) are discussed briefly concerning their main focus, working range and expected performance for laminar burning velocities. From this set of reaction mechanisms a few will be selected for further investigation in this thesis.

In literature several status reviews of detailed chemical kinetic models can be found. A recent one by Simmie [95] shows that the investigated chemical models give more or less similar results for ignition delay times. However, it is noteworthy to mention that many of the important reactions differ significantly between the mechanisms. Simmie concluded that the oxidation chemistry of a 'simple' fuel like hydrogen and carbon monoxide is still not well characterised. The chemistry which involves the hydrogen oxidation mechanism is known as the core of any detailed hydrocarbon combustion reaction mechanisms [108]. However, these contemporary hydrogen-oxidation mechanisms used by various authors differ by the number of species and reactions involved and their rate constants. Baulch et al. [4] suggested a complete set of relevant reactions for the chemistry involving hydrogen oxidation. It turned out that this review provided a basis for the modelling of laminar burning velocities of hydrogen-air, hydrogen-carbon monoxide-air and methane-air flames. Substantial progress has been made during the last decades in the accuracy of the measurements, not only for elementary reaction rates, but also a recently presented reexamination of a hydrogen-carbon monoxide combustion mechanism by Davis et al. [19]. They suggested new kinetic parameters for the important reaction $\text{H} + \text{O}_2 + \text{M} = \text{HO}_2 + \text{M}$. Additionally the new value of the thermodynamic data for the OH radical strongly suggested by Ruscic et al. [88], Joens [56] and Herbon et al. [47], was taken into account, resulting in a renewed interest in this hydrogen-oxidation mechanism. In 2004 several improved *comprehensive* hydrogen oxygen combustion mechanisms were introduced, e.g. Konnov [61], Ó Conaire et al. [78] and Li et al. [68].

The mechanism of Konnov [61], involving 10 species and 31 reactions, was validated with ignition experiments, hydrogen oxidation in flow reactors experiments and burning velocities of hydrogen-oxygen-inert mixtures at pressures from 0.35 to 4 atm. Also Ó Conaire et al. [78] proposed recently a new mechanism which takes its origin from Mueller et al. [77]. This Ó Conaire mechanism, which consists of 9 species and 21 reactions, is developed to simulate hydrogen combustion over a wide range. Ignition delay times, laminar burning velocities and species concentrations were taken into account [78]. The series of experiments numerically investigated ranged from 298 to

2700 K and pressure from 0.05 to 87 atm and the equivalence ratios from 0.2 to 6. The new mechanism of Li et al. [68] is also based on the earlier work of Mueller et al. [77]. The mechanism of Li et al. with 11 species and 19 reactions, was compared against a wide range of experimental conditions (298 - 3000 K, 0.3 - 87 atm, $\phi = 0.25 - 5.0$) including laminar burning velocities, shock tube, ignition delay time and species profiles.

Table 2.1: Laminar burning velocities of stoichiometric hydrogen-air mixtures at ambient conditions of several hydrogen-oxidation combustion reaction mechanisms.

Mechanism	Year	N_s	N_r	S_L (cm/s)
Ó Conaire [78]	2004	9	21	203.06
Konnov [61]	2004	10	31	208.15
Li [68]	2004	11	19	206.26

Results of laminar burning velocities of stoichiometric hydrogen-air flames are shown in table 2.1. These velocities have been determined with CHEM1D using the before mentioned hydrogen combustion reaction mechanisms. Also in the table the year the mechanism is introduced is given together with the number of species and reactions in the mechanism.

Recently Petrova and Williams [83] and Dagaut and Nicolle [18] presented their mechanisms for hydrocarbon combustion and adapted the new insights of the hydrogen chemistry (thermodynamic data of OH and new kinetic parameters [19, 47, 56, 88]) for their mechanism. However, in most of the well known methane-air mechanisms these new insight still have to be implemented. The San Diego 2005 mechanism published by Petrova and Williams [83], consisting of 37 species and 177 reaction steps, is designed to be used for autoignition, deflagrations, detonations and diffusion flames of a number of hydrocarbon fuels. This San Diego 2005 mechanism, is restricted for pressures below 100 atm and temperatures above 1000 K and fuel equivalence ratios less than about 3 for premixed systems. Dagaut and Nicolle [18] presented a mechanism of hydrocarbon oxidation from natural gas to kerosene and diesel fuels. One motivation of their research was focused on the effect of hydrogen-enriched natural gas blend oxidation, which is also the main topic of this thesis. However, their mechanism was experimentally validated mainly in a jet-stirred reactor, so the performance of their mechanism for laminar burning velocities has to be seen.

Konnov [60] presented a comprehensive mechanism for methane combustion with 127 species and 1207 reactions including C2, C3 hydrocarbons and NO_x formation in flames. It is extensively validated against a large set of experiments including species profiles, laminar burning velocities and ignition delay times in shock waves. The Gas Research Institute updated their mechanism [97] in the year 2000 to version GRI-mech 3.0 consisting of 53 species and 325 elementary reactions. It differs from the previous release GRI-mech 2.11 [11] in that kinetics and target data have been updated, improved, and expanded. Propane and C2 oxidation products have been added, and new formaldehyde and NO formation and reburn targets included. The conditions for which

Table 2.2: Laminar burning velocities of stoichiometric methane-air and hydrogen-air mixtures at ambient conditions of several combustion reaction mechanisms with methane-oxidation included.

Mechanism	Year	N_s	N_r	S_{L,CH_4} (cm/s)	S_{L,H_2} (cm/s)
Smooke [98]	1991	16	25	36.16	233.46
GRI-mech 3.0 [97]	2000	53	325	36.37	211.49
Konnov 0.5 [60]	2000	127	1207	33.96	-
Leeds 1.5 [53]	2001	37	174	36.99	203.64
SKGo3 [96]	2004	73	520	36.79	215.92
GDF-kin [®] [27]	2004	121	883	36.31	214.68
Dagaut [18]	2005	99	735	33.95	203.34
San Diego 2005 [83]	2005	37	177	33.50	208.06

GRI-Mech 3.0 was optimised, limited primarily by availability of reliable optimisation targets, are roughly 1000 to 2500 K, 10 Torr to 10 atm, and equivalence ratios from 0.1 to 5 for premixed systems. It is validated using e.g. ignition experiments, shock-tube species profile measurements and laminar burning velocities. The Leeds mechanism presented by Hughes et al. [53], which is introduced in 2001, describes the oxidation kinetics of hydrogen, carbon-monoxide, methane and ethane in flames. This Leeds mechanism (version 1.5) consisting of 37 species and 175 reactions is validated more or less using the same set of experimental data of the GRI-mechanisms. Finally, Skreiberg et al. [96] presented a new mechanism (SKGo3) for the combustion of biogas under fuel-rich conditions and moderate temperatures. It has been studied over a wide range of conditions, based on the measurements of Hasegawa and Sato [44]. Their experiments covered the fuels hydrogen (0 to 80 vol%), carbon monoxide (0 to 95 vol%), and methane (0 to 1.5 vol%), using equivalence ratios ranging from slightly lean to very fuel rich, temperatures from 300 to 1330 K, and NO levels from 0 to 2500 ppm.

In table 2.2 the laminar burning velocities of stoichiometric methane-air and hydrogen-air flames are presented. These velocities are determined with CHEM1D using the before mentioned methane based combustion reaction mechanisms. Also in this table the year the mechanism is mentioned together with the number of species and reactions. A noteworthy fact in this table is that both mechanisms, Dagaut and Nicolle [18] and Petrova and Williams [83], give ≈ 3 cm/s lower burning velocities for methane-air compared to the other ones. This is in the case of the mechanisms of Petrova and Williams probably caused by their effort to keep this mechanism rather small and hence included only a minimal set of reactions which are needed for the oxidation of hydrocarbons [83]. On the other hand the mechanism of Dagaut and Nicolle [18] is mainly validated with jet-stirred reactors and ignition data rather than laminar burning velocities. Note that, nowadays, experimental results reveal a value of 36 ± 1 cm/s as the laminar burning velocity of stoichiometric methane-air flames. Compared to the results in table 2.1 the results of methane based mechanisms in table 2.2 give a larger variation for stoichiometric hydrogen flames than the pure hydrogen mechanisms.

Besides the hydrogen based mechanisms mentioned in table 2.1, the methane based mechanisms used in the remainder of this thesis are the mechanisms: GRI-mech 3.0 [97], Konnov 0.5 [60], Leeds 1.5 [53], SKG03 [96] and GDF-kin[®] [27]. These mechanisms are used to compare their laminar burning velocity results with experimental data for the applied conditions mentioned in the previous chapter. Note that the selection is based on the laminar burning velocity only; making the selection somewhat arbitrary. A decent selection procedure should have included for example the comparison of ignition delay times, species profiles, sensitivity analysis. However, the focus of this thesis is mainly related to laminar burning velocities of hydrogen enriched methane-air mixtures the selection of the mechanisms based on the burning velocities is a useful start.

Note that the mechanism of Smooke [98] is also listed in table 2.2 and not further mentioned in the previous text. This mechanism is used in chapter 6 as a base mechanism for the methane-hydrogen asymptotic theory. This mechanism represents only a minimal subset of a complete reaction mechanism, and is also known as a skeletal mechanism. This mechanism does not include the reaction paths to higher hydrocarbons, but only represents the C1 chemistry. However, it predicts the important flame properties well for fuel-lean combustion [98].

Heat Flux Method

There are several experimental methods to determine the laminar burning velocity. This chapter focuses on one of them: the heat flux method. First an overview of several other methods for determining the laminar burning velocity is given. This is followed by a short description of the working principle of the heat flux method. Then the burner setup which is used in the present research is introduced. Next, the heat flux method is analysed in detail. This is followed by an example of how the setup is used to determine the laminar burning velocity, together with an error estimate. Finally a detailed analysis of the reproducibility of laminar burning velocity measurements using the heat flux method is presented.

3.1 Introduction

The adiabatic burning velocity of a fuel-oxidiser mixture is a key parameter in combustion research like stated in chapter 1. During the last decades various measurement techniques have been developed to measure the laminar burning velocity of gas mixtures. However, measuring the laminar burning velocity accurately is a rather difficult task, as the flame should be:

- adiabatic, which means that there is no heat loss to the surroundings,
- a flat flame with a plug-flow velocity profile, which means that the flame can be assumed to be a one-dimensional flame.

Phenomena like flame stretch and heat loss of the flame, influence the determination of the laminar burning velocity. This hampers accurate comparison between experimental data and theoretical or detailed numerical studies of laminar burning velocities. In this section five common experimental setups are briefly discussed: the counterflow burner; the Bunsen burner; expanding flames in a closed vessel; the flat flame burner and finally

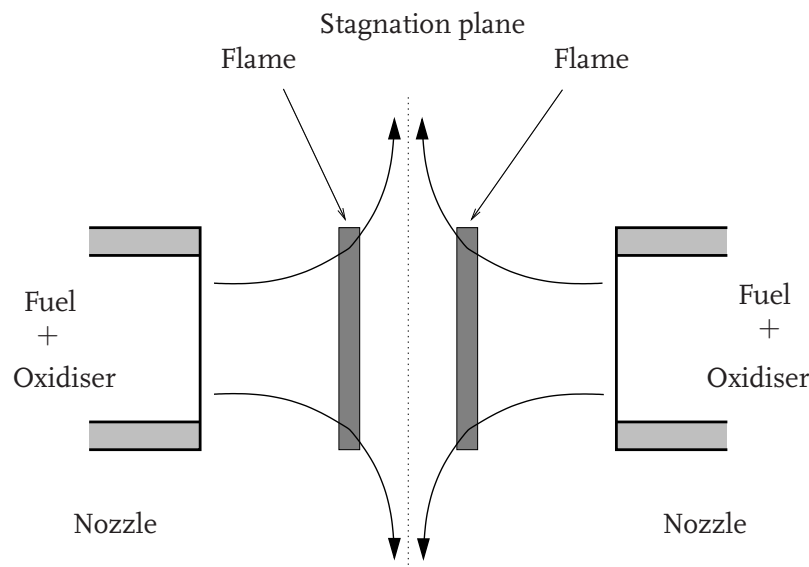


Figure 3.1: A schematic illustration of the experimental configuration of a premixed counterflow burner.

the heat flux burner. This latter one is used in this work and will be described into more detail.

Counterflow Method

The counterflow method or opposed jet method is based on the stabilisation of flames between counter-flowing jets. Both jets deliver a premixed fuel and oxidiser mixture. As a result, on both sides of the stagnation plane, premixed flames will be visible, like shown in figure 3.1. The flames stabilise in the flow and do not have any heat loss interaction with the burner. As can be seen in the figure indicated by the streamlines is that the flow profile of this configuration is not perpendicular to the flame front, which causes straining of the flow. Due to this straining the flames become stretched. The strain/stretch rate can be controlled by adjusting the distance between the nozzles. A larger distance between them will lead to a larger distance between the flame fronts. As a result the strain rate is smaller: so the flames become less disturbed. By repeating this experiment at various strain rates a correlation can be found between burning velocity and strain rate. To determine the laminar burning velocity the strain rate needs to be extrapolated to zero stretch. The resulting burning velocity depends highly on the model used for the extrapolation to zero stretch. A linear model as initially presented by Law [66] gives higher laminar burning velocity results for methane-air flames compared to a more recent non-linear stretch model presented by van Maaren et al. [74].

Bunsen Burner Method

Among the laminar burning velocity measurement methods the Bunsen burner is probably the oldest. In figure 3.2a a photograph of a premixed flame stabilised on a Bunsen burner is shown. A premixed mixture is flowing through a tube and a flame is stabilised at the exit rim of the tube. The total mass flow which is leaving the burner exit

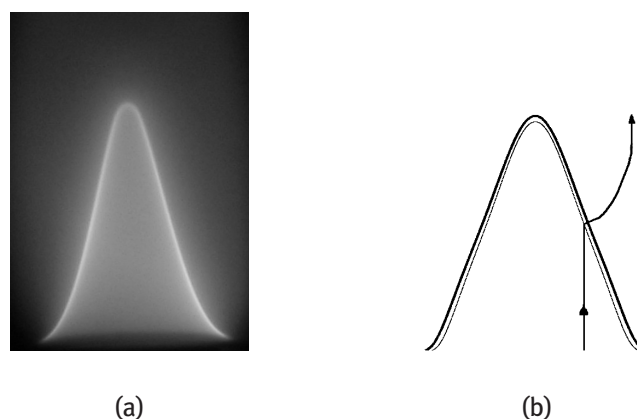


Figure 3.2: Photograph of a premixed methane-air Bunsen flame (left figure), and a schematic representation (right figure) of the flame surface profiles.

is equal to the amount of mass consumed by the flame. The flame seeks a stationary situation where this mass balance holds. Now the ratio of laminar burning velocity and the gas velocity equals the ratio between the flame surface and the burner diameter. Since the conical flame surface is larger than the burner exit area, the laminar burning velocity must be lower than the gas velocity. Although the Bunsen burner method is rather simple to apply, some difficulties in determining the laminar burning velocity occur mainly due to the uncertainty in the determination of the flame surface area. Depending on the optical method used the conical area may vary from the inner area to the outer area as shown in figure 3.2b, which can vary up to 10% [64]. Furthermore, immediately beneath the luminous area of this flame the unburnt gas changes flow direction from initially vertical direction to an outward direction as indicated by the arrow in figure 3.2. The gas flow passes the flame front almost perpendicular. However, in the flame tip stretch effects occur influence the laminar burning velocity. At the flame foot heat loss of the flame to the exit rim of the burner that influences the burning velocity.

Spherical Bomb Method

Unlike the previous two methods the spherical bomb method does not produce a stationary flame. A closed constant volume is filled with a combustible mixture a igniter is placed in the centre of the vessel. As the mixture is ignited, a spherical expanding flame is travelling from the centre to the outer walls. The laminar burning velocity can now be determined visually. Typical results of the visual method are shown in figure 3.3 where images of an expanding flame at three times are displayed. The flame velocity can be derived by determining the radius of the flame as a function of time [12, 39, 42]. After correction for gas expansion the laminar burning velocity is found. Also the pressure rise due to temperature increase can be used to determine the laminar burning velocity in a spherical bomb. Corrections are used for the pressure rise and temperature rise in the laminar burning velocity when the pressure as a function of time gives the basic information for the laminar burning velocity [76].

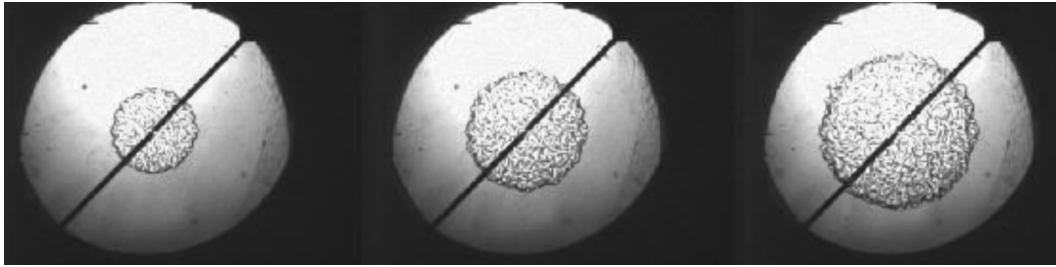


Figure 3.3: Schlieren images of an expanding hydrogen flame in a closed vessel [33]. Note that the flame is disturbed with cellular structures induced by hydrodynamic instabilities. These cellular structures enlarge the flame surface, resulting in an increased propagation velocity.

Flat Flame Burner Method

Powlings [86] was the first who tried to measure the laminar burning velocity with a flat flame burner. On this burner a 1D flame is stabilised on a porous metal disk at the exit of a water cooled flow tube. Botha and Spalding [10] improved the method by cooling the porous disk. This additional cooling brings the flame closer to the porous disk. They measured the temperature increase of the cooling water. In order to determine the laminar burning velocity several tests at different cooling rates need to be performed. The values of the gas velocities are plotted against cooling rates. The curve is then extrapolated to zero cooling rate to obtain the laminar adiabatic burning velocity. Experimentally the situation of zero cooling can not be achieved by this burner because the flame becomes instable and will blow off. According to Kuo [64] this method is quite accurate, however, in practise the temperature increase of the cooling water will be rather small and difficult to measure [64].

Heat Flux Burner Method

The heat flux method is a further improvement of the flat flame burner of Botha and Spalding [10] mentioned in the previous paragraph. It is introduced by de Goey et al. [35]. The basic idea behind the heat flux method is to compensate the heat loss by a heat gain of the unburnt gases when they flow through the burner plate [35]. This compensation of the heat loss needed for stabilising the flame on a flat perforated burner plate. The heat gain of the gas is only possible in the case that the unburnt gases are cooler than the burner plate. This heat gain is accomplished by fitting the perforated plate in a heated burner head. This gives a heat transport from the burner head to the burner plate and finally to the unburnt gas mixture. Generally the measured radial temperature profile in the plate is parabolic. The parabolic coefficient is zero when the gas inlet velocity U_g equals the laminar burning velocity S_L and the stabilised flame becomes adiabatic. The advantage of the heat flux method is that there is no need to extrapolate to determine the laminar burning velocity of an adiabatic flat flame. The heat flux method as used in the present research, has been developed to measure laminar burning velocities accurately in recent years, see e.g. [8, 72]. The experimental setup and the method is discussed in detail in the next sections.

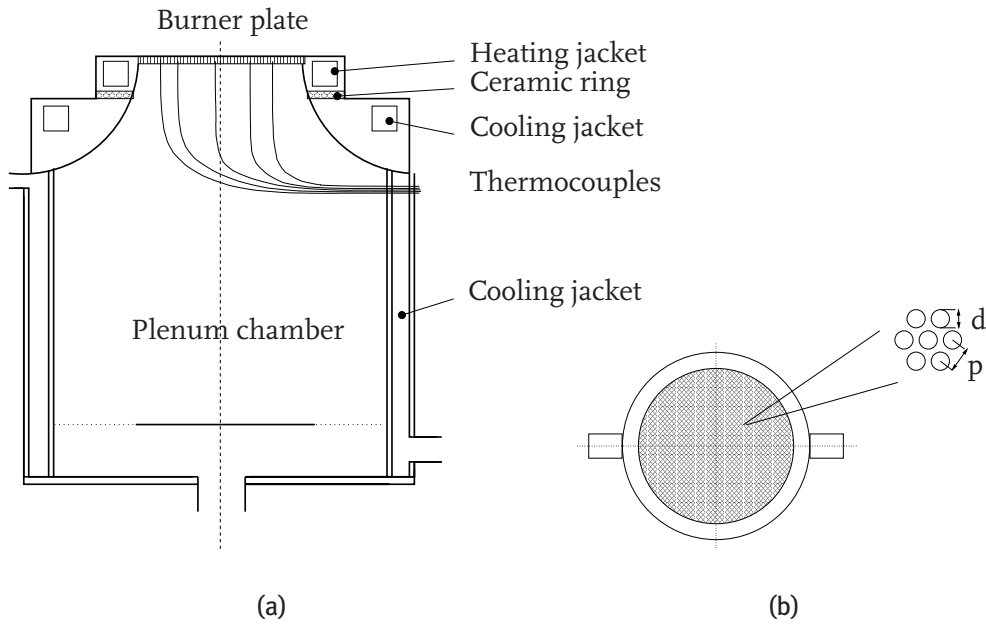


Figure 3.4: Schematic representation of the heat flux burner (left figure), indicating the main components of the burner. The right figure is a top view of the burner showing the perforation pattern of the burner plate.

3.2 The Heat Flux Burner

The goal of this section is to explain the principle of the heat flux method. First an overview of the present design of the heat flux burner is presented. The experimental set-up used here is similar to the one used in previous studies [8, 9] and has been extensively tested and optimised in recent years [8, 72]. A schematic representation of this burner is shown in figure 3.4. The plenum mixing chamber has a cooling system supplied with water at 298 K. The burner head consists of a heating jacket supplied with water kept at $T_R \approx 360$ K. This jacket keeps the burner plate edges at a certain temperature higher than the initial gas temperature, which causes the unburnt gas mixture to heat up when flowing through the burner plate. By doing so, the heat loss necessary to stabilise the flame can be compensated by the heat gain of the unburnt mixture. This leads to a stabilised adiabatic flame. The flat flame is stabilised on a perforated and heated brass plate. The applied burner plate is perforated with a hexagonal pattern of small holes, see figure 3.4b. The burner plate used in the current research is perforated with holes with a diameter d of 0.5 mm and pitch p of 0.7 mm. The perforation pattern is shown in figure 3.4b. The thickness h of the burner plate is 2 mm and it has a radius R of 15 mm. Eight thermocouples are glued into holes of the perforated plate. The thermocouples are positioned at different radii and different angles to measure the temperature profile across the burner plate. These copper-constantan thermocouples of 0.1 mm in diameter are positioned at the following pairs of radius-angle combinations 0 (0°), 2.8 (330°), 4.9 (150°), 7.7 (270°), 9.1 (30°), 10.5 (90°), 12.6 (210°), 14.7 (330°). The influence of the radiation on the thermocouple readings was neglected because the measured temperature of the burner plate was always below 400 K (unless otherwise mentioned).

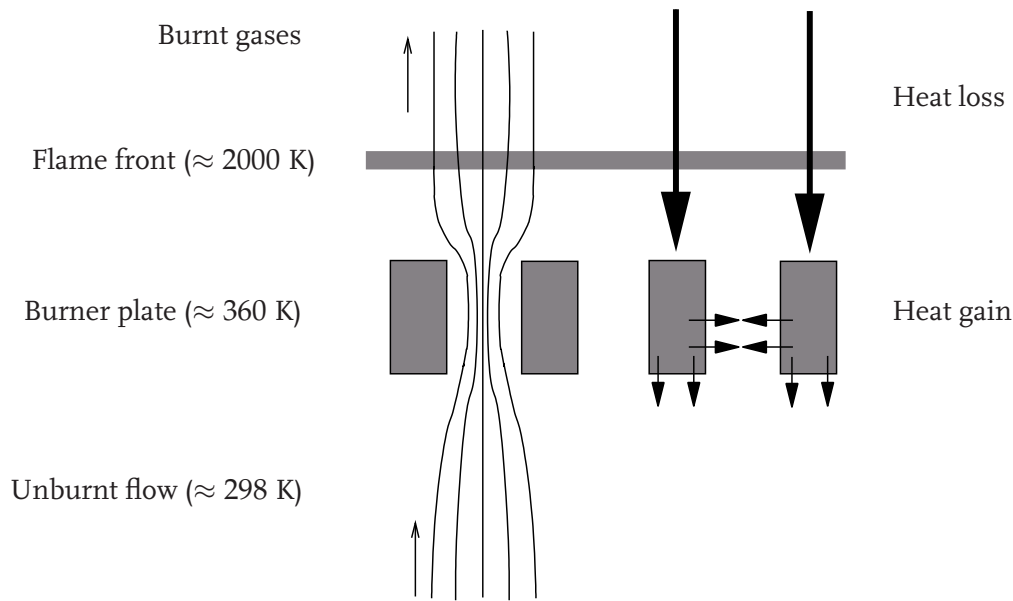


Figure 3.5: A close up of a small part of the burner plate showing a schematic representation of the heat flux method in the case of a stabilised flame. (left) a sketch of the flow pattern through a hole, the heat fluxes between burner, gas and flame (right). Typical temperatures appearing when a flame is stabilised on this burner are indicated.

3.2.1 Working Principle

Although in the previous part of this section the heat flux set up is introduced, the heat flux method still needs to be clarified in a more detailed way. In figure 3.5 a schematic overview of the method is depicted. The unburnt gas is flowing through a perforated flat burner plate. This burner plate is kept at temperatures typically 60 K above the unburnt gas temperature. The burner plate has a heat loss to the gas mixture causing the gas mixture to increase in temperature. A flame is stabilised on top of this burner plate with a typical temperature of ≈ 2000 K. On the right hand side of figure 3.5 the heat flows are depicted between the burner plate, the unburnt gas and the flame. The smaller arrows indicate the heat gain of the unburnt gas mixture by the burner plate, while the larger arrows indicate the heat loss from the flame to the burner plate. When the gas inlet velocity is lower than the laminar burning velocity, the flame is stabilised on the burner. As a result the heat loss of the flame to the burner plate is larger than the heat gain of gas mixture by the burner plate. When the unburnt gas velocity is above the laminar burning velocity the heat gain of the gas by the burner plate is larger than the heat loss of the flame. An adiabatic situation is found when there is *no* net heat loss to the burner. In this case the laminar adiabatic burning velocity equals the inlet velocity of the gas mixture. In practise however, it is difficult to adjust the gas flow to represent the exact velocity where $U_g = S_L$. This practical inconvenience is circumvented by interpolation of the gas velocity towards a zero heat flux. The heat flux is determined by measuring the temperature profile across the burner plate with the thermocouples attached to the burner plate. This temperature profile represents the effect of the heat flux, i.e. it indicates whether the burner plate is losing heat or gaining heat. A detailed description of the interpolation

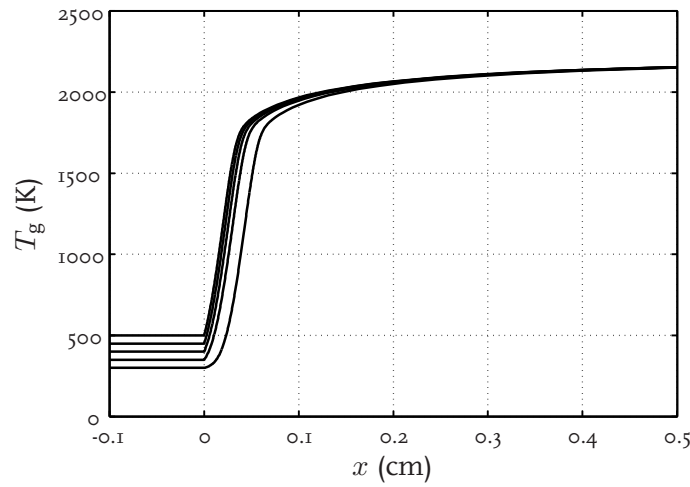


Figure 3.6: Temperature profile of a 1D burner stabilised flames with increasing heating jacket temperature T_R and constant mass flow as a function of the height above the burner, x .

of the gas velocity towards a zero flux is given in section 3.3 where a typical example of a measurement is shown. In this section the method to stabilise adiabatic flames on a burner is explained by using figure 3.5. A more fundamental description is given in Appendix D, showing that the flame properties of an adiabatic burner stabilised flame can be seen as properties of freely propagating flames. The only difference compared to a free flame is that the stand-off distance of the flame alters with varying temperatures of the heating jacket, T_R . This behaviour is shown in figure 3.6 where numerical results of several 1D burner stabilised flames have been calculated with increasing T_R and constant mass flow $\dot{m} = 0.040 \text{ gr cm}^{-2} \text{ s}^{-1}$. The flame temperature is unchanged, although the flame is moving slightly closer to the burner plate indicating a shorter stand-off distance. De Goey et al. [37] performed 2D simulations of a flame stabilised on a heat flux burner. they concluded that the species mass fractions profiles are not disturbed by the burner plate. Only small local differences are likely to occur in practise in the area close to the downstream side of the burner plate, due to small flow disturbances induced by the presence of the burner perforations. However, the flow pattern and flame structure should represent a 1D situation before reaching the reaction layer [36, 72]. If this is not succeeded then the consumption speed of the flame is not equal to the laminar burning velocity anymore but is slightly different due to flame stretch and curvature effects. By using 2D simulations to determine this small scale structure of flat burner stabilised flames de Goey et al. [37] showed that these disturbances are flattened out by the pressure drop over the flame. In the present setup these disturbances are negligibly small: van Maaren et al. [73] estimated that with well chosen diameter and pitch dimensions the stretch rate $\approx 1 \text{ s}^{-1}$. The maximum hole diameter that can be used before the flat flame becomes perturbed by the perforation geometry is determined by the applied flow velocity. A larger flow rate requires smaller holes for the flow to become uniform. The current burner plate configuration with, $d = 0.5 \text{ mm}$ and $p = 0.7 \text{ mm}$, can be used for burning velocities up to 60 cm/s [37].

3.2.2 Energy Equation of the Burner Plate

In the remaining part of this section the heat flux balance of the burner plate is analysed in order to interpret the applied temperature measurements. The analysis is started by considering the energy equation of the plate in cylindrical coordinates, with conductivities ($\lambda_{p,r}, \lambda_{p,x}$), depending on the diameter and pitch of the perforation in the plate,

$$-\frac{1}{r} \frac{\partial}{\partial r} \left[\lambda_{p,r}(r) r \frac{\partial T_p(x, r)}{\partial r} \right] - \frac{\partial}{\partial x} \left[\lambda_{p,x}(r) \frac{\partial T_p(x, r)}{\partial x} \right] = -\alpha [T_p(x, r) - T_g(x, r)], \quad (3.1)$$

with α the heat transfer coefficient between the burner plate and the gas mixture. The plate temperature $T_p(x, r)$ in equation (3.1) depends on the axial position and radial position r . The conduction terms $\lambda_{p,x}$ and $\lambda_{p,r}$ have been investigated numerically in detail by Sonnemans [101] and confirmed experimentally by van Maaren [72]. Due to rotational symmetry of the system the tangential term in the θ direction is omitted. Also the radiation of the burner plate is not included due to the relative low burner plate temperature; typically 360 K in the current burner setup. Integration of equation (3.1) over the burner thickness from $x = 0$ to $x = h$, gives

$$\begin{aligned} -\frac{1}{r} \frac{\partial}{\partial r} \left[\lambda_{p,r}(r) r \frac{\partial}{\partial r} \int_0^h T_p(x, r) dx \right] &= - \int_0^h \alpha [T_p(x, r) - T_g(x, r)] dx \\ &\quad + \lambda_{p,x}(r) \frac{\partial T_p(x, r)}{\partial x} \Big|_{x=h} - \lambda_{p,x}(r) \frac{\partial T_p(x, r)}{\partial x} \Big|_{x=0} \\ &= q(r). \end{aligned} \quad (3.2)$$

In this equation q is the net heat flux from the gas to the plate, including the heat loss of the flame and the heat gain of the unburnt gas. Introducing an average plate temperature $\bar{T}_p(r)$,

$$\bar{T}_p(r) = \frac{1}{h} \int_0^h T_p(x, r) dx, \quad (3.3)$$

gives together with equation (3.2):

$$-\frac{1}{r} \frac{d}{dr} \left[\lambda_{p,r}(r) r \frac{d}{dr} \bar{T}_p(r) \right] = \frac{q(r)}{h}. \quad (3.4)$$

In general the conduction coefficient $\lambda_{p,r}$ depends on the temperature and the perforation pattern. However, Bosschaart [7] showed that when determining the laminar burning velocity the temperature influence on $\lambda_{p,r}$ is rather minimal, resulting in a conduction coefficient λ_p which is only dependent on the conduction coefficient of brass λ_{br} and geometrical effects which can be parametrised by the parameter ϵ , in the following way:

$$\lambda_p = \epsilon \cdot \lambda_{br}. \quad (3.5)$$

The geometrical constant ϵ for the current diameter pitch dimensions of 0.5 mm and 0.7 mm is determined by Sonnemans [101] and van Maaren [72]. A value of $\epsilon = 0.362$ is used. Now, equation (3.4) can be solved together with the boundary condition $\bar{T}_p(r = 0) = T_c$ this gives:

$$\bar{T}_p(r) = T_c - \frac{q}{4\lambda_p h} r^2. \quad (3.6)$$

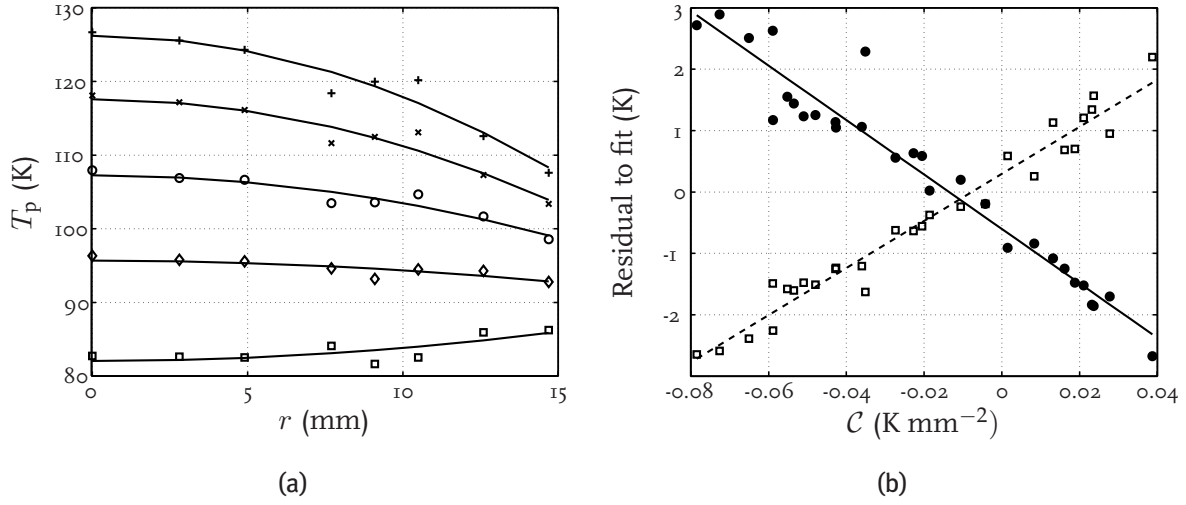


Figure 3.7: Thermocouple temperature profiles for a stoichiometric methane-air flame with different gas velocities (left figure). Gas velocities varying from 33 (upper curve) to 37 cm/s (lower curve) in steps of 1 cm/s. The differences from the measurements to the parabolic fit in the left figure plotted against the parabolic coefficient C (right figure). Note that only the thermocouples at $r = 7.7$ mm (\square) and $r = 10.5$ mm (\bullet) are selected, the other thermocouples have typical differences of ≈ 1 K.

This indicates that the temperature distribution in the burner plate appears to be a parabola, with the centre of the burner plate as the symmetry axis. Therefore it is possible to determine the laminar burning velocity for a given gas mixture composition by measuring the temperature profiles across the burner plate for several gas velocities. In the next section this technique is applied and a typical measurement is shown.

3.3 Typical Laminar Burning Velocity Measurement

In the previous section several assumptions applied to the heat flux method have been investigated in detail. In this section the theory of the heat flux method is applied to a typical measurement situation, e.g. a stoichiometric methane-air flame. For a given gas mixture composition, several temperature profiles are measured with varying gas inlet velocity. The velocity U_g is varied around the laminar burning velocity. The temperature distribution in the plate is measured with the thermocouples attached in the burner plate. Typical experimental temperature profiles (symbols) are shown in figure 3.7a. In this figure the gas velocity U_g is increased from 33 (upper curve) up to 37 cm/s (lower curve). The flame is changing with increasing velocity from a burner stabilised flame into a *super* adiabatic flame. Since equation (3.6) is a parabolic function, the experimental temperature profiles are fitted with a parabolic function and become

$$T_p(r) = T_c + Cr^2, \quad \text{with} \quad C = -\frac{q}{4\lambda_p h}, \quad (3.7)$$

with \mathcal{C} the parabolic coefficient. In figure 3.7a the measured plate temperatures are plotted as a function of the radius (symbols), together with the parabolic fit as a function of the radius (solid line). The parabolic coefficient \mathcal{C} determines whether a flame is sub adiabatic or *super* adiabatic. A negative value of \mathcal{C} indicates that there is a net heat loss from the flame to the burner, and a positive value indicates a net heat gain of the gas mixture by the plate. Small fluctuations in the measured temperature profiles in figure 3.7a are still visible when comparing them to the parabolic fit, e.g. the thermocouple at a radius of ≈ 7.7 mm. Bosschaart [7] noticed that these fluctuations arise due to a systematic error and a random error. The systematic error is traced down to the small differences in attachment of the positions of the thermocouples in the holes in the plate in axial direction (See Appendix D). For each thermocouple, k , the resulting equation now becomes [7]:

$$T_{p,k}(x_k, r) = (T_c + \mathcal{C}r^2) \left(1 + c\epsilon\alpha^2 h x_k\right), \quad \text{with} \quad \mathcal{C} = -\frac{T_c}{4}\alpha^2, \quad (3.8)$$

with c a constant, ϵ parameter to describe the geometrical effects shown in equation (3.5), h the thickness of the plate and x_k the height dependence of thermocouple k . x_k can vary between 0 and 2 mm. Compared to the 1D situation in equation (3.6) this equation is extended with a height dependent factor. This height dependent factor corresponds to the effective attachment height of a thermocouple in the burner plate. This attachment height is slightly different for every individual thermocouple and results in a correction which is proportional to the parabolic coefficient. In figure 3.7b the deviation from experimental data to the polynomial fit is plotted for two thermocouples ($r = 7.7$ mm and $r = 10.5$ mm) as a function of the parabolic coefficient \mathcal{C} . Note that these thermocouples have been selected because they have the largest deviations from the parabolic fit. The remaining 6 thermocouples have typical deviations of ± 1 K. The symbols in figure 3.7b denote thermocouple measurements of a large set of experimental data with varying equivalence ratios (variation of gas heat conductivity) and flame stabilisation (variation of the heat loss). A linear fit is used through the experimental points in order to be able to determine the correction which has to be used with a certain polynomial coefficient \mathcal{C} . Now a temperature correction can be applied to the data presented in figure 3.7a by first calculating the parabolic coefficient \mathcal{C} . The linear fit of the thermocouple correction in figure 3.7b gives for a certain height-dependent thermocouple a certain temperature correction. For example the thermocouple at $r = 7.7$ cm gives a temperature correction of -2 K in the case a parabola coefficient of $\mathcal{C} = -0.06$ K mm $^{-2}$ is measured. Now the measured temperatures are adapted to find the corrected temperature. The other thermocouples are corrected in a similar way. The result is shown in figure 3.8a. Compared to figure 3.7a the systematic variation of the thermocouples is largely vanished. The remaining fluctuations can be contributed to the measurement system, thermocouples themselves and analog digital conversion. In figure 3.8b the parabolic coefficients \mathcal{C} (crosses) are finally plotted against the unburnt gas velocity U_g . In order to determine the laminar burning velocity a third order polynomial fit is applied to the parabolic coefficients of the temperature corrected experimental data. Now by a linear interpolation of this fit to $\mathcal{C} = 0$, the laminar burning velocity is found. In this case pure methane flame, and $\phi = 1$, the laminar burning velocity of 36.43 cm/s. In figure 3.8b this value is denoted with a circle.

Summarising, the laminar burning velocity is determined by measuring the temperature

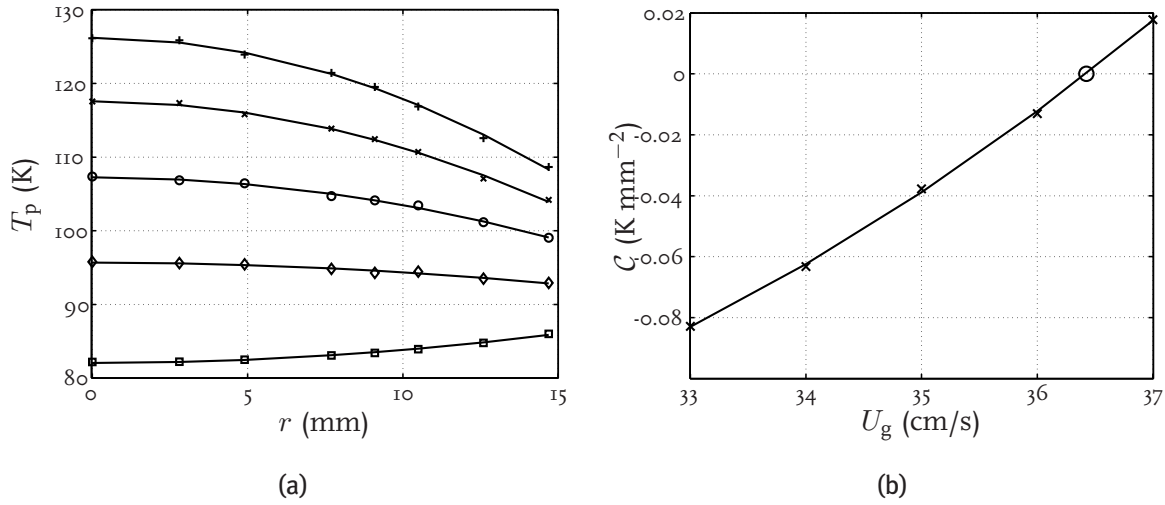


Figure 3.8: Corrected thermocouple temperature profiles for a stoichiometric methane-air flames with different gas velocities (left figure). The gas velocities vary from 33 (upper curve) to 37 cm/s (lower curve) in steps of 1 cm/s. The temperatures are corrected for the systematic errors occurring due to the difference in thermocouple attachment position. Parabolic coefficients determined from the corrected temperature curves plotted against the gas velocity (right figure). At $C = 0$ the laminar adiabatic burning velocity is at 36.43 cm/s.

profile of a certain gas mixture for several gas velocities. This is followed by a correction of the temperature profile in order to reduce the systematic error due to variation in the attachment height of the thermocouples. A parabolic curve is fitted through these corrected temperature measurements. The resulting parabolic coefficients for several gas velocities for this specific mixture are used to determine a flat temperature profile ($C = 0$). The velocity corresponding to this flat temperature profile is the laminar burning velocity which is found by interpolation. In the remaining part of this section the resulting accuracy of the measurements is extended.

3.3.1 Error Estimate

Bosschaart and de Goey [8] analysed the heat flux method in detail. The flow velocity and the gas mixture are regulated by carefully calibrated mass flow controllers (MFC). The calibration is done in order to correct for any nonlinear effect in the devices and electronic circuits¹. In Appendix B the calibration procedure is described. After calibration the uncertainty of an MFC can be estimated according to Bronkhorst Hi-Tec [50] with:

$$\Delta \dot{m} = 0.5\% \text{ Reading} + 0.1\% \text{ Full Scale.} \quad (3.9)$$

The uncertainty $\frac{\Delta \dot{m}_i}{\dot{m}_i}$ will be $\approx 0.7\%$ per MFC, in case the MFC is used in a range above 10% of its maximum flow rate. This uncertainty of the massflows is shown in figure 3.9 as a function of the equivalence ratio. Now, the resulting errors in the equivalence ratio can

1. More information concerning the present calibration setup can be found in the thesis of Bosschaart [7].

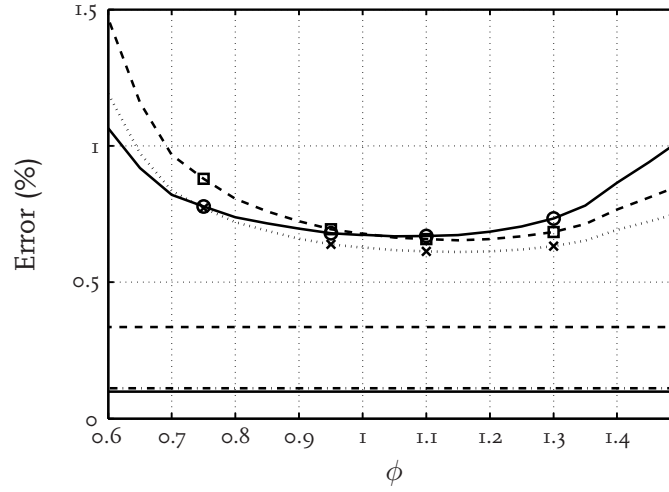


Figure 3.9: Error estimates of the individual component of the gas velocity and equivalence ratio, temperature, pressure and burner deck area of a methane-hydrogen-air mixture with 30 mol% of hydrogen in the fuel mixture. The solid line denotes the error estimate of the pressure; dashed line, temperature; dashed dotted line, area; solid line with circles, air mass flow; dotted line with squares, methane mass flow; dashed line with squares, hydrogen mass flow.

be estimated by using partial derivatives of the equivalence ratio as a function of the mass flows as mentioned in equation (B.1). This results in a relative error in the equivalence ratio $\Delta\phi$ which is given by the sum of relative errors of the separate mass flows,

$$\frac{\Delta\phi}{\phi} = \sum_{i=1}^{N_{\text{MFC}}} \left| \frac{\Delta\dot{m}_i}{\dot{m}_i} \right|. \quad (3.10)$$

This gives typical uncertainties of $\approx 2\%$ for equivalence ratios around 1.0. For other equivalence ratios the errors become larger, because the relative error of the MFCs increases when producing smaller flows. The resulting error in the gas velocity is also a straightforward analysis using partial derivatives of the gas velocity as a function of the conditions and the mass flows in equation (B.2), leading to:

$$\frac{\Delta U_g}{U_g} = \left| \frac{\Delta T_u}{T_u} \right| + \left| \frac{\Delta p_u}{p_u} \right| + \left| \frac{\Delta A}{A} \right| + \sum_{i=1}^{N_{\text{MFC}}} \left| \frac{\Delta\dot{m}_i}{\dot{m}_i} \right|. \quad (3.11)$$

The individual components of the equations (3.10) and (3.11) can be determined when using typical error estimates for the unburnt temperature, pressure and the burner deck area given by $\Delta T_u = 1$ K, $\Delta p_u = 100$ Pa, and $\Delta A = 0.785 \text{ mm}^2$ (corresponding 1 mm variation in diameter), respectively. In figure 3.9 the individual components of the error estimates are plotted as a function of the equivalence ratio for methane-hydrogen-air flame with 30 mol% of hydrogen in the fuel mixture. The relative error of the mass flows on the lean and rich side can be reduced by choosing MFCs which have been designed for smaller gas flows. Note that the unburnt gas temperature, pressure and burner deck area have a relatively small influence on the total error estimate of the gas velocity compared the mass flows of the gases.

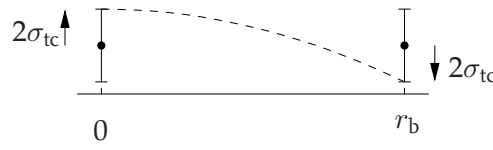


Figure 3.10: Error estimate of the parabolic coefficient, \mathcal{C} , due to remaining scatter in thermocouple measurements. The dashed line shows the parabola which is still acceptable within errors of the outer thermocouples.

The influence of the remaining fluctuation in the thermocouple readings on the burning velocity will be addressed in the remaining part of this section. Although in the previous section the systematic error of the thermocouple readings has been eliminated, a statistical error in the burning velocity measurement remains due to thermocouple scatter. To estimate this error the sensitivity s is defined as

$$s = \left. \frac{d\mathcal{C}}{dU_g} \right|_{\mathcal{C}=0}, \quad (3.12)$$

indicating the variation of the parabolic coefficient when the gas velocity is changed. This sensitivity coefficient s can be determined from figure 3.8b. The error estimate of the temperature readings due to the remaining scatter in the thermocouple measurements is σ_{tc} . By taking standard deviations from the residues of the parabola fits from the corrected thermocouple readings of figure 3.8a, the error estimate of the temperature readings is known. This leads to an uncertainty in the parabolic coefficient of:

$$\sigma_{\mathcal{C}} = \frac{4\sigma_{tc}}{r_b^2}, \quad (3.13)$$

with r_b the outermost thermocouple. In figure 3.10 this error estimate procedure of the parabolic coefficient is illustrated. The dashed line shows a parabola across the radius of the burner plate which is still acceptable as a fit, in the situation that two thermocouples, at $r = 0$ and $r = r_b$, measure equal temperatures. According to Bosschaart and de Goey [8] the error in the burning velocity due to the remaining scatter in the thermocouple measurements can now be estimated by combining equations (3.12) and (3.13):

$$\sigma_{S_L} = \frac{1}{s} \cdot \frac{4\sigma_{tc}}{r_b^2}, \quad (3.14)$$

where $r_b = 14.7$ mm is the position of the thermocouple on the edge of the burner. The resulting average error estimate in the laminar burning velocity with the heat flux method is in general less than 0.4 cm/s in the case of varying equivalence ratios, based on a 95% confidence interval. The average error in the equivalence ratio is less than 0.035 for the entire measurement range. Only at very low or high equivalence ratios the error can become larger.

3.3.2 Heating Jacket

In appendix C the background of the heat flux method is described more elaborately. It is assumed that the actual value of the temperature of the heating jacket T_R is not

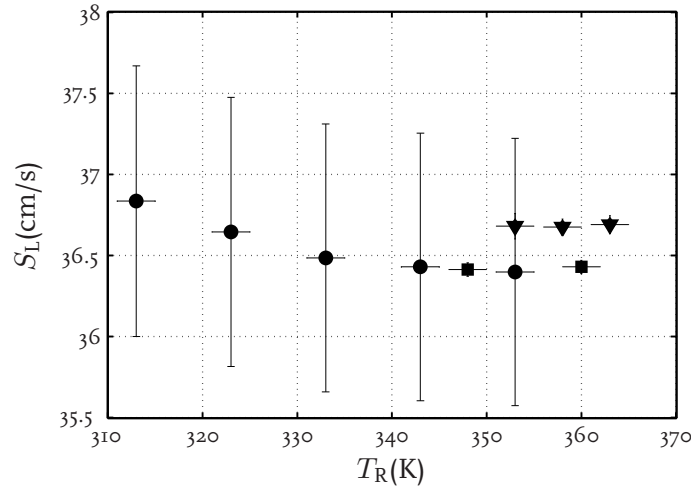


Figure 3.11: Measured laminar burning velocities of stoichiometric methane-air mixtures as a function of the heating jacket temperature. Denoted symbols are $T_u = 298$ K, regular measurements, \bullet ; $T_u = 298$ K with long stabilisation, \square ; $T_u = 299$ K, \blacktriangledown .

important, as long as T_R is high enough to prevent partial blow-off. Figure 3.11 shows the measured laminar burning velocity of a stoichiometric methane-air mixture is shown (with error estimate) as a function of the heating jacket temperature T_R . The circles are regular measurements, whereas the squares denote measurements which were focused on optimal accuracy. This is achieved by taking long temperature stabilisation times of approximately half an hour after changing the mass flow, together with a set of mass flow controllers that produces more stable mass flows. These measures are used in order to reduce the fluctuations in the temperature profile. The laminar burning velocity results at $T_u = 298$ K are all within their error estimates. However, the error estimates are increasing at lower values of T_R resulting in a less accurate measurement of the laminar burning velocity. This tendency indicates that more gas is consumed by the flame, although the input parameters are kept constant (e.g. equivalence ratio, temperature, pressure). The flame surface is increasing by tending to blow-off, because the temperature difference between T_u and T_R (which is needed for stabilisation) gets smaller; A minimum temperature difference of ≈ 30 K between T_u and T_R should be maintained to measure the laminar burning velocity accurately. Figure 3.11 gives also a clear overview of the reproducibility of laminar burning velocity measurements with the heat flux method: the *regular* measurements (circles) are within the error bars of each other. Note that measurements denoted with triangles are measurements performed with optimal accuracy and an unburnt gas temperature T_u increase of ≈ 1 K. Even the measurements with this optimal accuracy are within the error bars of each other, both squares and triangles. This relative small change in unburnt gas temperature can even be observed with the current heat flux method.

Experimental Results

Laminar burning velocity measurements performed with the heat flux method are presented and compared with experiments by other researchers in this chapter. The first part of this chapter deals with measurements of the laminar burning velocity of hydrogen-oxygen-nitrogen flames at ambient conditions. The oxygen fraction is lowered compared to the contents as occurring in air. In the remaining part of this chapter measurements of the laminar burning velocities of methane-hydrogen-air flames are presented not only at ambient conditions but also at increased unburnt gas temperatures. The resulting adiabatic burning velocities measured with the heat flux method are presented with error margins using a 95% confidence interval. Typical error margins for methane-hydrogen-air flames are 0.3 cm/s.

4.1 Introduction

Laminar burning velocities of methane-air mixtures as a function of temperature, pressure and stoichiometric ratio have been measured by many investigators using several experimental techniques. In the previous chapter some of these techniques have been addressed. The experimentally determined laminar burning velocity results were inconsistent for a long time. The laminar burning velocity for a stoichiometric mixture at ambient conditions varied typically between 35 and 45 cm/s, see e.g. figure 4.1. A major breakthrough came when van Maaren and de Goey [74] demonstrated numerically that flame stretch due to flame front curvature and/or flow divergence must be taken into account. For this reason, the methodology of the determination of laminar burning velocity with the counterflow twin-flame technique by extrapolation to zero stretch rate has been further improved by Vagelopoulos et al. [106]. The same yields for constant volume bombs where the experimentalist has to use essentially the same approach to determine the unstretched burning velocities. Nowadays experimental data of laminar

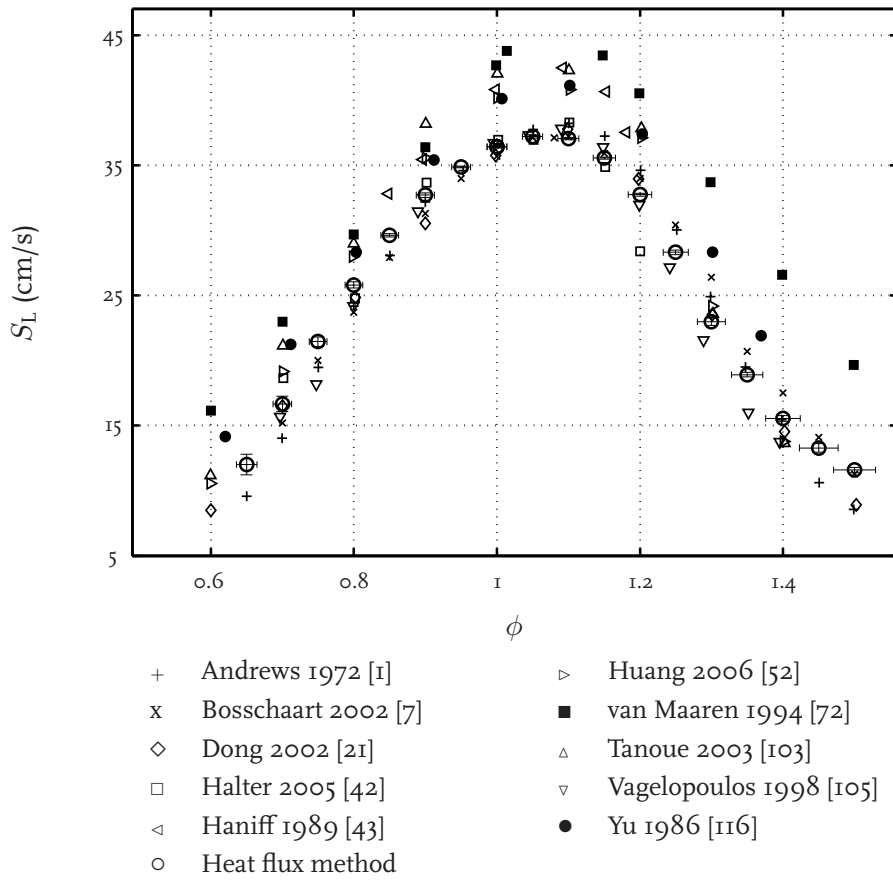


Figure 4.1: Experimental results from literature of the adiabatic burning velocity of methane-air flames at ambient conditions.

burning velocities, with the applied new insights, lead to more consensus, which is for stoichiometric methane-air flames ≈ 36 cm/s within ± 1 cm/s.

The laminar burning velocities of hydrogen-air mixtures were not consistent because of the same reasons. A large spread of the laminar burning velocity is found in literature, see figure 4.2, where for example the maximum laminar burning velocity at ambient conditions ranges from 260 to 350 cm/s. For hydrogen flames part of the scatter in the measurements of figure 4.2 is also related to cellular instabilities over the flame surface. An example of such an instability can be seen in the previous chapter in figure 3.3, where the expanding flame is disturbed with cellular structures induced by hydrodynamic instabilities. The cellular structures enlarge the flame surface, resulting in an increased propagation velocity. Hence, the laminar burning velocity is difficult to determine from the experimental data.

Experimental results available in literature are concentrated around pure methane-air flames or pure hydrogen-air flames, rather than fuel mixtures consisting of methane and a significant amount of hydrogen. In the case of methane-hydrogen-air flames some data is available in literature, e.g. Coppens et al. [17], Halter et al. [42], Haniff et al. [43], Huang et al. [52], and Yu, Law and Wu [116]. However, the experimental data are either not corrected for non-linear stretch effects or the supplied data is only available at selected

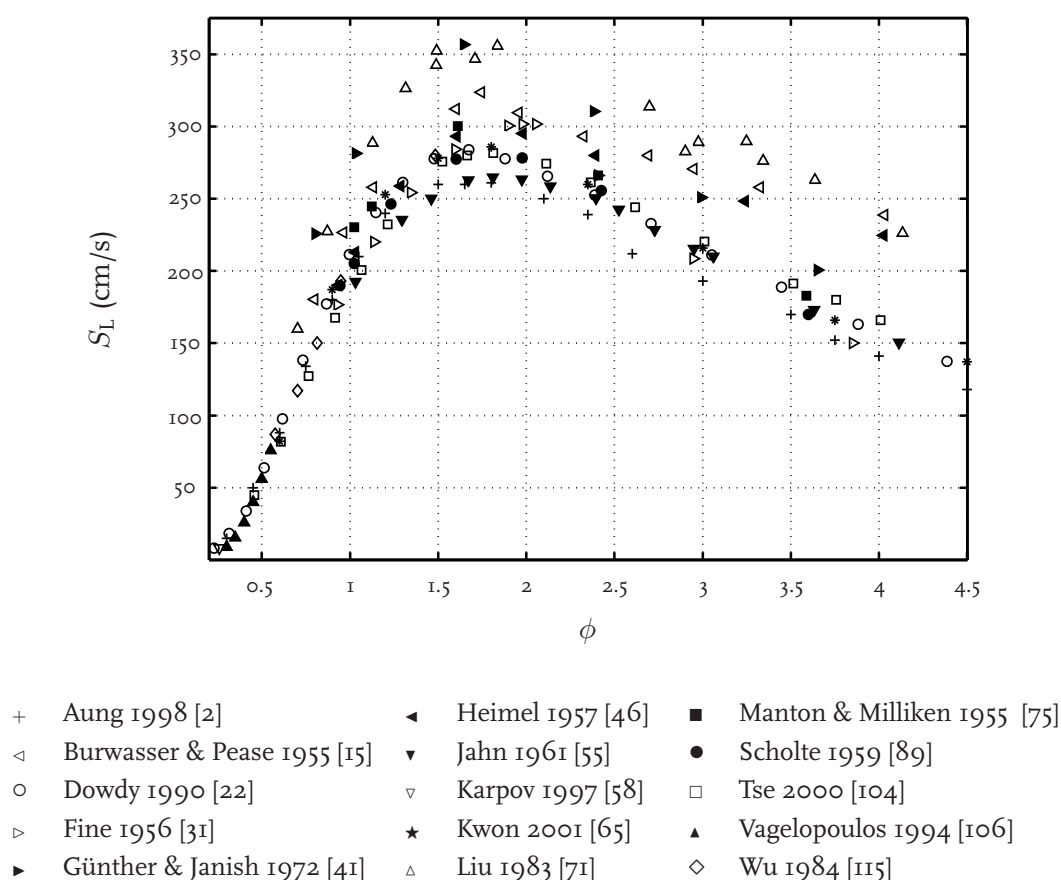


Figure 4.2: Experimental results from literature of the adiabatic burning velocity of hydrogen-air flames at ambient conditions.

hydrogen fractions and equivalence ratios rather than a broad range.

In this chapter laminar burning velocities measurements, as determined with the heat flux burner, are presented and compared with experimental data of other researchers. The results of the measurements are reported in section 4.2 starting with a set of measurements of hydrogen flames with lower oxygen contents by dilution with extra nitrogen. Note that for completeness the experimental data with error estimates are also tabulated in appendix E. The results of hydrogen flames diluted with nitrogen are followed by experimental results of methane-hydrogen-air flames at ambient conditions in section 4.3. Then a last set of measurements of methane-hydrogen-air flames was carried out at increased unburnt gas temperature. This provides us with information on laminar burning velocities progressing towards gas turbine conditions. These measurements are presented in section 4.4. In the last section of this chapter the experimentally determined laminar burning velocities are evaluated and a number of conclusions is drawn.

4.2 Hydrogen-Oxygen-Nitrogen Flames

Burning velocities of hydrogen-air mixtures as a function of equivalence ratio, temperature and pressure have been measured by many investigators. The heat flux setup, as

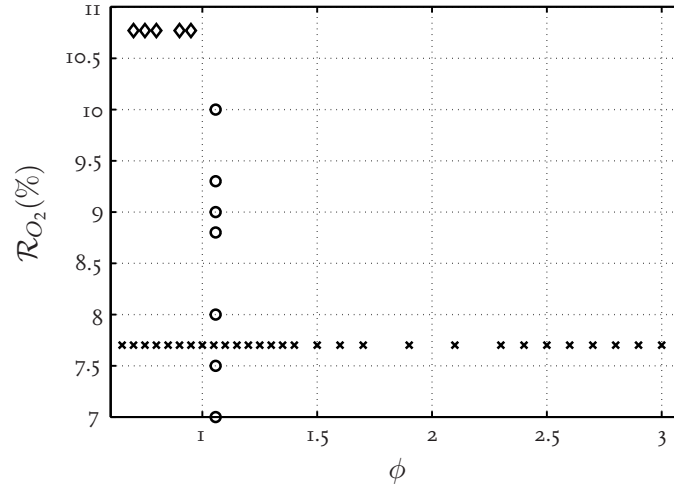


Figure 4.3: Investigated parameter range of hydrogen-oxygen-nitrogen flames. The symbols denote: constant equivalence ratio $\phi = 1.06$ and varying \mathcal{R}_{O_2} : \circ ; $\mathcal{R}_{O_2} = 7.7\%$ and varying ϕ : \times ; $\mathcal{R}_{O_2} = 10.7\%$ and varying ϕ : \diamond .

presently available, is designed to determine laminar burning velocities accurately for gas mixture velocities below ≈ 60 cm/s. For hydrogen-air mixtures this range occurs at very lean mixtures ($\phi < 0.5$), see figure 4.2. As a result only a rather small range in equivalence ratio can be measured. Extending this range can be achieved by dilution of the mixture with nitrogen. In standard air the ratio between oxygen and nitrogen content, defined as

$$\mathcal{R}_{O_2} = \frac{X_{O_2}}{X_{O_2} + X_{N_2}} \cdot 100\% \quad (4.1)$$

is $\approx 21\%$. Laminar burning velocity results from numerical simulations indicate that this ratio should be below $\approx 10\%$ in order to have a laminar burning velocity over a broad range of equivalence ratios below 60 cm/s. However, the available amount of reliable data for the burning velocities of hydrogen-oxygen-nitrogen mixtures with oxidiser composition different from that of air is limited. These kind of nitrogen diluted hydrogen flames were studied using the counterflow twin-flame technique by Egolfopoulos and Law [26].

In this section three sets of experimental data have been measured. The measured data range is depicted in figure 4.3, in which the symbols denote measured data points as currently accessed with the heat flux burner. The first set of experiments are carried out with constant equivalence ratio, $\phi = 1.06$, and varying oxygen content, \mathcal{R}_{O_2} . The second and third set of measurements are conducted with constant oxygen content, and varying equivalence ratio. The oxygen contents are 7.7 and 10.7% respectively. The measurements are performed with an unburnt gas temperature of 298 K at ambient pressure. The measured data for the laminar burning velocity are shown in figures 4.4, 4.5 and 4.6. The results are presented with 95% confidence interval error estimates. These error estimates for the oxygen fraction and for the burning velocity were derived as described in chapter 3. In the next section the data are analysed and compared with experimental data of Egolfopoulos and Law [26].

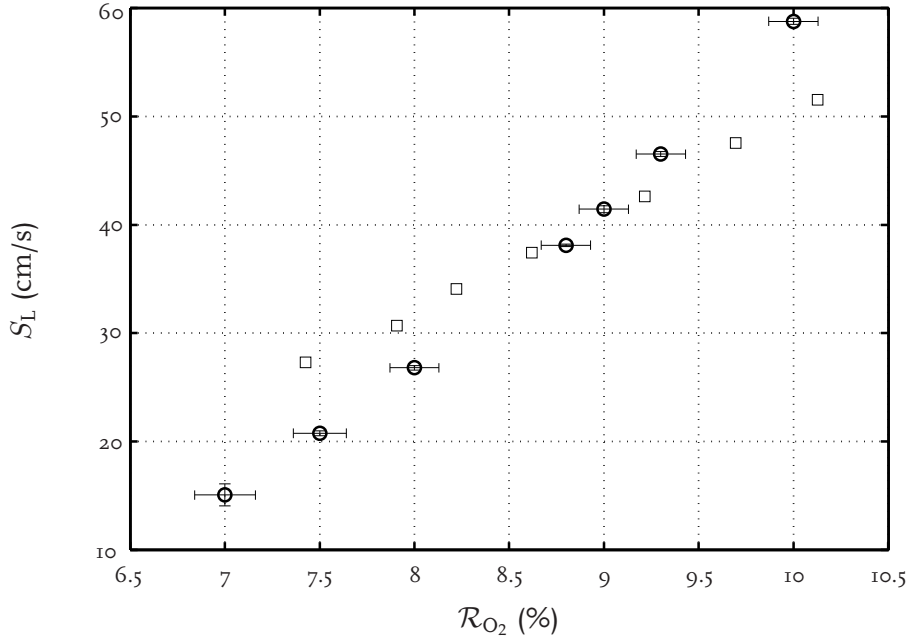


Figure 4.4: Laminar burning velocities measurements of hydrogen-oxygen-nitrogen flames at $\phi = 1.06$ with varying oxidiser content R_{O_2} at ambient conditions ($T_u = 298$ K and $p_u = 1$ atm). The circles denote present measurements with the heat flux method and the squares are measurements of Egolfopoulos and Law [26].

4.2.1 Results

This section which describes the laminar burning velocity of hydrogen-oxygen-nitrogen mixtures is based on the article *Laminar Burning Velocities of Diluted Hydrogen-Oxygen-Nitrogen Mixtures* by Hermanns et al. [48]. In figure 4.4 the results with varying oxygen content in the oxidiser and constant equivalence ratio, $\phi = 1.06 \pm 0.02$, are shown. The error estimate for the oxygen fraction varies between 0.1 and 0.2%. The largest error occurs at highly diluted mixtures by nitrogen, $R_{O_2} = 7.0\%$. This is due to the fact that here the mass flow controllers have been used in a very low working range ($< 20\%$); the mass flow rates for hydrogen and oxygen become small in this area. In appendix B.2 it is shown that with lower mass flows the uncertainty of the mass flow controller increases. The error estimate for the laminar burning velocity varies between 0.1 and 1.0 cm/s. In this case the largest uncertainty in the measurements occurs also at mixtures which are highly diluted by nitrogen; $R_{O_2} = 7.0\%$.

When comparing the experimental results of Egolfopoulos and Law [26] with results of the heat flux method, the latter show lower laminar burning velocities for an oxygen fraction up to $R_{O_2} = 9\%$, whereas above an oxygen content of 9% the present results become higher than the data of Egolfopoulos and Law. The largest difference between the experimental results in the present range of measurements is found at the boundaries of the measurement area: $R_{O_2} = 7.5\%$ and 10.0% where it is approximately 6 cm/s at both sides. It should be emphasised that this discrepancy between the measurements of Egolfopoulos and Law and the heat flux method is not only outside the presented

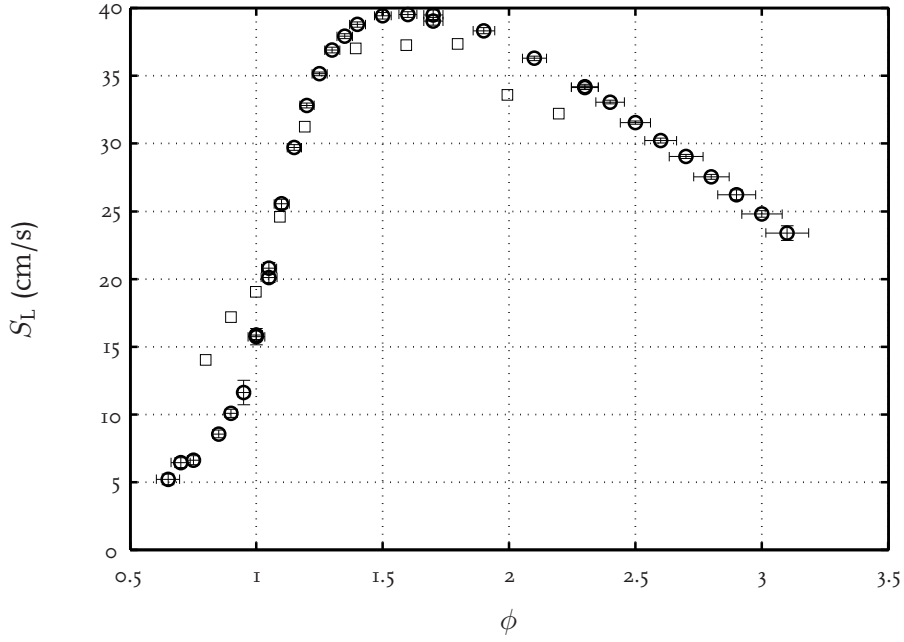


Figure 4.5: Experimental results of hydrogen-oxygen-nitrogen flames at $\mathcal{R}_{O_2} = 7.7\%$ with varying equivalence ratio. The circles denote present measurements with the heat flux method and the squares are measurement of Egolfopoulos and Law [26].

uncertainty estimates of the heat flux burner, but also outside the uncertainty estimate of the counterflow twin-flame technique. This latter one was estimated by Egolfopoulos and Law [26] to be 1 - 2 cm/s for burning velocities less than 60 cm/s. They assumed that this uncertainty was determined by the accuracy of the LDV method.

Measurements of laminar burning velocities with varying equivalence ratio and constant dilution ratio of $\mathcal{R}_{O_2} = 7.7\%$ are presented in figure 4.5. The error estimate, $\Delta\phi$, determined with the heat flux method ranges from 0.02 to 0.08. The maximum $\Delta\phi$ occurs at $\phi = 3.10$ and the minimum $\Delta\phi$ occurs at $\phi = 0.80$. The uncertainty in the laminar burning velocity, ΔS_L , varies between 0.1 and 0.9 cm/s. Here the maximum ΔS_L occurs at $\phi = 0.95$ whereas the minimum value occurs at $\phi = 2.30$.

The experimental results of Egolfopoulos and Law [26] are also shown in figure 4.5. The data of Egolfopoulos and Law on the lean side show significantly higher burning velocities, the discrepancy reaches up to 6 cm/s. At stoichiometry and toward slightly fuel rich conditions the measured values of both the heat flux method and the counterflow measurements of Egolfopoulos and Law are comparable. At equivalence ratios above $\phi = 1.4$ the measurements with the counterflow method are below the heat flux results. The difference in this area is about 3 cm/s which is just outside the expected experimental uncertainty of the counterflow method [26].

The last set of measurements of hydrogen-oxygen-nitrogen flames are performed with $\mathcal{R}_{O_2} = 10.7\%$. Results of these measurements are shown in figure 4.6, where $\Delta\phi$ is 0.02 for the entire measurement range and ΔS_L varies from 0.2 at $\phi = 0.95$ to 1.6 cm/s for the lean flame at $\phi = 0.70$.

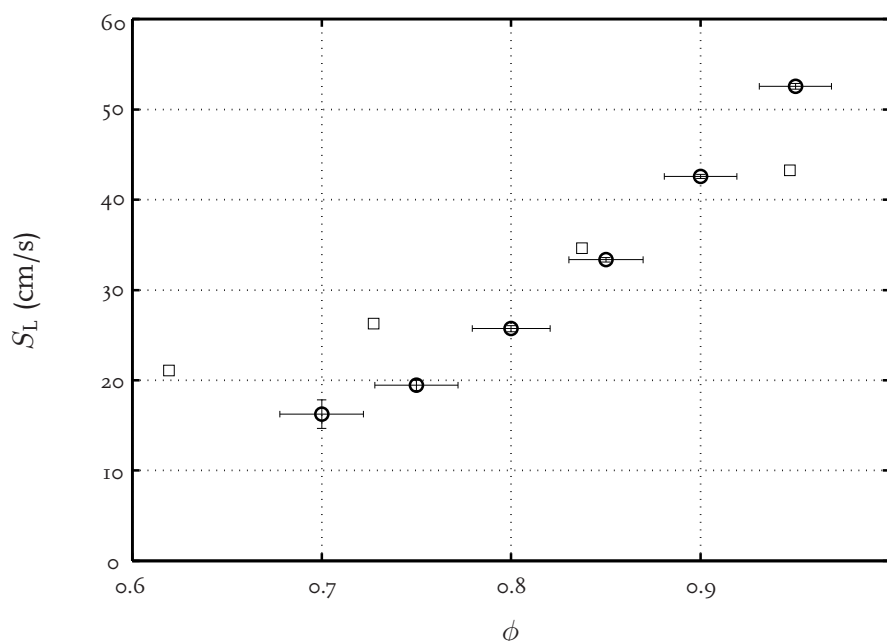


Figure 4.6: Experimental results of hydrogen-oxygen-nitrogen flames at $\mathcal{R}_{O_2} = 10.7\%$ with varying equivalence ratio. The circles denote present measurements with the heat flux method and the squares are measurement of Egolfopoulos and Law [26].

For these lean flames the data of Egolfopoulos and Law show higher burning velocities than the presented heat flux results, similar as for $\mathcal{R}_{O_2} = 7.7\%$. Above an equivalence ratio of $\phi = 0.90$ the situation changes and the heat flux results show higher burning velocities in comparison to the counterflow data. Near an equivalence ratio of 0.95 the maximum difference in the laminar burning velocity is about 10 cm/s.

4.2.2 Discussion

In the present investigation new measurements for the laminar burning velocity of flames propagating in hydrogen-oxygen-nitrogen mixtures using the heat-flux method are presented and analysed. A comparison of the heat flux measurements with experimental results obtained using the counterflow twin-flame technique [26] showed a discrepancy outside the experimental errors.

It is interesting to note that the deviation with the measurements obtained by the counterflow twin-flame technique [26] and compared with the results using the heat flux method in non-stretched flames changes its sign at an equivalence ratio around 0.9. Davis and Searby [19] demonstrated recently that the Markstein number in hydrogen-air flames also changes sign in these slightly lean mixtures. The Markstein number reflects the stability of flames, a positive value indicates that the burning velocity decreases with increasing stretch rate. Small disturbances at the flame front will be suppressed, making the flame stable. In contrast to this, a negative value of the Markstein number means that the burning velocity is increasing with increasing stretch rate. In this case small disturbances appearing at the flame front increase the local flame speed and make the flame unstable.

Table 4.1: Overview of available data of methane-hydrogen-air laminar burning velocity measurements in literature using several measurements techniques and hydrogen contents.

Author	Year	Methodology	\mathcal{R}_{H_2} (%)
Present measurements	2007	Heat flux	0, 10, 20, 30, 40
Coppens et al. [17]	2007	Heat flux	0, 5, 15, 25, 35
Huang et al. [52]	2006	Constant volume	0, 20, 40
Halter et al. [42]	2005	Constant volume	0, 10, 20
Tanoue et al. [103]	2003	Constant volume	0, 20, 40
Haniff et al. [43]	1989	Flat flame	0, 5, 10, 15, 20, 30, 35, 40
Yu et al. [116]	1986	Counterflow	0, 10, 20, 30, 40

For intermediate stretch values the perturbations on the burning velocity have a non-linear behaviour; this is shown by van Maaren and de Goey [74]. One might expect therefore that the linear extrapolation to zero stretch rate [26] might be an important reason for the discrepancy between the experimental results shown in figures 4.4, 4.5 and 4.6. This has been recognised and demonstrated by Vagelopoulos et al. [106] for hydrogen-air flames where a significant uncertainty occurs when using the method of linear extrapolation to zero stretch rate. They showed that a non-linear correction was more accurate. The difference between corrected and non-corrected laminar burning velocities increases towards leaner hydrogen-air mixtures. Regrettably, the results obtained by Egolfopoulos and Law [26] in hydrogen-oxygen-nitrogen mixtures with varying oxygen content have not been corrected for these non-linear effects.

4.3 Methane-Hydrogen-Air Flames

In this section laminar burning velocity measurements of methane-hydrogen-air flames at ambient conditions are presented. The amount of hydrogen in the fuel is varied for the measurements presented in this section. This hydrogen ratio in the fuel is defined as:

$$\mathcal{R}_{\text{H}_2} = \frac{X_{\text{H}_2}}{X_{\text{H}_2} + X_{\text{CH}_4}} \cdot 100\%. \quad (4.2)$$

It ranges from 0 to 40%. The equivalence ratio was varied typically between 0.6 and 1.5 at ambient conditions. The presented measurements with the heat flux burner will be compared with data of other experimentalists in this section. The experimental methodology to determine the laminar burning velocity as is used in this thesis is shown in table 4.1 together with the author name, the year of publication and the hydrogen enrichment of the fuel.

4.3.1 Results

The experimental results obtained with the heat flux method for the different hydrogen fractions in the fuel stream are shown in figure 4.7. It is clear that the laminar burning

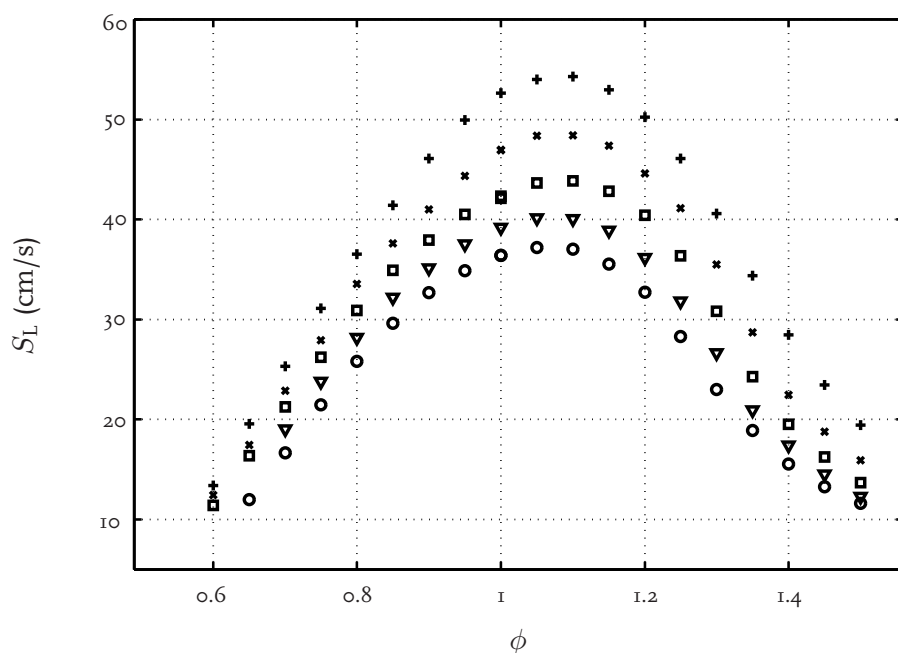


Figure 4.7: Experimental data of the laminar burning velocity of methane-hydrogen-air flames measured with the heat flux burner for hydrogen contents of $R_{H_2} = 0, 10, 20, 30$ and 40% denoted with $\circ, \nabla, \square, \times, +$ respectively.

velocity increases by increasing the amount of hydrogen in the mixture. For a stoichiometric mixture, the laminar burning velocity increases from 36.4 cm/s (at $R_{H_2} = 0\%$) to 39.2 cm/s (at $R_{H_2} = 10\%$), 42.3 cm/s (at $R_{H_2} = 20\%$), 47.0 cm/s (at $R_{H_2} = 30\%$) and 53.5 cm/s (at $R_{H_2} = 40\%$).

In figures 4.8 - 4.12 the results are also shown for the different hydrogen fractions separately. The error estimates in the burning velocities as obtained by the heat flux method are also presented in these figures together with the uncertainties in the equivalence ratio. Typically the uncertainty in the equivalence ratios is less than 0.06 for the entire range. The error in the laminar burning velocity is less than 1.1 cm/s for the entire measurement range. However, close to an equivalence ratio of 1.0 the errors become smaller. In this area the errors are typically less than 0.3 cm/s for the laminar burning velocity and less than 0.04 for the equivalence ratio.

Besides the present experimental data determined with the heat flux method, the figures 4.8 - 4.12 show the experimental results obtained by other investigators. A comparison between the different results will be presented in this section.

Methane-air flames

Heat flux measurements of laminar burning velocities with varying equivalence ratio of methane-air flames are presented in figure 4.8. The error estimate of the equivalence ratio, $\Delta\phi$, ranges from 0.01 to 0.03 for methane-air flames. The maximum $\Delta\phi$ occurs at $\phi = 1.50$ and the minimum $\Delta\phi$ occurs at $\phi = 0.80$. In the case of the uncertainty in the laminar burning velocity, ΔS_L , the values vary between 0.1 and 0.8 cm/s . Here the

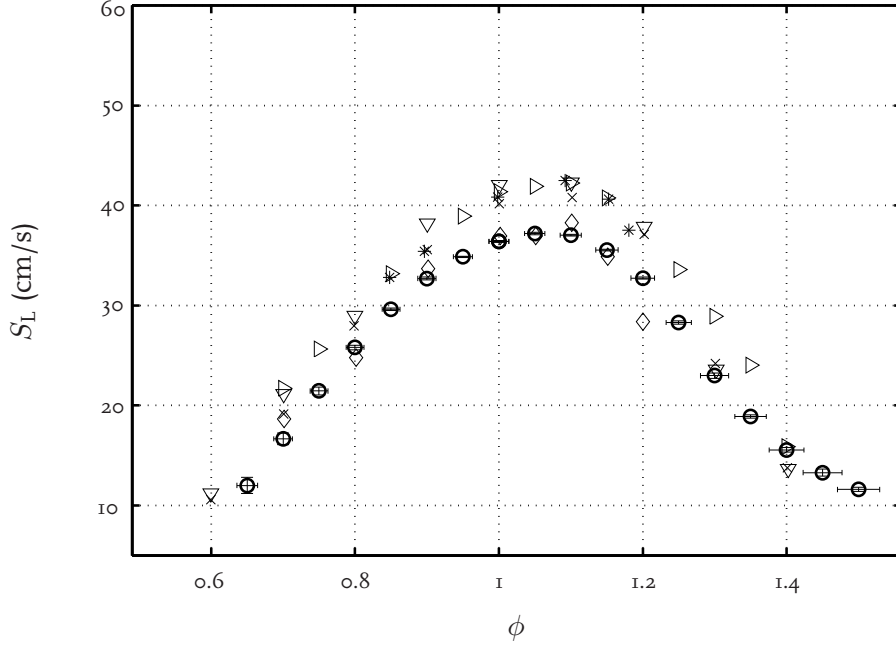


Figure 4.8: Laminar burning velocities of methane-air mixtures, $\mathcal{R}_{H_2} = 0\%$. The symbols are: \circ , Heat flux measurements with error estimates; Yu [116], \triangleright ; Haniff [43], $*$; Tanoue [103], ∇ ; Halter [42], \diamond and Huang [52], \times .

maximum uncertainty in the laminar burning velocity occurs at $\phi = 0.65$ whereas the minimum value occurs at $\phi = 0.95$.

In literature a significant amount of measurement data of methane-air flames can be found, see e.g. figure 4.1. In figure 4.8 only experimental data of authors which have measured methane-hydrogen-air mixtures are presented, Yu et al. [116], Haniff et al. [43], Tanoue et al. [103], Halter et al. [42], and Huang et al. [52]. The data of Halter et al. is most close to the present results. The difference in laminar burning velocity of Halter et al. and the heat flux data are within approximately 1 cm/s for the measured range. Only at an equivalence ratio of 0.7 and 1.2 the difference is larger; 2 and 4 cm/s respectively. The measured laminar burning velocity of Halter et al. at $\phi = 1.2$ is low, even compared to the experimental results of other authors. Overall the data of Halter et al. agree quite well with the heat flux results. The data of the other authors, Yu et al. [116], Haniff et al. [43], Tanoue et al. [103] and Huang et al. [52] show higher burning velocities compared to the heat flux method for fuel lean mixtures up to slightly fuel rich mixtures ($\phi = 1.2$). This difference can be as large as 5 cm/s for stoichiometric flames. In the case of fuel rich flames, with an equivalence ratio larger than 1.3, the difference between the measured results using the heat flux method and the experimental data determined by Haniff et al., Tanoue et al. and Huang et al. is less than 2 cm/s. Although the difference with the selected experimental data can be significant, the heat flux measurements are comparable with other recent methane-air data, see figure 4.1 and e.g. [9, 17, 42].

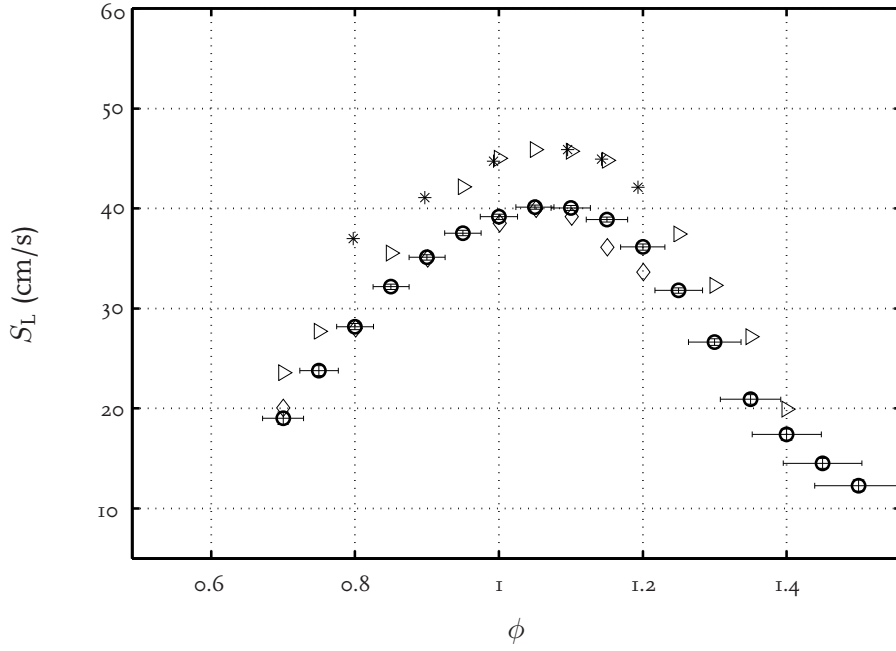


Figure 4.9: Laminar burning velocities of methane-hydrogen-air mixture using a hydrogen content of $\mathcal{R}_{\text{H}_2} = 10\%$. The symbols denote: \circ Heat flux measurements with error estimates; Yu [116], \triangleright ; Haniff [43], $*$; Halter [42], \diamond .

Methane-hydrogen-air flames ($\mathcal{R}_{\text{H}_2} = 10\%$)

Results of laminar burning velocity measurements with a hydrogen enrichment of $\mathcal{R}_{\text{H}_2} = 10\%$ are shown in figure 4.9. Here the error estimate for the heat flux data in the equivalence ratio varies between 0.03 and 0.06 with a maximum of 0.06 at an equivalence ratio of 1.50. Compared to the methane results in figure 4.8 and previous publications [8, 9] the error estimate in the equivalence ratio is relatively large. This is partly due to the additional mass flow controller for the hydrogen mass flow, but also induced by the low working range of this mass flow controller for the present measurements with $\mathcal{R}_{\text{H}_2} = 10\%$. Both add up and result in an increased uncertainty in the equivalence ratio, see also equation (3.10). The uncertainty in the laminar burning velocity ranges between 0.2 and 0.6 cm/s. The smallest uncertainty occurs at an equivalence ratio of 1.05 and the largest uncertainty occurs at $\phi = 0.70$.

The data of Halter et al. [42] shown in figure 4.9 are for fuel lean flames in good agreement with the heat flux results. The fuel lean data of Halter are difficult to recognise in the figure because they are close to the heat flux data. For rich flames the data of Halter et al. show ≈ 3 cm/s lower laminar burning velocities. Note that this lower burning velocity is also found for fuel rich flames in the pure methane situation. The experimental data of Haniff et al. [43] in figure 4.9 show a significantly higher burning velocity compared to the heat flux results. Haniff et al. estimated their uncertainty in the measurements as $\pm 3.5\%$, which is approximately 0.7 to 2 cm/s for the methane-hydrogen-air flames investigated in this thesis. In general the laminar burning velocities of Haniff et al. are ≈ 6 cm/s faster than the heat flux results; this discrepancy is slightly larger than in the case of methane-air flames. The measurements of Yu et al. [116]

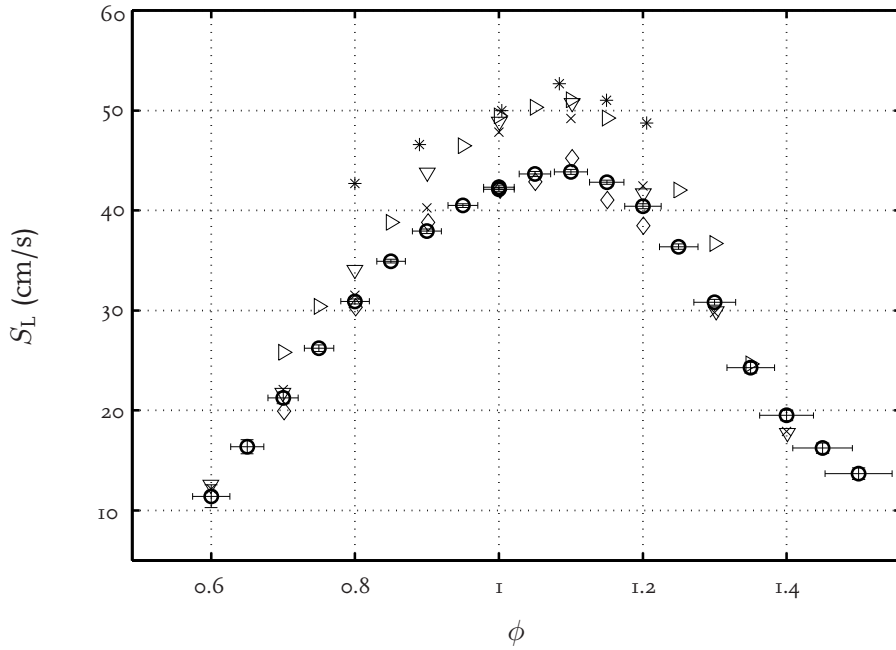


Figure 4.10: Laminar burning velocities of methane-hydrogen-air mixture using a hydrogen content of $\mathcal{R}_{H_2} = 20\%$. The symbols denote: \circ Heat flux measurements with error estimates; Yu [116], \triangleright ; Haniff [43], $*$; Tanoue [103], ∇ ; Halter [42], \diamond ; Huang [52], \times .

in figure 4.9 give higher burning velocities than the heat flux data. The difference for stoichiometric flames is ≈ 6 cm/s.

Methane-hydrogen-air flames ($\mathcal{R}_{H_2} = 20\%$)

In the case of a hydrogen dilution of $\mathcal{R}_{H_2} = 20\%$, the laminar burning velocity measurements with the heat flux burner are shown in figure 4.10. The error estimate of the equivalence ratio is between 0.02 and 0.05 with the lowest uncertainty occurring at an equivalence ratio of 0.85 and the highest uncertainty at an equivalence ratio of 1.50. The resulting error estimates for the laminar burning velocity are between 0.2 and 1.1 cm/s at an equivalence ratio of 0.95 and 0.60 respectively.

Comparing the laminar burning velocities measured by Halter et al. [42] with 20 mol% of hydrogen enrichment with the heat flux results show a difference less than 2 cm/s with a maximum difference at $\phi = 1.20$. Similar as in the pure methane situation the results of Haniff et al. [43] and Huang et al. [52] for $\mathcal{R}_{H_2} = 20\%$, show a higher laminar burning velocity compared to the heat flux method in figure 4.10. The data presented by Yu et al. [116] and Tanoue et al. [103] show a larger burning velocity between an equivalence ratio of 0.80 and 1.10, with a maximum difference of 7 cm/s at $\phi = 1.10$. In the case of very lean flames, lower than $\phi = 0.8$, the difference between the heat flux results and the data of Tanoue et al. is significantly smaller, ≈ 1 cm/s. Also on the fuel rich side, $\phi > 1.2$ this difference is smaller, ≈ 2 cm/s.

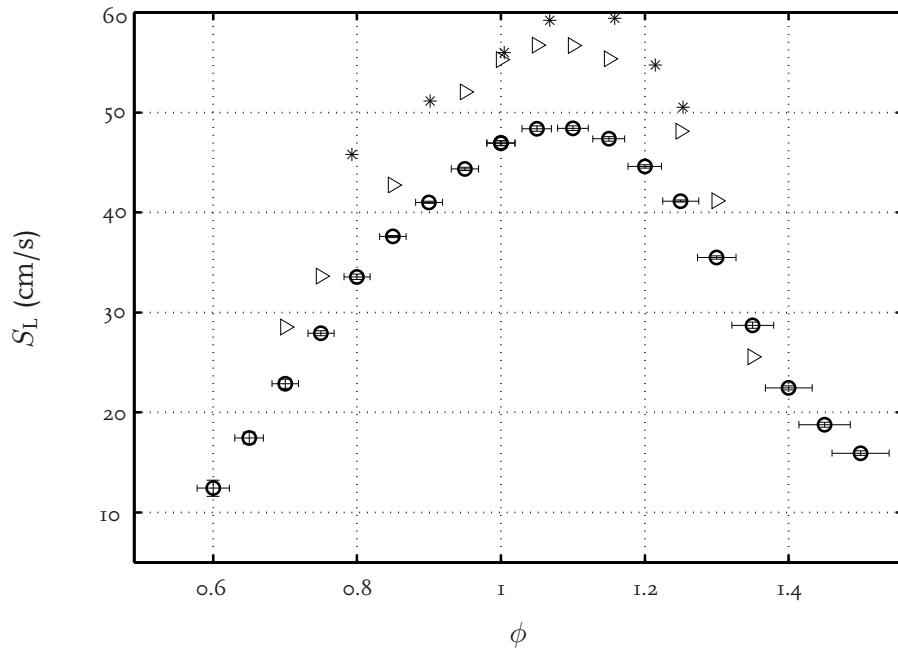


Figure 4.11: Laminar burning velocities of methane-hydrogen-air mixture using a hydrogen content of $\mathcal{R}_{H_2} = 30\%$. The symbols denote: \circ Heat flux measurements with error estimates; Yu [116], \triangleright ; Haniff [43], $*$

Methane-hydrogen-air flames ($\mathcal{R}_{H_2} = 30\%$)

Experimental data for $\mathcal{R}_{H_2} = 30\%$ of hydrogen enrichment are presented in figure 4.11. The heat flux error estimates for the equivalence ratio are slightly smaller than for 10 and 20 mol% of hydrogen enrichment. In figure 4.11 they are typically between 0.02 and 0.04. The uncertainties in the laminar burning velocity are typically between 0.1 and 0.8 cm/s. From the authors used as a reference in this thesis only Yu et al. [116] and Haniff et al. [43] measured laminar burning velocities of methane-hydrogen-air mixtures with $\mathcal{R}_{H_2} = 30\%$ of hydrogen enrichment. Compared to the present heat flux results the measured laminar burning velocity by Yu et al. and Haniff et al. are significantly higher, up to 12 cm/s. This overprediction compared to the heat flux data is consistent with lower contents of hydrogen in the fuel, see figures 4.8 - 4.10.

Methane-hydrogen-air flames ($\mathcal{R}_{H_2} = 40\%$)

The last set of measurements of laminar burning velocities of methane-hydrogen-air mixtures at ambient conditions is shown in figure 4.12. In this figure the experimental data of heat flux measurements with a hydrogen content of $\mathcal{R}_{H_2} = 40\%$ are presented. The uncertainty in the equivalence ratio is between 0.02 and 0.05 which is comparable with the uncertainties presented of hydrogen enriched methane-air flames for $\mathcal{R}_{H_2} = 10, 20$ and 30% of hydrogen. The laminar burning velocities measured by Yu et al. [116], Haniff et al. [43], Tanoue et al. [103] and Huang et al. [52] are generally higher than the heat flux data; between an equivalence ratio of 0.80 and 1.20 this difference can be as large as 10 cm/s. Below $\phi = 0.8$ and above $\phi = 1.2$ this difference is smaller and less than

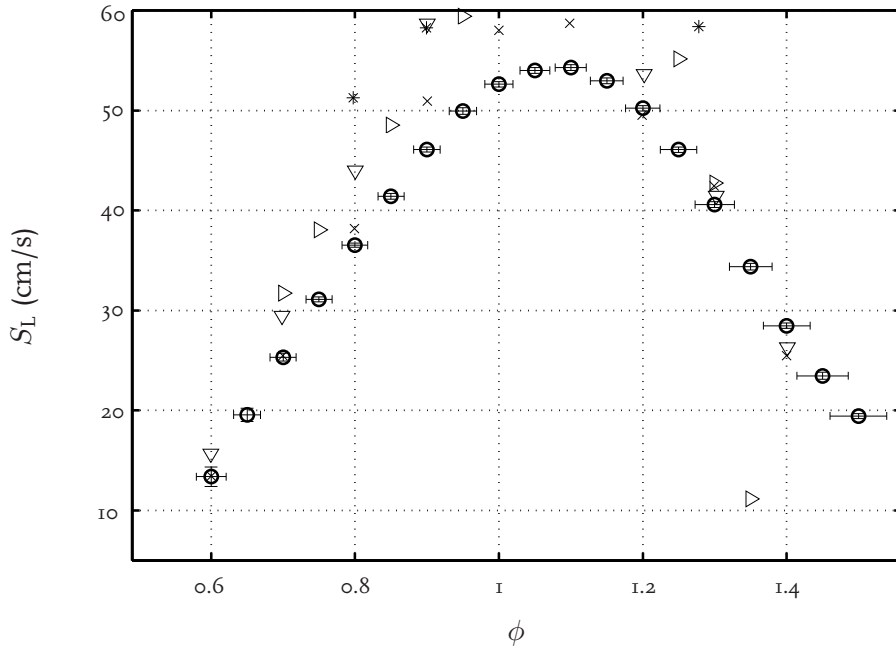


Figure 4.12: Laminar burning velocities of methane-hydrogen-air mixture using a hydrogen content of $R_{H_2} = 40\%$. The symbols denote, \circ Heat flux measurements with error estimates; Yu [116], \triangleright ; Haniff [43], $*$; Tanoue [103], ∇ ; Huang [52], \times .

4 cm/s. Note that for the highest burning velocities a few measured data points of Yu et al. and Tanoue et al. are just outside the plotted range.

4.3.2 Anomalies observed during measurements

At fuel rich mixtures ($\phi > 1.4$) the flames observed are not perfectly flat. Typically it is seen that the flame is curved at the edges of the burner plate as is shown in figure 4.13. The top figure shows a flat flame front of a strongly stabilised flame. After increasing the gas velocity the flame detaches from the edge of the burner plate. For even higher gas velocity, but still burner stabilised flames, a curved flame geometry is occurring which is seen in the bottom figure of figure 4.13. Due to these curved flames, a flame surface is found that is larger than expected and the laminar burning velocity is less accurately determined and becomes overestimated. The significant increased flame surface perturbs the error analysis presented in chapter 3. Therefore the heat flux results for equivalence ratios larger than $\phi = 1.4$ should be taken with care. The resulting error estimate for these fuel rich flames is probably slightly underpredicted. The exact error estimate is difficult to determine due to the fact that the flame surface area is not well defined anymore.

4.3.3 Discussion

In this section laminar burning velocity measurements of hydrogen enriched methane-air flames determined with the heat flux burner have been presented and analysed. The comparison of the laminar burning velocities in this thesis is restricted to experimental

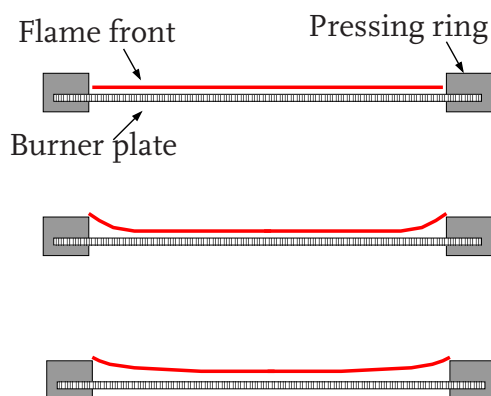


Figure 4.13: Typical flame shapes for mixtures with an equivalence ratio larger than ≈ 1.4 . The gas velocity increases from the top figure to the bottom figure.

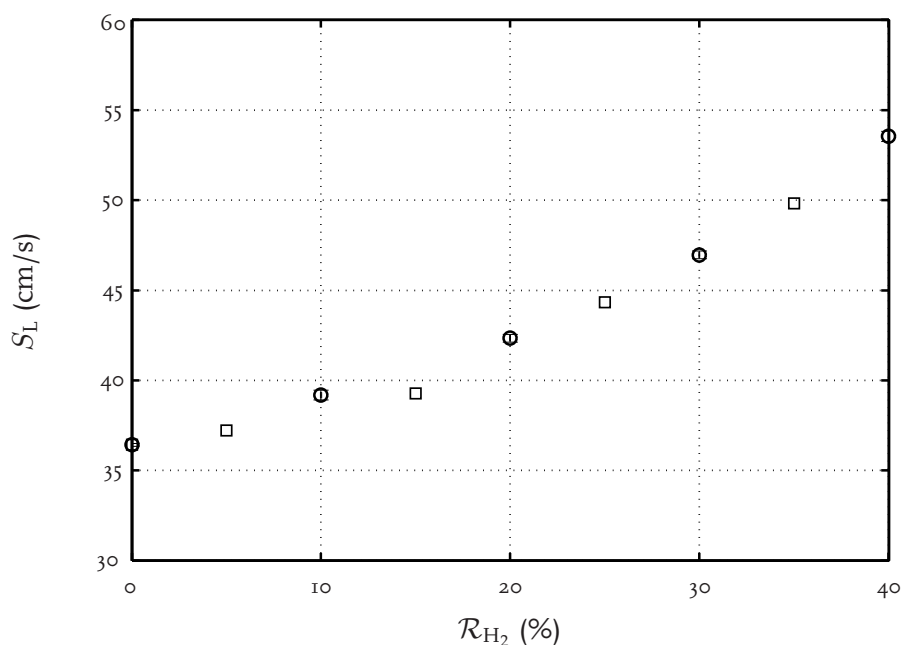


Figure 4.14: Experimental results of laminar burning velocities of stoichiometric methane-hydrogen-air flames as a function of the hydrogen content. The heat flux measurements are denoted with a circle and error estimate, the results of Coppens are denoted with squares.

results of authors who have measured methane-hydrogen-air flames as well. In the case of methane-air flames, recent work of several authors showed that the heat flux burner measurements gives comparable burning velocities; see e.g. the work of Bosschaart and de Goey [9] and Coppens et al. [17]. In figure 4.14 the present laminar burning velocity measurements are plotted together with the results Coppens et al. for hydrogen contents of $R_{H_2} = 0, 5, 15, 25$ and 35% . The laminar burning velocity increase is for both experimental results similar. However, the laminar burning velocity of $R_{H_2} = 15$ slightly underpredicted by Coppens et al. [17] compared to the present results. For methane-hydrogen-air flames the overall agreement between the results of the heat flux method and the measurements of other authors is satisfactory. The recently presented data of Halter et

al. [42] show minor differences, less than 1% for stoichiometric flames, compared to the heat flux measurements. For equivalence ratios larger than 1.2 the measurement of Halter et al. is low compared to present heat flux measurements. The measurements of Haniff et al. [43] and Huang et al. [52] cover the complete presented measurement range. Already for methane-air flames, the data of Haniff et al. [43] show higher burning velocities and the difference increases at higher hydrogen contents. The measurements by Huang et al. [52] are not performed with methane-air mixtures, but with a natural gas mixture consisting of 96.16 vol% methane and traces of ethane, propane and nitrogen. Generally, ethane and propane have slightly higher burning velocities compared to methane [7] whereas nitrogen reduces the laminar burning velocity.

It should be emphasised that a comparison gives good results only if a non-linear stretch correction is used for flames which do not have a flat flame. This has already been recognised by Vagelopoulos et al. [106] who showed for the counterflow technique that the resulting burning velocity of methane-air flames significantly reduces (typically 10%) in the case that a non-linear stretch correction is applied. Both Yu et al. [116] and Tanoue et al. [103] used the counterflow twin flames measurement technique, but did not correct for stretch in a non-linear manner. This leads to an over-prediction of the laminar burning velocities compared to the heat flux data; also for higher hydrogen fractions. For methane-air mixtures the over-prediction typically fluctuates around 10% compared to the currently accepted data in literature over the entire equivalence range. An over-estimation of 10% is also found with the measurements of Haniff et al. [43], although they used a flat burner.

To make a comparison for the influence of hydrogen on the burning velocity the ratio between the measurements of several authors and the heat flux method are computed for stoichiometric methane-air flames and stoichiometric methane-hydrogen-air flames (table 4.2). The scaled burning velocity of Huang et al. [52] and Halter et al. [42] does not change much when adding hydrogen, less than 3%. This is different for the results of Tanoue et al. [103], Haniff et al. [43] and Yu et al. [116] where the scaled laminar burning velocity increases with hydrogen content. According to Law [67] it was expected that for hydrogen enriched methane-air flames the non-linear stretch contribution becomes less important. These methane-hydrogen-air flames are rather thin and less susceptible to the non-linear stretch effects because the strength of the stretch depends on the dimension of the nozzle separation distance and hence implicitly the flame thickness [67]. In table 4.2 the results of Tanoue et al. [103], Haniff et al. [43] and Yu et al. [116] show a different behaviour than expected. The ratio between the burning velocities increases with increasing hydrogen content. This can partly be explained by the change of sign of the Markstein number for stoichiometric methane-hydrogen-air flames around $\mathcal{R}_{H_2} = 40\%$; which is shown recently by van den Schoor [90]. For these highly hydrogen enriched methane-air flames the laminar burning velocity is becoming more susceptible to cellular structure formation which enlarge the laminar burning velocity.

Table 4.2: Scaling factors of available data of stoichiometric methane-hydrogen-air laminar burning velocity measurements found in literature using several measurements techniques. The reference value, $S_{L,HF}$ is the laminar burning velocity of the heat flux method.

Author	methodology	$S_L/S_{L,HF}$	$S_L/S_{L,HF}$	$S_L/S_{L,HF}$
		$\mathcal{R}_{H_2} = 0\%$	$\mathcal{R}_{H_2} = 20\%$	$\mathcal{R}_{H_2} = 40\%$
Present measurements	Heat flux	1	1	1
Huang et al. [52]	Constant volume	1.10	1.13	1.10
Halter et al. [42]	Constant volume	1.01	0.99	—
Tanoue et al. [103]	Constant volume	1.15	1.15	1.19
Haniff et al. [43]	Flat flame	1.12	1.18	1.21
Yu et al. [116]	Counterflow	1.13	1.17	1.21

4.4 Temperature Dependency of Methane-Hydrogen-Air Flames

In this section laminar burning velocities of methane-hydrogen-air mixtures at increased unburnt gas temperature as measured with the heat flux burner are reported. Generally the heat flux setup uses water to keep the plenum chamber and heating jacket at constant temperature (see figure 3.4a). Using water as a heating medium limits the maximum temperature to ≈ 350 K. The heat flux setup is modified in order to measure laminar burning velocities at unburnt gas temperatures higher than 350 K by using synthetic oil as heating medium.

The temperature dependency of the burning velocity is determined for three equivalence ratios ($\phi = 0.8, 1.0$ and 1.2). The unburnt gas temperature is increased from 298 K to 418 K. This upper value is still a restriction induced by the heat flux equipment; some parts of the burner head are glued with tin which has a melting point of ≈ 450 K. Furthermore, a value of ≈ 60 cm/s is taken as an upper limit for the unburnt gas velocity, because for higher gas velocities a 1D flat flame is not guaranteed anymore [37]. In the figures presented in this section the error estimate is not shown because the error estimate is small and difficult to distinguish from the presented data. For completeness the experimental data with error estimates is listed in appendix E.

4.4.1 Results

Experimental results of laminar burning velocities, determined with the heat flux method, of stoichiometric hydrogen enriched methane-air flames as a function of the unburnt gas temperature are shown in figure 4.15. The hydrogen content in the fuel varies between $\mathcal{R}_{H_2} = 0, 10, 20$ and 30% . The laminar burning velocity as a function of the unburnt gas temperature is increasing with ≈ 0.22 cm s⁻¹ K⁻¹ for stoichiometric methane-air flames and is slightly larger with increasing amount of hydrogen in the fuel. For mixtures of $\mathcal{R}_{H_2} = 30\%$ this increase is ≈ 0.26 cm s⁻¹ K⁻¹.

The error estimates of the burning velocities as obtained by the heat flux method are also

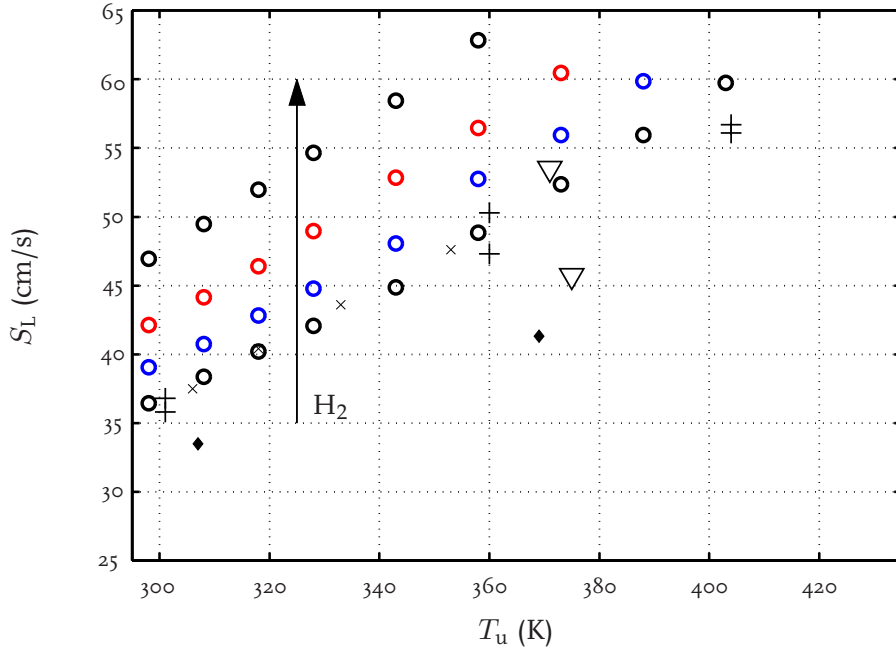


Figure 4.15: Experimental results of the laminar burning velocity of methane-hydrogen-air flames as a function of the unburnt gas temperature T_u at an equivalence ratio of $\phi = 1.0$. The symbols denoted with a \circ are measured with the heat flux burner for hydrogen contents of $\mathcal{R}_{H_2} = 0, 10, 20$ and 30% . The other symbols denote methane-air measurements of Bosschaart [7], \times and Gu et al. [39], $+$; Dugger et al. [23], \blacklozenge ; Barassin et al. [3], ∇ .

presented in figure 4.15 together with the uncertainties in the unburnt gas temperature. The uncertainty of the unburnt gas temperature is taken as ± 1 K which is based on thermocouple measurements inside the plenum chamber. The error in the laminar burning velocity is less than 0.5 cm/s for the entire measurement range. The uncertainty in laminar burning velocity is slightly larger for the measurements performed with synthetic oil ($T_u \geq 343$ K) as transport medium of the heating jacket. The typical uncertainty for synthetic oil as heating medium is ≈ 0.4 cm/s whereas for water this is ≈ 0.2 cm/s. When using oil the time needed to achieve a more or less constant temperature reading is taking longer compared to water.

In literature recent measurements of the laminar burning velocities as a function of the unburnt gas temperature are scarce. For stoichiometric methane-air mixtures measurements of Bosschaart [7] and Gu et al. [39] Dugger et al. [23], and Barassin et al. [3] are shown in figure 4.15. Comparing these data with the present measured heat flux results for stoichiometric methane-air mixtures shows large differences. The methane-air data of Gu et al. [39], Dugger et al. [23], and Barassin et al. [3] are considerable scattered, for example the difference between both measurements of Gu et al. at an unburnt gas temperature of 360 K is approximately 4 cm/s. The measurements of Bosschaart [7] using a heat flux burner are comparable with the present measurements. Bosschaart used water as heating medium, resulting in a restriction of the equipment to $T_u = 353$ K.

The measured laminar burning velocities of methane-hydrogen-air flames at an

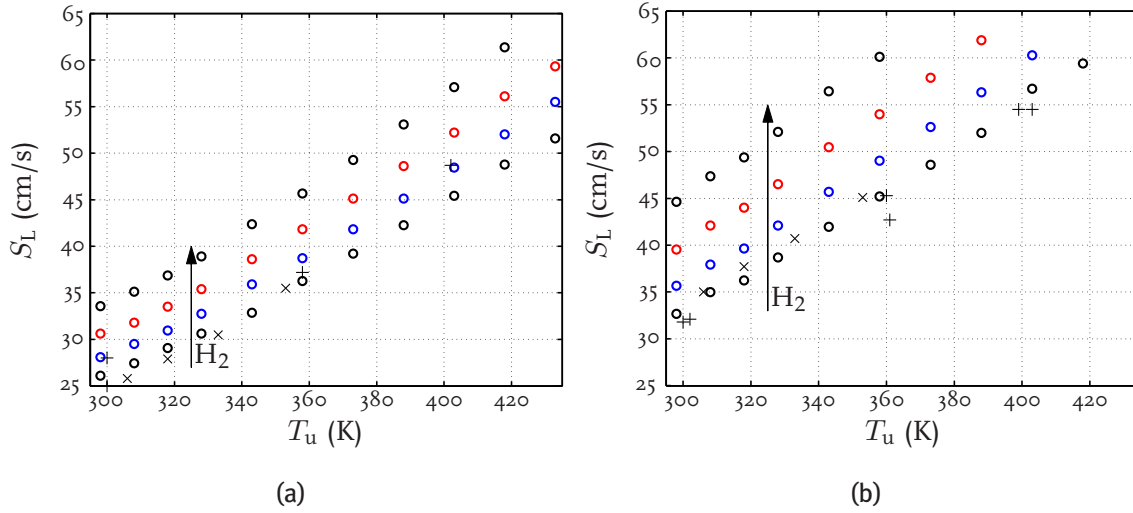


Figure 4.16: Experimental results of the laminar burning velocity of methane-hydrogen-air flames as a function of the unburnt gas temperature T_u at an equivalence ratio of $\phi = 0.8$ (left) and $\phi = 1.2$ (right). The symbols denoted with a \circ are measured with the heat flux burner for hydrogen contents of $\mathcal{R}_{H_2} = 0, 10, 20$ and 30%. The other symbols denote methane-air measurements of Bosschaart [7], \times and Gu et al. [39], $+$.

equivalence ratio of $\phi = 0.80$ are shown in figure 4.16a. For these lean flames the measured laminar burning velocity with the heat flux burner as a function of the unburnt temperature is increasing with $0.19 \text{ cm s}^{-1} \text{ K}^{-1}$ for methane-air flames and $0.21 \text{ cm s}^{-1} \text{ K}^{-1}$ for methane-hydrogen-air flames ($\mathcal{R}_{H_2} = 30\%$). The minimum uncertainty in the laminar burning velocity is 0.1 cm/s . The maximum uncertainty, 1.0 cm/s , is measured when using a hydrogen content of $\mathcal{R}_{H_2} = 20\%$ at an unburnt gas temperature of 373 K .

The experimental data of other authors in figure 4.16a tend to agree well with the present heat flux data. The methane-air measurements of Bosschaart [7] are somewhat lower, $\approx 1 \text{ cm/s}$, than the present heat flux data. This is probably due to an inconsistent use of the oxygen content in air (mole based or mass based) which is solved in the present measurements. The experimental results of methane-air flames by Gu et al. [39] show also here for these lean flames large scatter.

Finally, laminar burning velocities determined with the heat flux burner at an equivalence ratio of $\phi = 1.20$ are shown in figure 4.16b. In the case of methane-air flames with increasing unburnt gas temperature the laminar burning velocity is increasing with $0.22 \text{ cm s}^{-1} \text{ K}^{-1}$. For the methane-hydrogen-air flames ($\mathcal{R}_{H_2} = 30\%$) this increase is $0.26 \text{ cm s}^{-1} \text{ K}^{-1}$. The minimum error estimates is 0.1 cm/s at an unburnt gas temperature of 318 K for $\mathcal{R}_{H_2} = 10\%$ and the maximum is 0.7 cm/s at an unburnt temperature of 358 K for $\mathcal{R}_{H_2} = 30\%$.

The experimental results of Bosschaart [7] and Gu et al. [39] are also shown in figure 4.16b. The methane-air results of Bosschaart are comparable with the present heat flux data. The burning velocity tends to be slightly higher compared to the present results, probably due

Table 4.3: Laminar burning velocity measurements with the heat flux burner of stoichiometric methane-hydrogen-air flames at ambient conditions. In this table the measurements with a gold coated burner plate and the conventional brass plate are listed.

\mathcal{R}_{H_2} (%)	$S_{\text{L,brass}}$ (cm/s)	$S_{\text{L,gold}}$ (cm/s)
0	36.4 ± 0.1	36.4 ± 0.2
10	39.2 ± 0.3	39.3 ± 0.4
20	42.4 ± 0.2	42.5 ± 0.3
30	47.0 ± 0.2	47.0 ± 0.3
40	53.5 ± 0.3	53.4 ± 0.4

to this inconsistent use of the oxygen content in air. The results of Gu et al. are scattered but tend to have a similar trend in the increase with increasing unburnt temperature as the present heat flux results.

4.4.2 Influence of the burner plate

The influence of the burner plate on the flow pattern, temperature profile and species profile have been analysed numerically by de Goey et al. [37] and experimentally by Bosschaart and de Goey [8] and Dyakov et al. [24]; it was concluded that the burner plate has negligible influence on the laminar burning velocity. However, burner surface reactions were not taken into account. The potential influence of burner surface reactions increases at increased unburnt gas temperatures and increasing hydrogen content because radicals might reach the burner surface and react. These burner surface reactions could affect the measured laminar burning velocity. This possible influence is analysed in this subsection.

In order to analyse the chemical interaction between the gas and the burner plate a gold coated burner plate is used in the heat flux setup instead of brass. This gold coating is chosen to change the possibility of extracting radicals from the gas. The resulting laminar burning velocities for stoichiometric methane-hydrogen-air flames determined with the brass plate and the gold plate are listed in table 4.3. The differences in laminar burning velocity between both types of burner plates is very small and well below the experimental uncertainty. The error estimate is slightly larger for the gold coated burner plate, this is probably due to the conventional thermocouple setup in this gold burner plate. The brass burner plate is using a differential thermocouple measurement method as described by Bosschaart [7]. This differential method has the advantage that the temperature difference is measured directly, which causes a smaller error estimate.

The influence on the burning velocity of chemical reactions occurring on the burner surface is also investigated numerically with CHEM1D. This is done by adjusting the chemical source term for H atom in equation (2.22) to zero at positions in the domain where temperatures are below the plate temperature T_p . The idea behind this is that all H atoms occurring below a certain temperature T_p immediately stick on the burner plate and do not take part anymore in the combustion process; resulting in a H atom

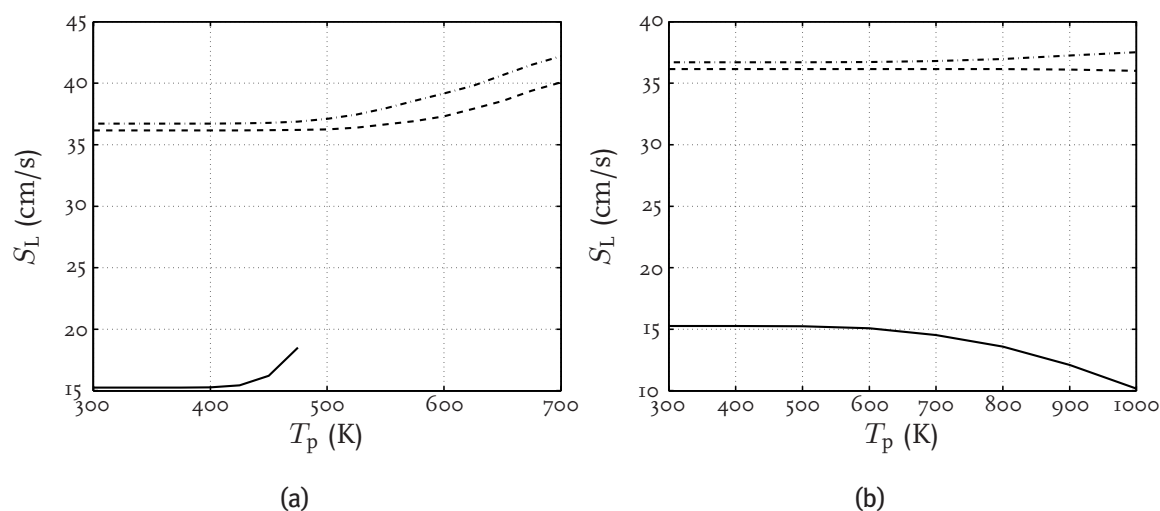


Figure 4.17: Numerical results of the (scaled) laminar burning velocity as a function of the plate temperature T_p . Shown are stoichiometric methane-air flames determined using the Smooke mechanism [98] and GRI-mech 3.0 [97], denoted with a dotted line and dash dotted line respectively. The stoichiometric hydrogen-oxygen-nitrogen flames ($\mathcal{R}_{O_2} = 7.7\%$) using the mechanism of Konnov [61] are denoted with a solid line. The source of H atom is kept zero up till the temperature T_p (left figure), whereas the third body efficiency is increased for temperatures up to T_p (right).

sink. In figure 4.17a the result for three combustion reaction mechanisms is shown. For temperatures below 400 K a negligible effect of H atoms sink on the surface is found. Above this temperature the laminar burning velocity of stoichiometric hydrogen-air flames increases significant due to H atoms sink. In the case of stoichiometric methane-air flames the laminar burning velocity increase occurs at temperatures above ≈ 500 K for both investigated methane-air combustion reaction mechanisms.

In hydrogen flames, diffusivity of H atoms is much higher than that of other species. Hermanns et al. [48] focused on hydrogen flames and investigated numerically this H atoms sink on the surface. The detailed reaction mechanism of Konnov [61] was extended by the following surface reaction, $Sc + H \Rightarrow ScH$, with Sc an artificial scavenger of H atoms. This reaction is only taken into account for temperatures in the domain which are below the plate temperature T_p . It is introduced in the simulations in a very small quantity into the unburnt mixture; below a mole fraction of 10^{-4} . The rate constant of this reaction and amount of scavenger was varied in such a way as to modify the concentration of H atoms at a distance corresponding to a local temperature of 360 K. The variation of H atoms concentration at this temperature in the modelling mimics the possible sink due to surface reactions. This is illustrated by Hermanns et al. [48] for the fastest flame with an oxygen content of $\mathcal{R}_{O_2} = 7.7\%$ and equivalence ratio of 1.7. For this flame the calculated laminar burning velocity is 38.75 cm/s. By introducing the assumption that all H atoms reaching the surface of the burner plate are removed from the system, the concentration of H should be reduced by less than about 30%. This value is estimated from the porosity of the perforated plate (figure 3.4b) and by allowing a partial sink of H

atoms inside holes of the perforated plate. In this case, 30% reduction of H-atoms, the calculated burning velocity is 38.72 cm/s. Even at the limiting case of a reduction of H atoms by 60%, the calculated burning velocity is 38.67 cm/s. These tiny changes are well below the experimental uncertainties discussed in the previous sections.

Another point of interest is whether the burner plate could act in reactions as a kind of third body, e.g. reaction 5 in table A.1. This is investigated by adding an additional third body coefficient for the nitrogen species in equation (A.2). The collision efficiency for this species is set to 100. The adjusted equation for the reaction rate of third body reactions is given by

$$r_j = \left(100 n_{N_2} + \sum_{i=1}^{N_s} \varsigma_{ij} n_i \right) \left(k_{j,f} \prod_{i=1}^{N_s} n_i^{\nu'_{ij}} - k_{j,b} \prod_{i=1}^{N_s} n_i^{\nu''_{ij}} \right), \quad (4.3)$$

In figure 4.17b the laminar burning velocity for stoichiometric methane-air flames as a function of the plate temperature T_p is shown using the mechanisms of Smooke [98], GRI-mech 3.0 [97] and Konnov [61] for hydrogen-oxygen-nitrogen flames ($R_{O_2} = 7.7\%$). The laminar burning velocity is hardly influenced by this effect until a temperature of ≈ 500 K. Above this plate temperature the hydrogen-air burning velocity drops significantly, whereas the laminar burning velocity increases for methane-air above a plate temperatures of ≈ 500 K. This indicates that it is unlikely that the burner plate, acting as a kind of third body, affects the laminar burning velocity measurements presented in this chapter.

4.5 Conclusions

The heat flux method has been successfully applied to hydrogen-oxygen-nitrogen mixtures and methane-hydrogen-air mixtures for various equivalence ratios. The initial temperature of these flames is 298 K, except for the methane-hydrogen-air flames where also measurements up to 433 K have been performed for equivalence ratios of $\phi = 0.8, 1.0$ and 1.2. The typical uncertainty (95% confidence interval) for the present measurements in the burning velocity is ≈ 0.5 cm/s.

Comparison with literature shows that the present methane-hydrogen-air data is consistent with recent laminar burning velocity results determined by other measurement techniques such as the counterflow method and the spherical bomb method, provided that proper corrections are made in those experiments to account for any non-linear stretch effects. The majority of the experimental data found in literature did not correct for these non-linear effects and show significantly higher laminar burning velocities compared to the present heat flux data. The recent published data presented by Halter et al. [42] are comparable with the present heat flux data.

The laminar burning velocities of methane-air for increased unburnt gas temperature presented in this thesis are comparable with recent measurements of Bosschaart et al. [7]. The experimental data of other authors is considerably scattered. The experimental data presented by Gu et al. [39] tend to predict somewhat similar increase in burning velocity as a function of the unburnt gas temperature. In the case of laminar burning velocities of methane-hydrogen-air mixtures for increased temperature of unburnt gas mixtures

new accurate data, with confidence intervals, as measured with the heat flux method are presented.

For hydrogen-oxygen-nitrogen flames a significant difference was found when comparing the present results with experimental data from literature. Part of this difference in burning velocity can be attributed to errors arising from the linear extrapolation to zero stretch employed by Egolfopoulos and Law. [26]. Due to large amount of nitrogen added in the hydrogen-oxygen-nitrogen mixture not only the laminar burning velocity decreases compared to hydrogen-air but also the flame temperature. The burning velocities for hydrogen-oxygen-nitrogen mixtures presented in this thesis can provide an extended basis for the validation of kinetic models towards lower flame temperatures.

For methane-hydrogen-air flames with equivalence ratios larger than 1.4 it was found that the flames stabilised on the heat flux burner do not behave as 1D flames anymore. The laminar burning velocity measured for these flames overpredict the laminar burning velocity slightly. This behaviour is not observed for the investigated fuel rich hydrogen-oxygen-nitrogen flames. An indication of the flatness is given by the temperature distribution in the burner plate which showed no anomalies that could arise in the case of cellular flames. Additionally, experiments with diluted flames of hydrogen-carbon monoxide-carbon dioxide-air by Konnov et al. [62] which were stabilised on a similar burner and were visible, no cellularity has been observed. Also recent studies of hydrocarbon-oxygen-inert flames stabilised using the heat flux method [63] showed that cellularity does not appear in mixtures with nitrogen as inert diluent.

The influence of the burner plate acting as a catalyst is also analysed numerically as well as experimentally. A negligible effect is found for the present measurement range. The change in burning velocity due to burner surface reactions is expected to be smaller than the present measurement uncertainty. However when increasing the unburnt gas temperature to temperatures relevant for gas turbine conditions, $T_u \approx 600$ K, the burner plate could have some influence on the measured laminar burning velocities.

In the development of detailed, comprehensive chemical mechanisms for the modelling of combustion phenomena, model validation through comparison with reliable experimental data is important. In the next chapter the performance of existing combustion reaction mechanisms in determining the laminar burning velocity is compared with the present heat flux data.

Numerical Results

The laminar burning velocities measured using the heat flux burner and presented in the previous chapter are compared in this chapter with numerical calculations. To that end several combustion reaction mechanisms have been used. The first part of this chapter deals with hydrogen-oxygen-nitrogen flames at ambient conditions. The heat flux measurements are compared with hydrogen based as well as methane based reaction mechanisms. In the second part of this chapter the measured laminar burning velocities of methane-hydrogen-air flames at ambient conditions are compared with several numerical mechanisms. In the last part of this chapter a comparison between experimental heat flux data and numerical data is performed for methane-hydrogen-air flames at increased unburnt temperature.

5.1 Introduction

In the previous chapter measurements of the laminar burning velocity for several mixtures are presented. This accurate set of laminar burning velocity data determined with the heat flux method will be used in this chapter to validate existing combustion reaction mechanisms. The selected combustion reaction mechanisms mentioned in chapter 2 will be used for this purpose. The heat flux data of the hydrogen-oxygen-nitrogen flames in the next section will be compared using hydrogen based mechanisms as well as methane based mechanisms. Methane based mechanisms are used in the sections describing the comparison between experiments and numerical results of methane-hydrogen-air flames for ambient conditions and as well as for increased unburnt gas temperatures. The heat flux data presented in the previous chapter give relative small error estimates. In the figures shown in this chapter the error estimate is not shown when the error estimate is small and difficult to distinguish from the presented data. For completeness the experimental data with error estimates is listed in appendix E.

A decent analysis regarding kinetic schemes should include for example a comparison of ignition delay times, species profiles, sensitivity analysis, reaction path analysis and the applied reaction rates. However, the focus of this thesis is related to laminar burning velocities of hydrogen enriched methane-air mixtures, as a result only burning velocities will be used to describe the performance of the kinetic schemes.

5.2 Hydrogen-Oxygen-Nitrogen Flames

This section describes the laminar burning velocities of the relevant hydrogen-oxygen-nitrogen flames. These flames are interesting from a reaction modelling point of view. This is because in recent studies [19, 47, 56, 88] it has turned out that the frequent extensions and adaptations of the most important existing kinetic schemes of complex fuels has resulted in a decreased accuracy of the sub-mechanism describing the oxidation chemistry in the hydrogen-oxygen-nitrogen sub-system. This has introduced a renewed interest in this sub-mechanism by the reaction mechanism builders [61], resulting in several new hydrogen based combustion reaction mechanisms in recent years [61, 68, 78].

Both hydrogen based mechanisms (table 2.1) and methane based mechanisms (table 2.2) will be used for comparison. However, the methane based mechanism of Konnov [60] is not used for comparison in this section because a more recent hydrogen based mechanism is available [61]. The pressure ($p_u = 1$ atm) and unburnt gas temperature ($T_u = 298$ K) is equal for both experiments and numerical data. The measurement range which is used for comparison in this section is shown in the previous chapter in figure 4.3.

Varying oxygen content at $\phi = 1.06$

In figure 5.1 the laminar burning velocities determined with the heat flux burner are shown together with the corresponding error estimate. The presented results in this figure are taken at constant equivalence ratio; $\phi = 1.06$ but with varying oxygen content. The heat flux measurements are compared with several numerical combustion reaction mechanisms. In figure 5.1a the results of several hydrogen-air based mechanisms are shown and in figure 5.1b of the methane-air based mechanisms are shown.

The hydrogen based mechanisms in figure 5.1a generally underpredict the laminar burning velocity compared to the experimental data determined with the heat flux method. The hydrogen mechanism of Konnov [61] is the closest one to the experimental data. The difference for low oxygen contents for this mechanism is approximately 1 cm/s and increasing to approximately 10 cm/s for $R_{O_2} = 10\%$. The difference between the heat flux data and the two other hydrogen based mechanisms, of Ó Conaire et al. [78] and Li et al. [68], is even larger. Note that the increase in burning velocity as a function of the oxygen content for the heat flux method is larger than the increase in the numerically determined data.

In the case of methane based mechanisms the comparison between numerical data and the experimental results is shown in figure 5.1b. Generally the methane based combustion

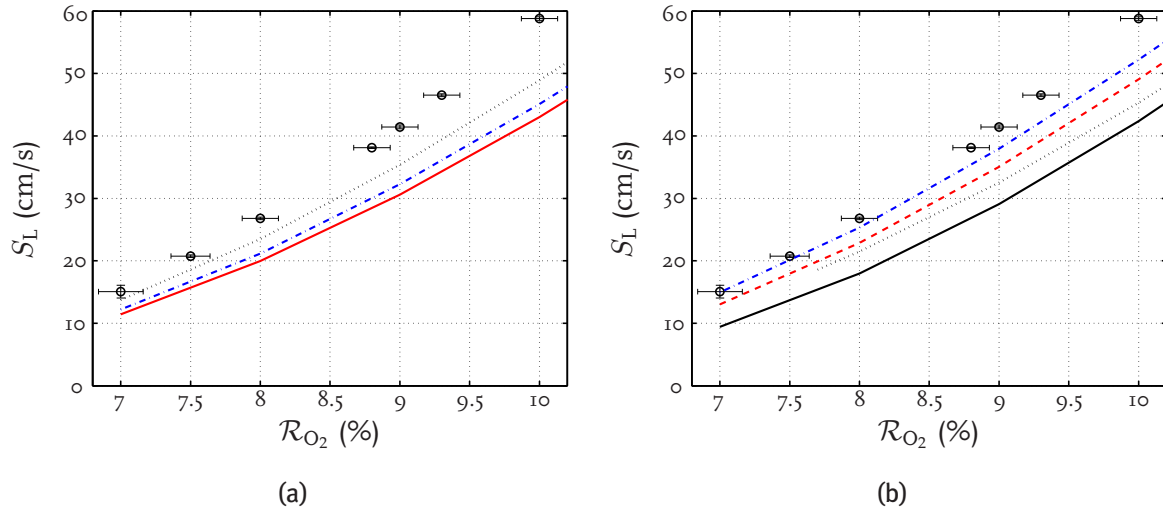


Figure 5.1: Experimental and numerical data of the laminar burning velocities of hydrogen-oxygen-nitrogen flames as a function of the oxygen content at constant equivalence ratio $\phi = 1.06$. The heat flux measurements are denoted with a circle and error estimate. Left figure: Hydrogen based mechanisms, Konnov [61], dotted line; Li et al. [68], dashed dotted line and O'Conaire et al. [78], solid line. Right figure: Methane based mechanisms, Leeds [53], dotted line with square symbols; GDF-kin [27], dashed line; SKGo3 [96], dashed dotted line and GRI-mechanism [97], solid line.

mechanisms underpredict the laminar burning velocity. However, the difference between experiments and the SKGo3 mechanism [96] for oxygen contents lower than 9% is negligibly small, less than 1 cm/s. Note that the numerical results for the lower oxygen contents with the SKGo3 mechanism are inside the heat flux error estimates. For higher oxygen contents the difference increases up to ≈ 7 cm/s. The GDF-kin mechanism [27], the Leeds mechanism [53] and the GRI-mechanism [97] give lower results at $R_{O_2} = 10\%$; 10, 14 and 17 cm/s respectively. The numerical results of these mechanisms are clearly outside the error estimate of the heat flux burner for the measured range. For oxygen contents at $R_{O_2} = 7\%$ the difference is smaller than ≈ 5 cm/s. Similarly as for the hydrogen based mechanisms the increase in burning velocity as a function of the oxygen content increases slower compared to the heat flux data. It is interesting to note that the laminar burning velocities calculated with the methane based SKGo3 mechanism compared to the heat flux data give smaller differences than the hydrogen based mechanisms.

Varying equivalence ratio at $R_{O_2} = 7.7\%$

The laminar burning velocities as a function of the equivalence ratio of hydrogen-oxygen-nitrogen flames are shown in figure 5.2. The hydrogen dilution of these mixtures is $R_{O_2} = 7.7\%$. Again in the left figure the heat flux results are compared with results of hydrogen based mechanisms whereas in the right figure a comparison with the methane based mechanisms is presented.

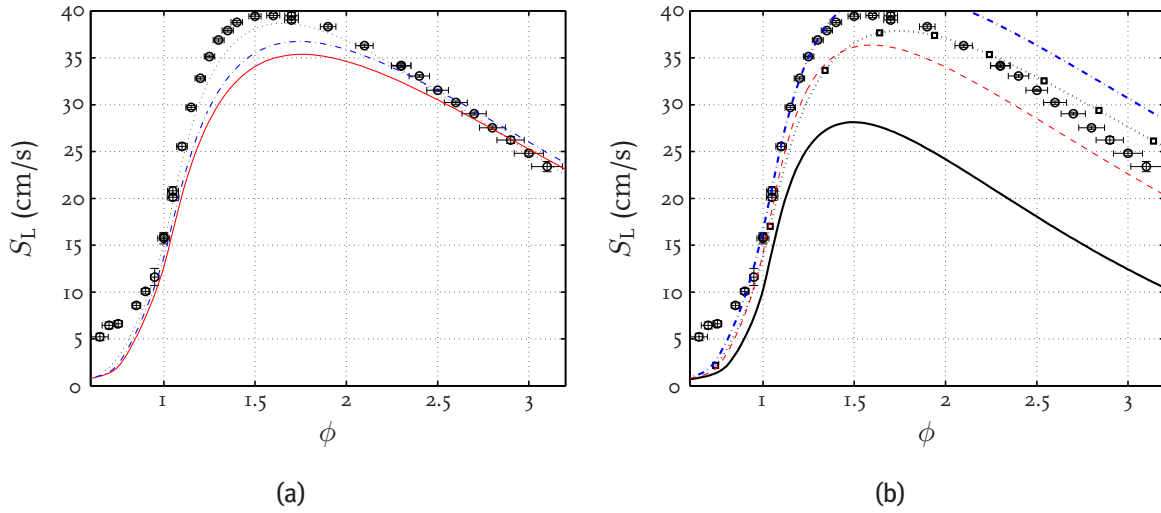


Figure 5.2: Experimental and numerical data of the laminar burning velocities of hydrogen-oxygen-nitrogen flames as a function of the equivalence ratio at constant oxygen content $R_{O_2} = 7.7\%$. The heat flux measurements are denoted with a circle and error estimate. Left figure: Hydrogen based mechanisms, Konnov [61], dotted line; Li et al. [68], dashed dotted line and Ó Conaire et al. [78], solid line. Right figure: Methane based mechanisms, Leeds [53], dotted line with square symbols; GDF-kin [27], dashed line; SKGo3 [96], dashed dotted line and GRI-mechanism [97], solid line.

Four regions can be distinguished in figure 5.2a when comparing the hydrogen based mechanisms with the heat flux results; two regions with relatively large differences and two regions with relatively small differences. The first region with large differences occurs at equivalence ratios lower than $\phi \approx 0.9$, in this region the velocities are low and the difference between the kinetic schemes and heat flux results is ≈ 4 cm/s. In the second region the difference between experiments and numerical data is relative small, less than 2 cm/s which is just outside the error estimate of the heat flux data in this region. This region starts at an equivalence ratio of $\phi \approx 0.9$ and ends at an equivalence ratio of $\phi \approx 1.05$. Note that due to the sharp increase of the laminar burning velocity a small change in equivalence ratio gives already a significant increase in burning velocity. The third region is located between equivalence ratios of $\phi \approx 1.05$ and $\phi \approx 2.3$. In this region the laminar burning velocity is underpredicted by the hydrogen based reaction mechanisms compared to the heat flux data and outside the error estimates. The maximum difference is located approximately where the maximum burning velocity is located; $\phi \approx 1.5$. Note that position of the maximum burning velocity is slightly different. Looking at the different reaction mechanisms individually, it is concluded that in this region the Konnov mechanism [61] is performing quite well. Also the location of the largest burning velocity is predicted fairly well. The difference between heat flux data and this mechanism is ≈ 3 cm/s. The mechanisms of Li et al. [68] and Ó Conaire et al. [78] show in this region differences up to ≈ 6 cm/s. In the fourth and last region the differences between the mechanisms and the heat flux data become smaller again; less than ≈ 2 cm/s ($\phi > 2.3$).

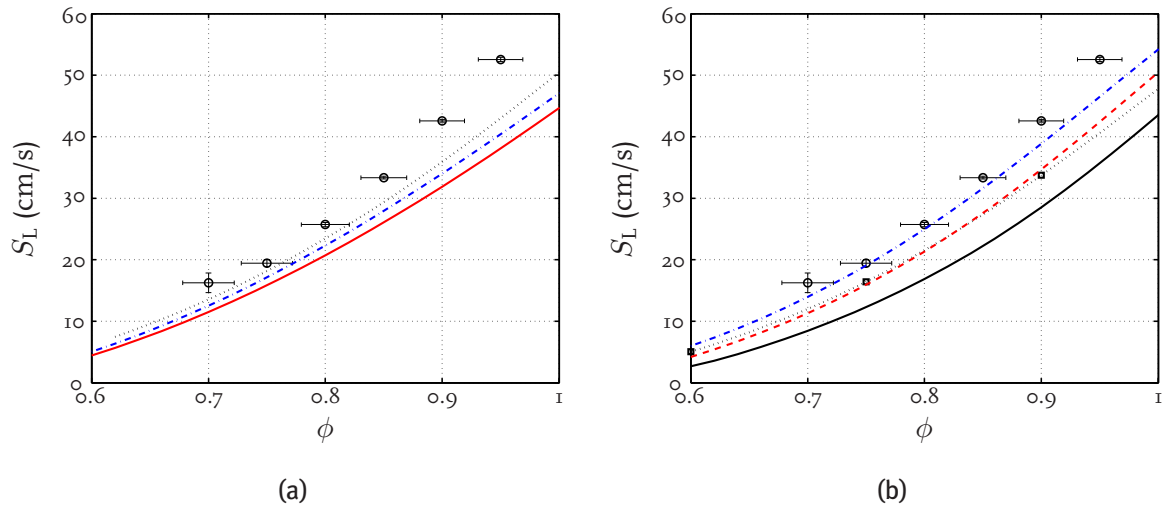


Figure 5.3: Experimental and numerical data of the laminar burning velocities of hydrogen-oxygen-nitrogen flames as a function of the equivalence ratio at constant oxygen content $\mathcal{R}_{\text{O}_2} = 10.7\%$. The heat flux measurements are denoted with a circle and error estimate. Left figure: Hydrogen based mechanisms, Konnov [61], dotted line; Li et al. [68], dashed dotted line and Ó Conaire et al. [78], solid line. Right figure: Methane based mechanisms, Leeds [53], dotted line with square symbols; GDF-kin [27], dashed line; SKGo3 [96], dashed dotted line and GRI-mechanism [97], solid line.

The comparison between experiments and methane based mechanisms in figure 5.2b shows significant differences for these combustion reaction mechanisms. The laminar burning velocities of the GRI-mechanism [97] are for fuel rich flames up to 13 cm/s lower compared to the heat flux data. For fuel lean flames the difference is smaller, less than 5 cm/s. For fuel rich flames ($\phi > 2$) the Leeds mechanism [53] overpredicts the laminar burning velocity whereas the GDF-kin mechanism [27] underpredicts the laminar burning velocity. The differences compared the heat flux data are less than 4 cm/s, but still outside the error margin of the heat flux burner. For mixtures with equivalence ratios between 1.2 and 2 the Leeds mechanism and the GDF-kin mechanism both underpredict the laminar burning velocity compared to the heat flux data; the difference in this region is less than 3 cm/s. In the region where the largest laminar burning velocity increase is located, around $\phi = 1$, the difference between measurements and mechanisms is relative small, less than 3 cm/s. The SKGo3 mechanism [96] performs in this area very well; for equivalence ratios between 0.8 and 1.4 the numerical results are even within the error estimate of the heat flux data. The difference in burning velocity between the heat flux data and the SKGo3 results increases for fuel rich flames. Here the difference between experimental data and SKGo3 data (≈ 5 cm/s) is even larger than the Leeds mechanism and the GDF-kin mechanism. For fuel lean mixtures all the mechanisms generally underpredict the laminar burning velocity up to 5 cm/s ($\phi < 0.9$).

Varying equivalence ratio at $\mathcal{R}_{O_2} = 10.7\%$

Laminar burning velocities determined with the heat flux method of hydrogen-oxygen-nitrogen flames with $\mathcal{R}_{O_2} = 10.7\%$ are shown in figure 5.3. The left figure shows the comparison with hydrogen based kinetic schemes and the right figure shows the methane based mechanisms. Generally the numerical determined burning velocities show lower values compared to the corresponding heat flux data. The laminar burning velocity of the experimental data increases faster as a function of equivalence ratio when comparing them to the numerical results.

The difference between experiments and numerical data for the hydrogen based mechanisms in figure 5.3a is for an equivalence ratio of 0.7 less than 4 cm/s. For equivalence ratios close to stoichiometry the difference increases and can be as large as 14 cm/s. However, for equivalence ratio smaller than $\phi = 0.8$ the results of the Konnov mechanism [61] are close to heat flux data and almost everywhere inside the error estimate. For larger equivalence ratios the difference increases. The mechanisms of Li et al. [68] and Ó Conaire et al. [78] show even lower results and are for the whole measured range outside the error estimate of the heat flux results.

The difference in burning velocities between the methane based mechanisms shown in figure 5.3b is larger compared to the hydrogen based mechanisms. It is interesting to note is that the SKGo3 mechanism [96] is located for almost the whole measured range inside the experimental error estimate of the heat flux method. Only the highest equivalence ratios show some lower burning velocities. The difference between the experimental results and the Leeds mechanism [53] and the GDF-kin mechanism [27] is on the lean side ≈ 4 cm/s and the maximum difference (≈ 12 cm/s) occurs at an equivalence ratio of $\phi = 0.95$ which is for the measured range outside the experimental uncertainty. The GRI-mechanism shows even lower results.

5.2.1 Discussion

The Konnov mechanism [61] is performing relative well to reproduce the experimental heat flux data. However, the difference in burning velocity can still be up to ≈ 10 cm/s for highly diluted nitrogen mixtures of $\mathcal{R}_{O_2} = 7.7\%$. For slightly less diluted nitrogen mixtures of $\mathcal{R}_{O_2} = 10.7\%$ the differences between experiments and the Konnov mechanism is smaller, ≈ 2 cm/s. The other hydrogen based mechanisms show slightly larger differences compared to the heat flux data. Generally the discrepancy in burning velocity between the hydrogen based combustion reaction mechanism is less than 3 cm/s. Only for mixtures consisting of an oxygen content of $\mathcal{R}_{O_2} = 7.7\%$ the discrepancy is slightly larger for equivalence ratios of $\phi \approx 1.5$.

The methane based mechanisms show large differences in burning velocity. Especially the discrepancy for the highly diluted nitrogen flames of $\mathcal{R}_{O_2} = 7.7\%$ is large, e.g. the GRI-mechanism [97] gives significantly lower burning velocities compared to the other mechanisms. Generally the SKGo3 mechanism [96] performs very well compared to the heat flux data. However the burning velocity is overestimated for rich flames consisting of an oxygen content of $\mathcal{R}_{O_2} = 7.7\%$ (≈ 5 cm/s).

It is interesting to note that the methane based SKGo3 mechanism [96] is performing

very well compared to the hydrogen based mechanisms. For example the burning velocity results of the SKGo3 mechanism compared to the heat flux data for mixtures with an oxygen content of $\mathcal{R}_{\text{O}_2} = 7.7\%$ and also for 10.7% is even slightly better than the results of the hydrogen based mechanisms. Especially for equivalence ratios close to stoichiometric mixtures. For all results it can be concluded that for $\phi < 1.4$ SKGo3 is the best scheme; for the entire measured range the Konnov mechanism performs best.

5.3 Methane-Hydrogen-Air Flames

In this section the laminar burning velocities of methane-hydrogen-air flames measured with the heat flux burner are compared with numerical results. The numerical results are calculated with CHEM1D using the selected methane combustion reaction mechanisms mentioned in chapter 2; GDF-kin[®] [27], GRI-mechanism version 3.0 [97], Leeds methane mechanism version 1.5 [53], SKGo3 [96] and the mechanism of Konnov version 0.5 [60]. The pressure ($p_u = 1$ atm) and unburnt gas temperature ($T_u = 298$ K) is equal for both experiments and numerical data. The measured hydrogen contents are $\mathcal{R}_{\text{H}_2} = 0, 10, 20, 30$ and 40% . In this section only $\mathcal{R}_{\text{H}_2} = 0, 20$ and 40% are discussed, because the comparison for the other hydrogen contents give similar results.

Methane-air flames

In figure 5.4 the laminar burning velocities of methane-air flames are shown as a function of equivalence ratio. The heat flux data are plotted with the error estimates. It is interesting to note that for stoichiometric methane-air flames the difference in laminar burning velocity between the heat flux data and the kinetic schemes is negligible. The difference in burning velocity is significant between the measurements and the results of the Leeds combustion mechanism [53]. On the fuel lean side this can be up to 6 cm/s and on the fuel rich side this is even larger, ≈ 10 cm/s. Generally the difference in figure 5.4 is less than ≈ 2 cm/s for the measured equivalence ratio range. Comparing the GRI-mechanism [97] and the SKGo3 mechanism [96] to the heat flux results gives comparable results. The numerical data are only for equivalence ratios smaller than 0.75 and larger than 1.40 outside the error estimate of experimental data. The Konnov mechanism [60] systematically underpredicts the laminar burning velocity compared to the measurements. The difference is small for lean mixtures and rich mixtures, but the discrepancy is notable for stoichiometric mixtures, see also Coppens et al. [17]. The mechanism GDF-kin [27] shows comparable results with the heat flux measurement for lean to slightly rich flames ($\phi = 1.05$). On the rich side the mechanism overpredicts the laminar burning velocity by ≈ 3 cm/s.

Methane-hydrogen-air flames at $\mathcal{R}_{\text{H}_2} = 20\%$

Laminar burning velocity results with the heat flux burner and simulations with CHEM1D of methane-hydrogen-air mixtures with a hydrogen content of $\mathcal{R}_{\text{H}_2} = 20\%$ in the fuel are shown in figure 5.5. Similar as for methane-air flames, the numerically

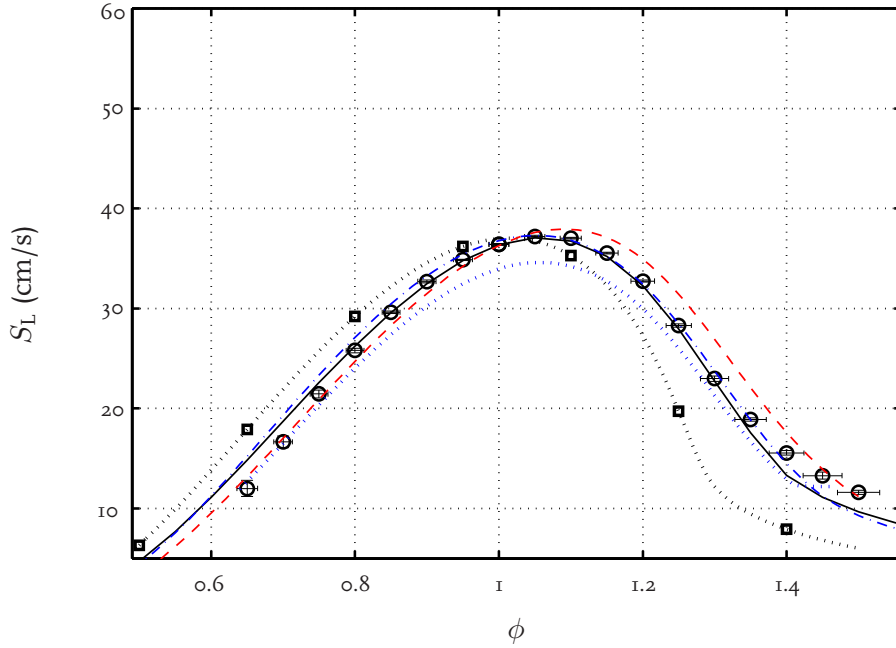


Figure 5.4: Experimental and numerical data of the laminar burning velocities of methane-air flames as a function of the equivalence ratio. The heat flux measurements are denoted with a circle and error estimate. The numerical results using the mechanisms of Leeds [53], dotted line with square symbols; Konnov [60], dotted line; GDF-kin [27], dashed line; SKGo3 [96], dashed dotted line and GRI-mechanism [97], solid line.

determined laminar burning velocities for this hydrogen content are for a stoichiometric flame very close to the experimental data. Only the mechanism of Konnov [60] underpredicts the laminar burning velocity for stoichiometric flames by approximately 2 cm/s. The results of the Leeds mechanism deviates from the experimental results and the other mechanisms significantly for fuel lean and fuel rich mixtures. This behaviour is also found for pure methane flames. The laminar burning velocity results of the other mechanisms are for the measured range of equivalence ratios almost everywhere inside the error estimate of the heat flux data. Only between an equivalence ratios of $\phi \approx 1.05$ and $\phi \approx 1.15$ the numerical data are just outside the error estimates. However, a small difference in equivalence ratio between the mechanisms is still visible; for example the GDF-kin mechanism [27] is approximately 0.03 shifted in equivalence ratio compared to the heat flux data, GRI-mechanism [97] and the SKGo3 mechanism [96].

Methane-hydrogen-air flames at $\mathcal{R}_{H_2} = 40\%$

The laminar burning velocity results as a function of equivalence ratio for a hydrogen content of $\mathcal{R}_{H_2} = 40\%$ are shown in figure 5.6. Here the Leeds mechanisms is performing significantly better on the lean side compared to the methane-air results (see figure 5.4) and the methane-hydrogen-air flames with a hydrogen content of $\mathcal{R}_{H_2} = 20\%$. For $\mathcal{R}_{H_2} = 40\%$ the difference to the heat flux measurements is approximately 1 cm/s. On the fuel rich side the difference increases again to even more than 10 cm/s. The shift

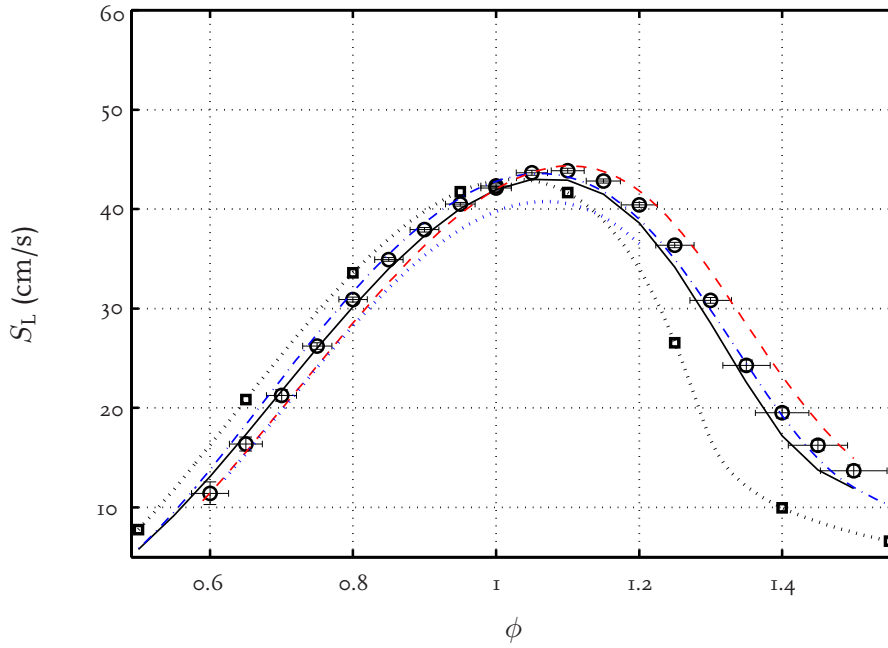


Figure 5.5: Experimental and numerical data of the laminar burning velocities of methane-hydrogen-air flames as a function of the equivalence ratio at $\mathcal{R}_{\text{H}_2} = 20\%$. The heat flux measurements are denoted with a circle and error estimate. The numerical results using the mechanisms of Leeds [53], dotted line with square symbols; Konnov [60], dotted line; GDF-kin [27], dashed line; SKGo3 [96], dashed dotted line and GRI-mechanism [97], solid line.

in equivalence ratio for the GDF-kin mechanism [27] which was mentioned already for $\mathcal{R}_{\text{H}_2} = 20\%$ increases even more. Contrary to the previous hydrogen contents the GRI-mechanism [97] now underpredicts the laminar burning velocity compared to the heat flux data, this difference is ≈ 3 cm/s. Also on the fuel lean side the GRI-mechanism underpredicts the present heat flux results. On the fuel rich side the laminar burning velocity calculated with the GRI-mechanism is comparable with the measured heat flux data. The difference between the SKGo3 mechanism [96] and heat flux measurements is for $\mathcal{R}_{\text{H}_2} = 40\%$ very small. The numerical results of this mechanism are within the error estimate of heat flux data for the measured range of equivalence ratios.

Stoichiometric methane-hydrogen-air flames

In figure 5.7 the laminar burning velocity of stoichiometric methane-hydrogen-air flames as a function of the hydrogen content is compared with the numerically determined burning velocities. The difference in burning velocity for hydrogen contents up to $\mathcal{R}_{\text{H}_2} = 20\%$ between the measurements and the mechanisms is not large; less than 1 cm/s. Except for the Konnov [60] mechanism which gives systematically ≈ 2 cm/s lower burning velocities. For higher hydrogen contents the difference increases slightly to ≈ 4 cm/s for the Konnov mechanism and 2 cm/s for the other mechanisms.

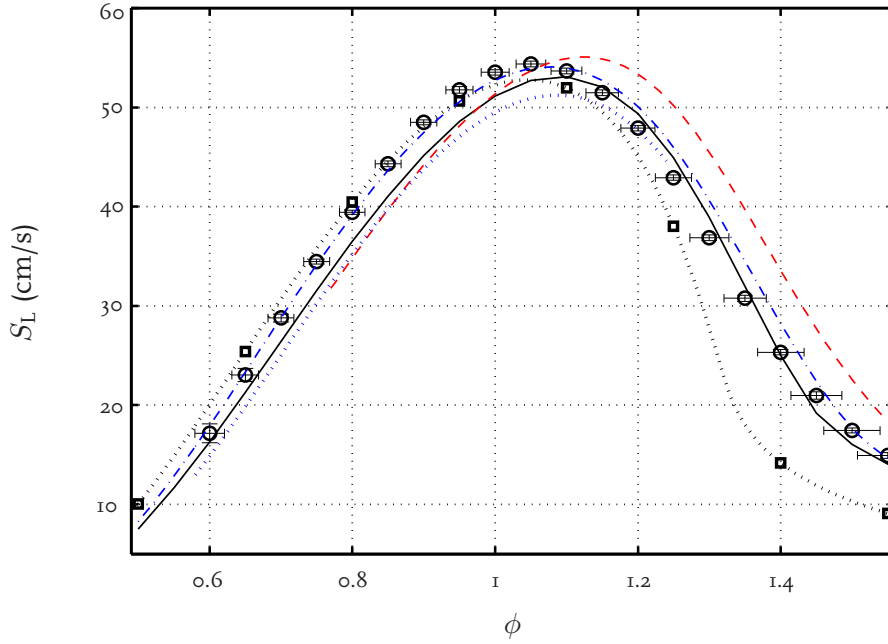


Figure 5.6: Experimental and numerical data of the laminar burning velocities of methane-hydrogen-air flames as a function of the equivalence ratio at $\mathcal{R}_{\text{H}_2} = 40\%$. The heat flux measurements are denoted with a circle and error estimate. The numerical results using the mechanisms of Leeds [53], dotted line with square symbols; Konnov [60], dotted line; GDF-kin [27], dashed line; SKGo3 [96], dashed dotted line and GRI-mechanism [97], solid line.

5.3.1 Discussion

The methane based mechanisms used in this section for comparison of the laminar burning velocity with the experimentally determined heat flux data show significant differences. For example for fuel rich mixtures the Leeds mechanism [53] significantly underpredicts the laminar burning velocity compared to the heat flux data, whereas for fuel lean mixtures this mechanism overpredicts laminar burning velocity slightly. The GDF-kin mechanism [27] slightly overpredicts the laminar burning for fuel rich flames. Note that this difference increases slightly with increasing hydrogen content. The Konnov mechanism [60] generally underpredicts the laminar burning velocity compared to the heat flux results. The largest difference occurs close to stoichiometric mixtures. The GRI-mechanism [97] and the SKGo3 mechanism [96] are close to the experimental data and even for a significant part of the measured range inside the error estimate of the heat flux method. However the GRI-mechanism underpredicts the laminar burning velocities for fuel lean mixtures at higher hydrogen contents, $\mathcal{R}_{\text{H}_2} = 40\%$. Here the GRI-mechanism is even outside the error estimate of the heat flux results.

Dominating mechanism

From the presented data in this section the mechanism behind the increase in burning velocity as a function of hydrogen content is still unclear. In this paragraph this increase

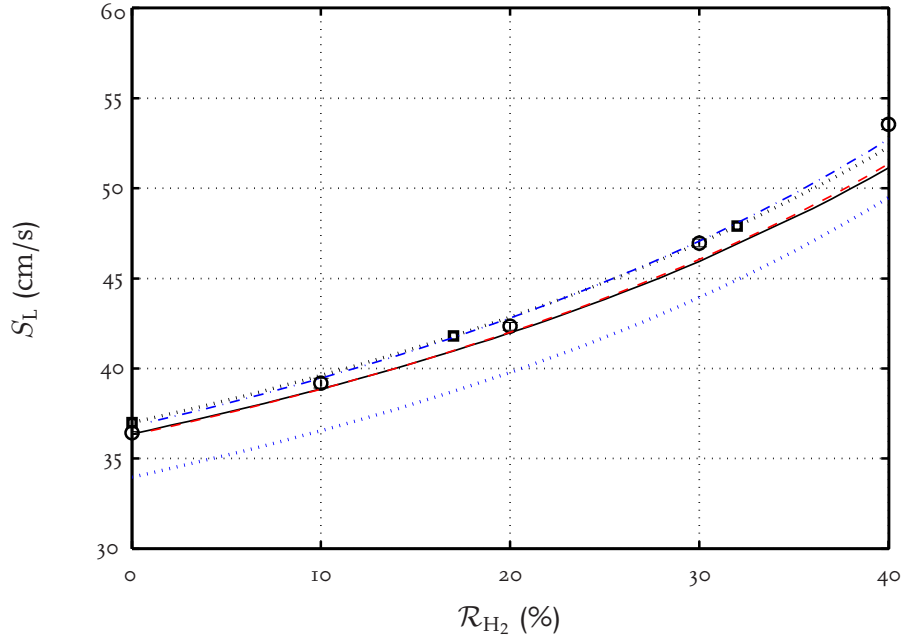


Figure 5.7: Experimental and numerical data of the laminar burning velocities of stoichiometric methane-hydrogen-air flames as a function of the hydrogen content. The heat flux measurements are denoted with a circle and error estimate. The numerical results using the mechanisms of Leeds [53], dotted line with square symbols; Konnov [60], dotted line; GDF-kin [27], dashed line; SKGo3 [96], dashed dotted line and GRI-mechanism [97], solid line.

in burning velocity will be investigated by analysing the change of the most important chemical reactions which take place in methane-hydrogen-air flames. Starting with a global view on the laminar burning velocity in figure 5.8 as a function of the hydrogen content. The data in this figure are determined using numerical calculations (GRI-mechanism) of stoichiometric methane-hydrogen-air flames. From this figure it is possible to identify three regimes [20]. The first regime (I) occurs at low hydrogen contents, $R_{H_2} < 50\%$. In this regime the laminar burning velocity increases slightly; this increase can be seen as a linear function of the hydrogen content. The second regime (II) for $50\% \leq R_{H_2} \leq 94\%$ a transition regime is found. Here the laminar burning velocity increases significantly and non-linearly. At higher hydrogen contents, $R_{H_2} > 94\%$, the third regime (III) is found. In this regime we have hydrogen flames with a minor amount of methane. Here the laminar burning velocity increases sharply and is again a linear function of the hydrogen content and therefore a linear function of methane. The two linear regimes have been widely recognised in literature [20].

In order to get insight in the reactions which play a major role in the observed regimes a sensitivity analysis is performed using the GRI-mechanism 3.0 [97]. In particular the influence of a certain reaction rate k_j on the mass flow is determined by using:

$$s_j = \frac{k_j}{\rho S_L} \frac{\partial \rho S_L}{\partial k_j}, \quad j \in [1, N_r]. \quad (5.1)$$

Here s_j is the relative sensitivity coefficient of the mass burning rate ρS_L when changing

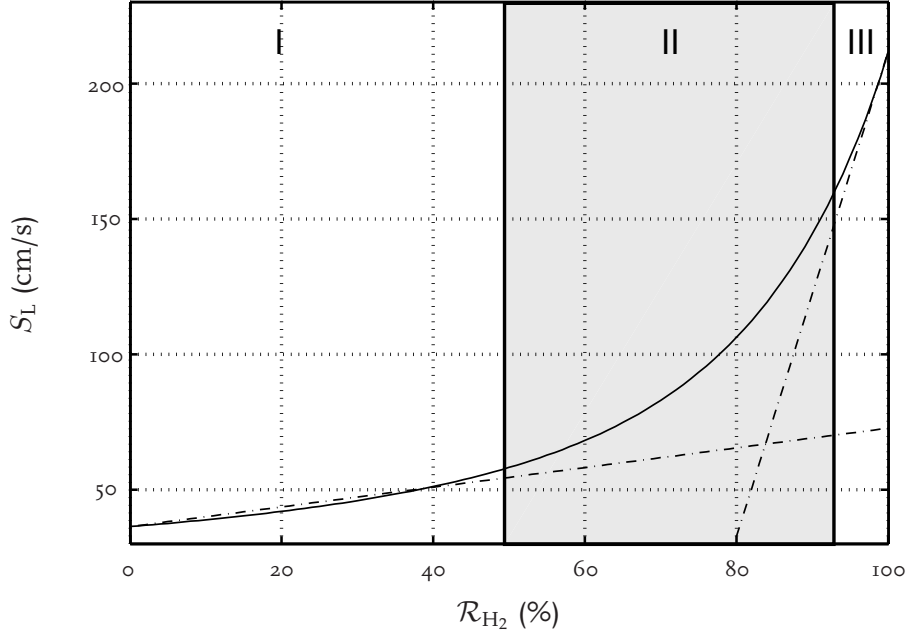


Figure 5.8: Laminar burning velocities of methane-hydrogen-air flames as a function of the hydrogen content. The solid line denotes the GRI-mechanism [97], the dashed-dotted lines are linear fits as a function of the hydrogen content.

reaction rate k_j . The elementary reaction steps with the largest sensitivity coefficients for stoichiometric methane-hydrogen-air flames in the GRI-mechanism [97] are listed below.



In figure 5.9 the corresponding sensitivity coefficients of the mentioned reactions are shown for several hydrogen contents; $\mathcal{R}_{\text{H}_2} = 0, 20, 40, 60, 80$ and 100%. In the first regime, $\mathcal{R}_{\text{H}_2} < 50\%$, the sensitivity coefficients for the presented reactions change slightly. However, in the second regime, $50\% \leq \mathcal{R}_{\text{H}_2} \leq 94\%$ the sensitivity coefficients start changing rapidly. Especially, reaction (5.2e), which drops significant. The corresponding sensitivity values of this reaction are still larger than the other major elementary reaction steps involved in the methane-hydrogen-air combustion. In this regime the importance of reaction (5.2h) gradually increases. In the third regime, $\mathcal{R}_{\text{H}_2} > 94\%$, the influence of reaction (5.2e) decreases sharp. The influence of the reactions (5.2a), (5.2b), (5.2c) and (5.2d) on the mass flow becomes negligible in this regime and in the end zero,

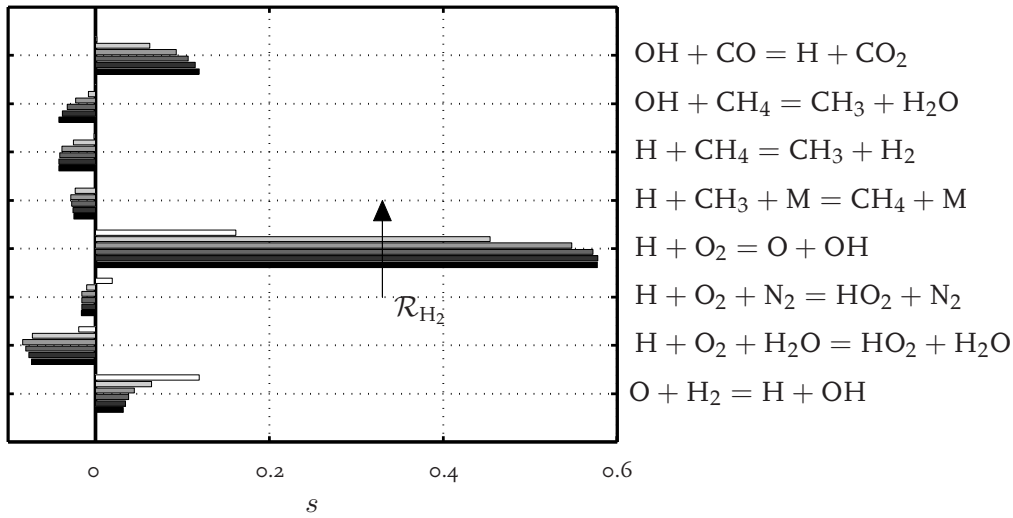


Figure 5.9: Sensitivity coefficients for stoichiometric methane-hydrogen-air flames using the GRI-mechanism [97]. The hydrogen contents are $\mathcal{R}_{\text{H}_2} = 0, 20, 40, 60, 80$ and 100% , indicated in gray colors from black to white respectively.

because no carbon containing species are available. for $\mathcal{R}_{\text{H}_2} = 100\%$. For stoichiometric hydrogen-air flames the most important reactions which determine the laminar burning velocity are (5.2e), (5.2f), (5.2g) and (5.2h).

Since reaction (5.2e) produces the largest relative sensitivity on the mass burning rate for stoichiometric methane-hydrogen-air flames it dominates the methane conversion. This process is well documented in literature, see e.g. [18, 87, 110]. When adding hydrogen the overall rate of combustion accelerates due to the increasing H radical concentration [20]. This indicates that there exists a strong coupling between the laminar burning velocity and the H radical concentration. This is recently shown by Di Sarli and Di Benedetto [20], who found that the laminar burning velocity increase as a function of the hydrogen content follows exactly the increase of the hydrogen radical in the mixture. In figure 5.10 this is shown using the GRI-mechanism [97]. According to Di Sarli and Di Benedetto [20] the fast reactions in the low temperature flame region require H radicals coming by diffusion from the flame front in the case of hydrogen-air flames. This kind of reactions enhance the propagation velocity of the hydrogen-air flames.

Correlation for the Burning Velocity

An expression describing the influence of the added hydrogen on the burning velocity can be useful as a design tool for analysing the behaviour of combustion equipment in the transition phase to a hydrogen economy. Gülder [40] proposed the following expression for methane-air flames with varying equivalence ratio

$$S_L = ZW\phi^\eta e^{\zeta(\phi-\sigma)^2}. \quad (5.3)$$

The values of the parameters are listed in table 5.1. Z is a parameter that is equal to 1 for pure fuels and, in the case the fuel is a mixture, depends on its composition. However,

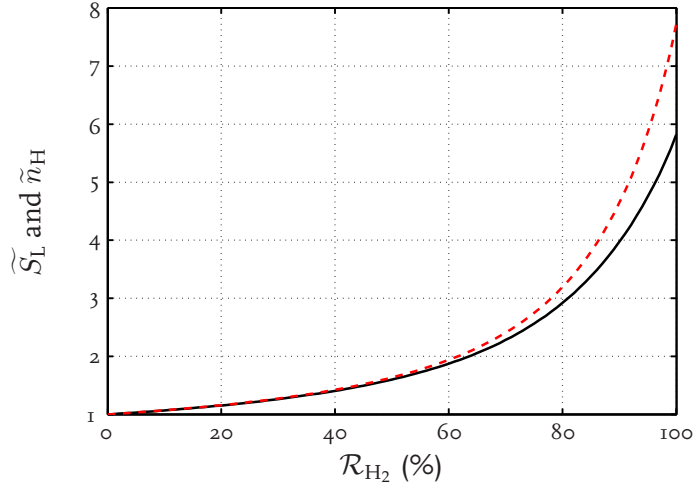


Figure 5.10: Normalised laminar burning velocities and the normalised maximum value of the hydrogen radicals as a function of the hydrogen content for stoichiometric methane-hydrogen-air flames using the GRI-mechanism [97]. Normalised laminar burning velocity, solid line and normalised maximum hydrogen radical concentration, dashed line.

Table 5.1: Fit parameters of equations (5.3) and (5.4).

	Glder [40]	Coppens [17]	Present Measurements
Z	1	-	-
γ	-	1.9153	1.7395
τ	-	1.533	1.3694
W (cm/s)	42.2	39.0542	38.9542
η	0.15	-0.4333	-0.7441
ζ	5.18	6.0157	6.2401
σ	1.075	1.1	1.1060
ω	-	0.0133	0.0126

Coppens et al. [17] noticed that this correlation does not agree with the actual, more precise, measurements of the laminar burning velocity of methane-air and methane-hydrogen-air mixtures. A new correlation is therefore proposed by Coppens et al. [17] which takes into account the hydrogen content in the fuel:

$$S_L = \left(1 + \gamma \mathcal{R}_{H_2}^\tau\right) W \phi^\eta e^{-\zeta(\phi - \sigma - \omega \mathcal{R}_{H_2})^2}. \quad (5.4)$$

In the exponent an additional term has been added by Coppens et al. to explore and simulate the shift of the maximum of the burning velocity dependence with the hydrogen concentration. The proposed correlation of Coppens et al. has also been fitted with the measurements of the present work. The parameters found when using a least square fitting procedure are listed in table 5.1. The values differ slightly from the values determined by Coppens et al. [17]. In figure 5.11, the present correlation is plotted together with the heat flux measurements. The correlation overestimates the flame speed observed

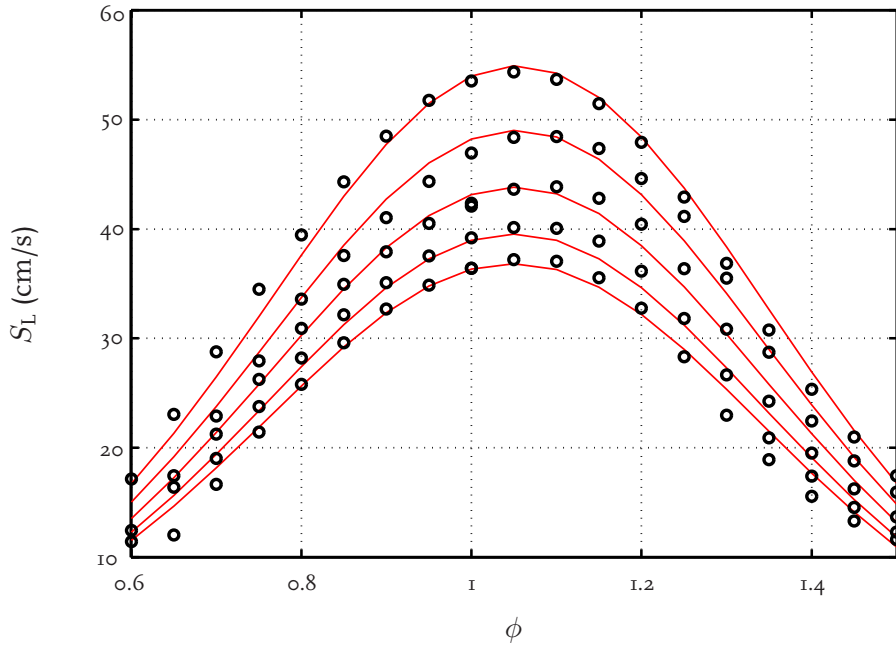


Figure 5.11: Laminar burning velocities of methane-hydrogen-air mixtures; $\mathcal{R}_{\text{H}_2} = 0, 10, 20, 30$ and 40% . The lines is the correlation of equation (5.4). The circles are heat flux measurements.

for lean mixtures and rich mixtures of fuels with relatively small hydrogen concentrations. For the highest hydrogen content $\mathcal{R}_{\text{H}_2} = 40\%$ the lean laminar burning velocity is slightly underpredicted. In general the maximum difference between the measurements and the experimental fit is less than 2.4 cm/s . Note that this value is comparable with the differences occurring between measurements and numerical combustion reaction mechanisms.

5.4 Methane-Hydrogen-Air Flames at Increased Unburnt Gas Temperatures

In this section the experimentally determined laminar burning velocities of methane-hydrogen-air flames with an increased unburnt gas temperature are compared with numerical data. The investigated equivalence ratios ($\phi = 0.8, 1.0$ and 1.2) and pressure ($p_u = 1 \text{ atm}$) are equal for both experiments and numerical data. The measured hydrogen contents are $\mathcal{R}_{\text{H}_2} = 0, 10, 20$ and 30% . In this section only the hydrogen contents $\mathcal{R}_{\text{H}_2} = 0$ and 20% are used for comparison. The other measured hydrogen contents behave similarly as the ones investigated in this section. Note that the error estimates for investigated flames are very small and not shown in the figures, because they are significantly smaller than the symbols used in the figures for indicating the heat flux measurements. However, the heat flux data with error estimates are listed in appendix E. The uncertainty in the unburnt gas temperature is taken as 1 K , see section 4.4.

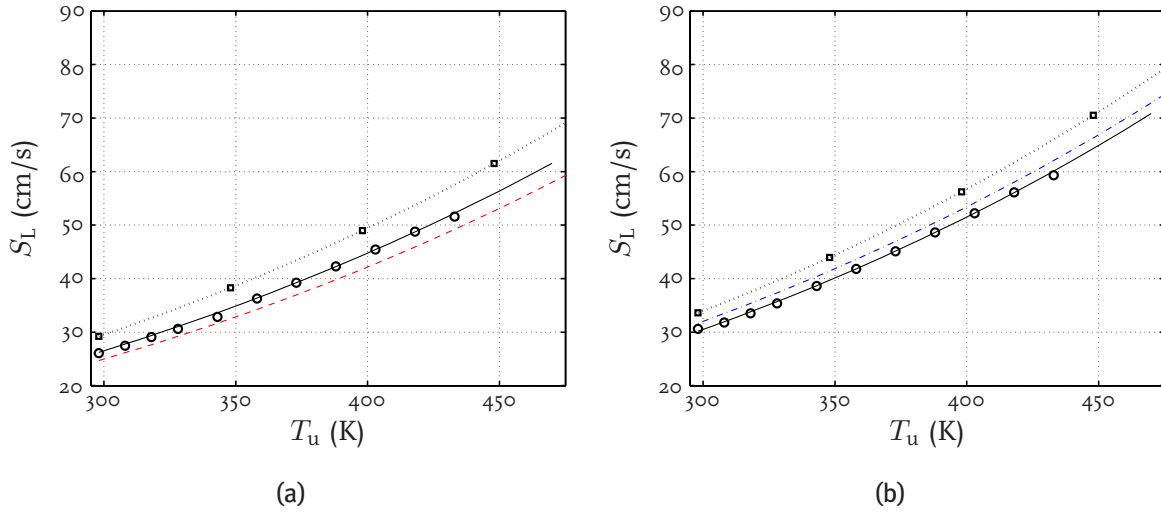


Figure 5.12: Experimentally and numerically determined laminar burning velocities of methane-hydrogen-air flames for an equivalence ratio of 0.8; $\mathcal{R}_{\text{H}_2} = 0\%$ (left) and $\mathcal{R}_{\text{H}_2} = 20\%$ (right). The heat flux data are denoted with circles, GRI-mechanism [97], solid line; Leeds mechanism [53], dotted line with square symbols; SKGo3 [96], dashed dotted line and the GDF-kin mechanism [27], dashed line.

Temperature dependence of fuel lean flames

The laminar burning velocities as a function of the unburnt gas temperature T_u are shown in figure 5.12 for mixtures with equivalence ratios of $\phi = 0.8$. The experimental heat flux data are compared with combustion reaction mechanisms for hydrogen contents of $\mathcal{R}_{\text{H}_2} = 0$ and $\mathcal{R}_{\text{H}_2} = 20$ in figures 5.12a and 5.12b respectively. The difference between the GRI-mechanism [97] and the heat flux data is very small and even close to or inside the error estimate of the heat flux data for both hydrogen contents. The Leeds mechanism [53] overpredicts the laminar burning velocity with typically 2 cm/s for both hydrogen contents. The SKGo3 mechanism [96] slightly overpredicts the laminar burning velocity, whereas GDF-kin mechanism [27] slightly underpredicts the laminar burning velocity. This behaviour of the combustion reaction mechanisms is consistent with the data presented in the previous section. The increase in burning velocity as a function of the unburnt gas temperature is slightly weaker for the mixtures with an hydrogen content of $\mathcal{R}_{\text{H}_2} = 0\%$ compared to the mixtures with $\mathcal{R}_{\text{H}_2} = 20\%$; being 0.20 and $0.23 \text{ cm s}^{-1} \text{ K}^{-1}$ respectively.

Temperature dependence of stoichiometric flames

In figure 5.13 numerically and experimentally determined laminar burning velocities as a function of the unburnt gas temperature are shown for stoichiometric mixtures. The difference between the measurements and numerical data is small. The individual mechanisms are difficult to distinguish and close to the experimental data. This small discrepancy for stoichiometric flames is also found for the measurements presented in

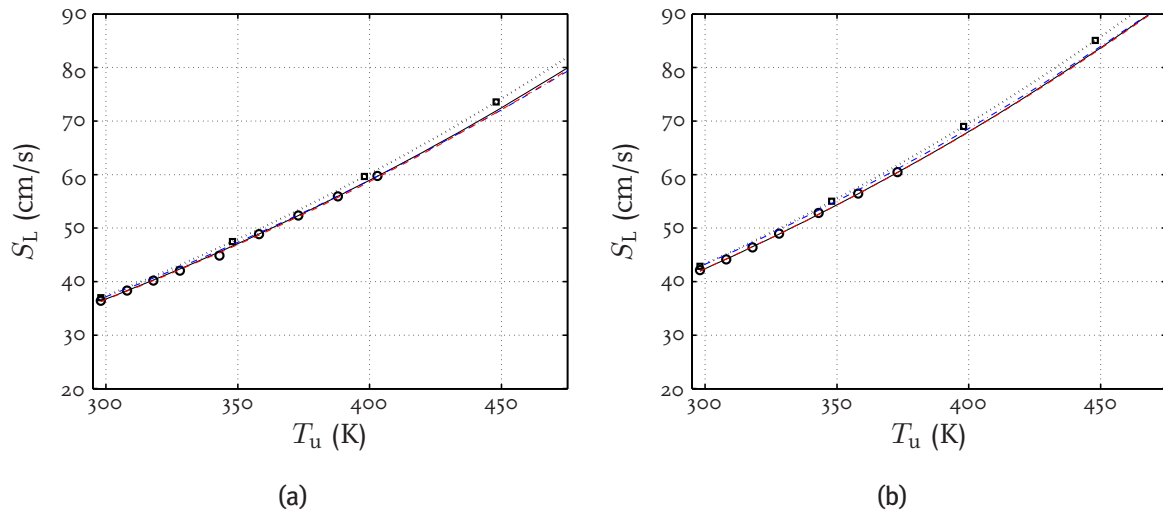


Figure 5.13: Experimentally and numerically determined laminar burning velocities of stoichiometric methane-hydrogen-air flames; $\mathcal{R}_{\text{H}_2} = 0\%$ (left) and $\mathcal{R}_{\text{H}_2} = 20\%$ (right). The heat flux data are denoted with circles, GRI-mechanism [97], solid line; Leeds mechanism [53], dotted line with square symbols; SKGo3 [96], dashed dotted line and the GDF-kin mechanism [27], dashed line.

the previous section. The increase in burning velocity as a function of the unburnt gas temperature for these stoichiometric flames is also slightly smaller for mixtures with an hydrogen content of $\mathcal{R}_{\text{H}_2} = 0\%$ compared to mixtures with $\mathcal{R}_{\text{H}_2} = 20\%$; being 0.25 and $0.28 \text{ cm s}^{-1} \text{ K}^{-1}$ respectively.

Temperature dependence of fuel rich flames

The temperature dependence of the laminar burning velocities of fuel rich methane-hydrogen-air mixtures ($\phi = 1.2$) is shown in figure 5.14. The results of the Leeds mechanism are for both hydrogen contents $\mathcal{R}_{\text{H}_2} = 0\%$ and $\mathcal{R}_{\text{H}_2} = 20\%$ lower than the experimental heat flux data, $\approx 4 \text{ cm/s}$. The difference between measurements and the other combustion reaction mechanisms is significantly smaller. The GDF-kin mechanism [27] slightly overpredicts ($\approx 1 \text{ cm/s}$) the laminar burning velocity. The difference between the GRI-mechanism [97] and the SKGo3 mechanism [96] is difficult to distinguish. These latter two mechanisms are just below the experimental data, although outside the error estimate of the heat flux results. For these mixtures the laminar burning velocity increases with 0.24 and $0.25 \text{ cm s}^{-1} \text{ K}^{-1}$ for $\mathcal{R}_{\text{H}_2} = 0\%$ and $\mathcal{R}_{\text{H}_2} = 20\%$ respectively.

5.4.1 Discussion

Generally the mechanisms predict the laminar burning velocity increase as a function of the unburnt gas temperature quite well. The typical difference between experiments and numerical data at $T_u = 298 \text{ K}$ occur also at higher unburnt gas temperatures. This

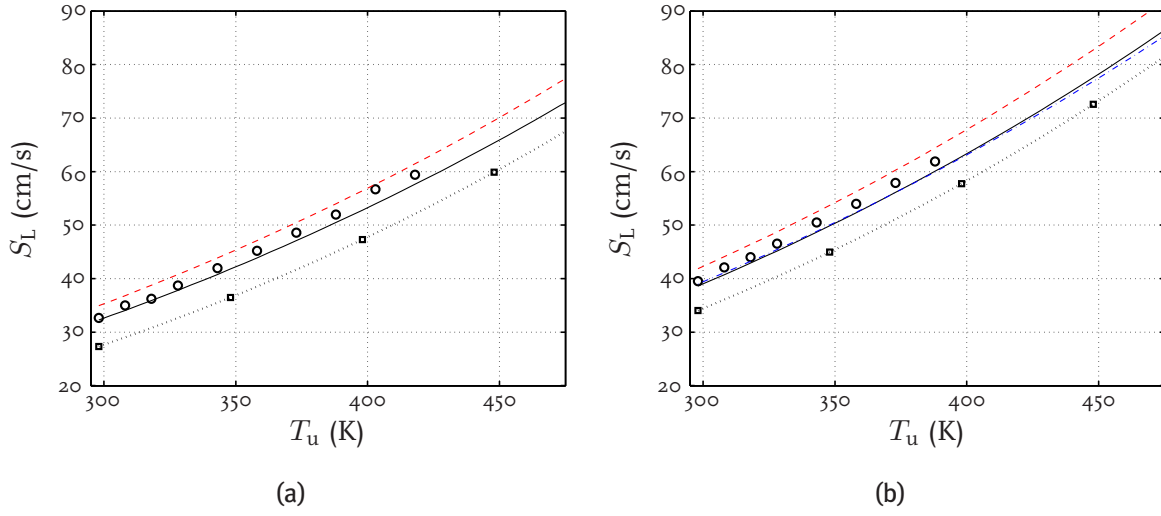


Figure 5.14: Experimentally and numerically determined laminar burning velocities of methane-hydrogen-air flames for an equivalence ratio of 1.2; $\mathcal{R}_{\text{H}_2} = 0\%$ (left) and $\mathcal{R}_{\text{H}_2} = 20\%$ (right). The heat flux data are denoted with circles, GRI-mechanism [97], solid line; Leeds mechanism [53], dotted line with square symbols; SKGo3 [96], dashed dotted line and the GDF-kin mechanism [27], dashed line.

is consistent for all equivalence ratios and hydrogen contents. The difference between experiments and numerical results is relatively small for stoichiometric flames. This is consistent with the methane-hydrogen-air results at ambient conditions where a relatively small difference between numerical and experimental data occurs close to stoichiometric conditions. Generally the difference between experiments and the numerically determined burning velocities using the GRI mechanism [97] is small, for fuel lean flames and stoichiometric flames almost everywhere inside the error estimate. For fuel lean and fuel rich flames the difference between experimental data and numerical data of the other mechanisms is slightly larger.

Correlation for the Burning Velocity as a function of the unburnt temperature

Experimental results of the laminar burning velocity as a function of the unburnt gas temperature are usually expressed as simple polynomial functions. Metghalchi and Keck [76] proposed the following relation:

$$S_L = S_{L,0} \left(\frac{T_u}{T_0} \right)^{\alpha_T} \left(\frac{p_u}{p_0} \right)^{\beta_p}, \quad (5.5)$$

with $T_0 = 293 \text{ K}$ and $p_0 = 1 \text{ atm}$. The temperature dependent burning velocities of atmospheric methane-hydrogen-air flames of the experimental and numerical data presented in this section have been used to determine α_T . In table 5.2 this coefficient is listed for two hydrogen contents $\mathcal{R}_{\text{H}_2} = 0\%$ and 20% and three equivalence ratios. Also listed in table 5.2 is the experimentally determined α_T of Gu et al. [39]. For stoichiometric flames the coefficient α_T is lower compared to the fuel lean and fuel rich flames.

Table 5.2: Temperature coefficient α_T of equation (5.5) for experimental and numerical data.

Data	$\mathcal{R}_{H_2}=0\%$			$\mathcal{R}_{H_2}=20\%$		
	$\phi=0.80$	$\phi=1.00$	$\phi=1.20$	$\phi=0.80$	$\phi=1.00$	$\phi=1.20$
Heat flux	1.87	1.65	1.78	1.83	1.61	1.69
GRI-mech 3.0 [97]	1.84	1.69	1.78	1.84	1.64	1.76
Leeds [53]	1.85	1.71	1.94	1.85	1.70	1.88
GDF-kin [27]	1.88	-	1.71	-	1.68	1.69
SKGo3 [96]	-	1.65	-	1.84	1.65	1.67
Gu et al. [39]	2.11	1.61	2.00	-	-	-

This is consistent for the experimental as well as the numerical results. The Leeds mechanism [53] has a slightly higher temperature coefficient for fuel rich mixtures compared to the other data. The difference in temperature coefficient between the other mechanisms and the heat flux data is relatively small. The experimental data of Gu [39] show significantly larger values for fuel lean flames and fuel rich flames compared to the heat flux data. This is probably due to the large scatter in experimental results presented by Gu et al. which is already recognised in the previous chapter (see figure 4.16). The heat flux data and numerically determined α_T decrease slightly with increasing hydrogen content.

5.5 Summary

The comparison between the experimental heat flux data and the numerical data in this chapter gives a good overview of the performance of recent combustion mechanisms concerning the laminar burning velocities for the investigated parameter range.

The first set of experimentally determined burning velocities consisting of hydrogen-oxygen-nitrogen flames are compared with hydrogen based combustion reaction mechanisms as well as methane based mechanisms. The hydrogen based mechanisms perform quite well for the highly diluted mixtures with nitrogen. The maximum burning velocity for $\mathcal{R}_{O_2} = 7.7\%$ is slightly underpredicted. Overall the performance of the hydrogen based Konnov mechanism [61] is quite good. Compared to the other methane based mechanisms the performance of the SKGo3 mechanism [96] for these highly diluted flames is very well, even the difference with the hydrogen based mechanisms is not that large sometimes even better. The GRI-mechanism [97] shows significant differences compared to the heat flux data for these hydrogen-oxygen-nitrogen flames highly diluted with nitrogen.

The methane based mechanisms are also used to compare the laminar burning velocities of methane-hydrogen-air flames as a function of equivalence ratio and hydrogen content with experimentally determined heat flux data. This second set of data at ambient conditions shows that the SKGo3 mechanism [96] performs very well for the investigated

parameter range. Also the GRI-mechanism [97] gives good results, it only deviates notably from the experimental data for higher hydrogen contents.

The laminar burning velocity results using the GRI-mechanism [97] for methane-hydrogen-air mixtures at increased unburnt gas temperatures are for the measured range close to the experimental data. In the case of the SKGo₃ mechanism [96] the differences between experiments and numerical data are slightly larger for fuel lean and fuel rich flames. For stoichiometric flames the differences between the heat flux data and the numerical data determined with the GRI-mechanism and SKGo₃ mechanism are small.

Asymptotic Theory for Stoichiometric Methane-Hydrogen-Air Flames

An asymptotic theory for stoichiometric methane-hydrogen-air flames is presented in this chapter. To that end the theory of Peters and Williams [82] for methane-air flames is adapted for methane-hydrogen-air flames. Understanding of the structure is used to identify appropriate assumptions that in the end lead to results for basic flame properties. First the methane-hydrogen-air theory will be derived followed by an analysis of the effect of hydrogen addition on the flame structure, as predicted by the asymptotic theory. Finally, this chapter ends with a comparison of the laminar burning velocity results from the asymptotic theory with experiments and numerical simulations.

6.1 Introduction

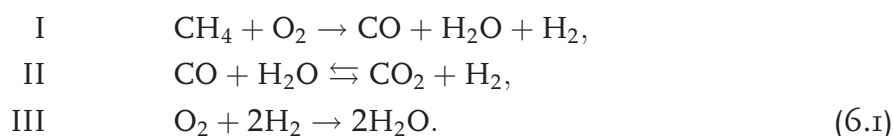
In this chapter, the basic phenomena explaining the flame structure and propagation velocity of stoichiometric methane-hydrogen-air flames are analysed. Certainly detailed numerical simulations using full chemistry can be used to determine basic flame properties, e.g. burning velocity, species concentrations. However, due to the huge amount of information delivered by these mechanisms it is difficult to get a basic understanding of the fundamental parameters that influence the flame. Another option to analyse these fundamental parameters is by using asymptotic theory. This kind of approach provides the basis to analyse the basic phenomena explaining the flame structure, which makes use of reduced kinetic mechanisms. The resulting models derived in literature and used for asymptotic analysis range from one-step to four-step mechanisms. By increasing the number of reaction steps in the model generally the level of complexity and accuracy of the model increases. Starting with simple one-step chemistry and using an asymptotic analysis of the flame structure. It is commonly based on Arrhenius approximations

with a scaled activation energy treated as a large parameter (Zel'dovich number) [113]. This kind of analysis is also termed as activation-energy asymptotics (AEA). This approach requires knowledge of overall rate parameters, e.g. activation energy itself. For most flames, these parameters are taken as complex fits [72] over a limited range of conditions [114]. Another approach in describing the asymptotic structure of flames and is known as rate-ratio asymptotics (RRA). The basic flames properties derived by rate-ratio asymptotics give only qualitative results but the understanding of the investigated flames is improved [114]. Applying asymptotic analysis with multiple reactions, e.g. two-step chemistry, more and more basic chemical parameters are being retained [82] and resulting accuracy of the equations describing flame properties like the laminar burning velocity increases. Applying asymptotic analysis to three or four-step mechanisms to derive basic flame properties gives already good agreement [114]. However, it turns out that the asymptotic analysis is becoming rather complex due to the large number of parameters that are involved in this kind of analysis.

Several asymptotic models are available in literature not only for methane-air or higher hydrocarbon flames [84, 91, 92] but also for hydrogen-air flames [94]. Most asymptotic theories available in literature describe the combustion of a single fuel, rather than fuel mixtures. The analysis of methane-hydrogen-air flames described in this chapter is based on the asymptotic theory of Peters and Williams [82] which is adapted from stoichiometric methane-air flames. The derivation of the theory is similar as the one introduced by Peters and Williams [82]. The most important difference is the scaling procedure associated with addition of hydrogen at the unburnt side. The relations found in the present theory will be compared with the original theory for the pure methane situation. The original version has proved to be successful in describing qualitatively the dependence of the burning velocity on pressure and preheating of the mixture [82]. Later extensions of the asymptotic theory of Peters and Williams make the results more quantitative, e.g. [91, 93]. The present analysis is based on the leading-order formulation of the methane-air theory, which is discussed in detail by Peters [80].

Reaction Mechanism Reduction

The analysis of Peters and Williams [80, 82] starts with the skeletal mechanism of Smooke [98]. This combustion reaction mechanism with its species involved, reactions, reaction rates, pre-exponential factors, temperature dependence and species efficiency is listed in Appendix A. It is suitable for lean and stoichiometric methane-air flames [98]. It is not developed for rich flames because this reaction mechanism does not include the path to higher hydrocarbons; it considers only C1 chemistry. Since the asymptotic theory presented here only involves stoichiometric methane-hydrogen-air flames, this mechanism is also a proper starting point, as it contains also the sub-mechanism for hydrogen-air combustion. First, Peters derived the well-known four-step mechanism [79], which is subsequently reduced to a three-step mechanism by taking H-radicals in steady-state. The resulting global reactions are



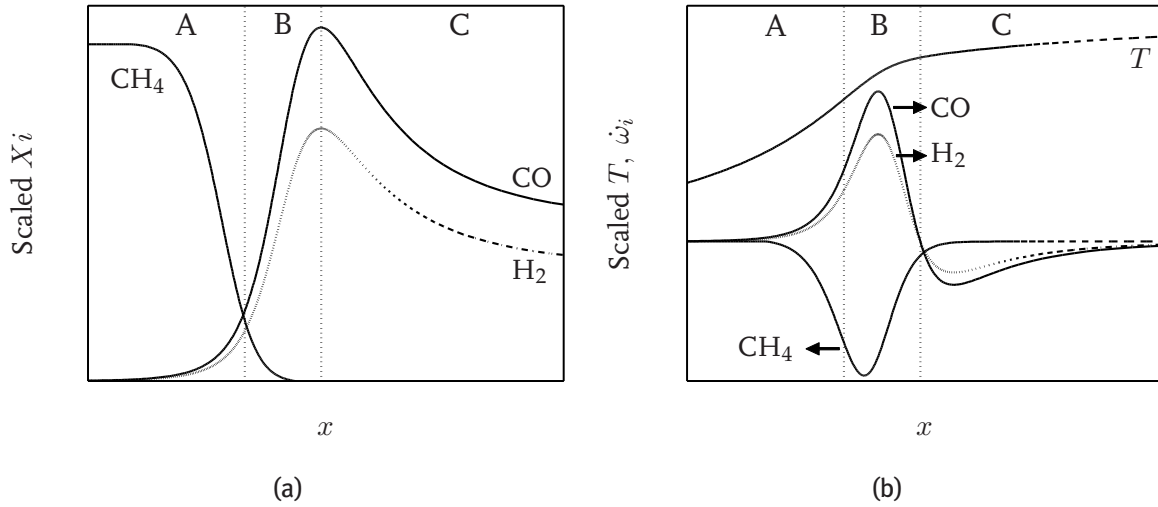


Figure 6.1: Schematic representation of the structure of a stoichiometric methane-air flame as a function of the coordinate x . Left figure: species concentrations. Right figure: species source terms and temperature. According to the asymptotic theory of Peters and Williams [82] the flame is divided into three layers, A) preheat zone, B) inner layer and C) oxidation layer.

In the present analysis the assumption is made that the amount of hydrogen in the fuel is relative low, so that the same equilibrium assumptions can be made as for stoichiometric methane-air flames. Hence, the same reduced four- and three-step mechanisms are also valid for methane-hydrogen-air mixtures¹. In the classical work of Peters and Williams [80, 82] the next step is to reduce this three-step mechanism to an effective two-step mechanism. As will be shown in section 6.1.2 this reduction is done by assuming partial equilibrium of the water-gas-shift reaction (reaction II). This two-step mechanism is used to describe the basic structure of a methane-air flame. The identified structure relies entirely on the competition between rate coefficients since the relevant activation energies are of only moderate magnitude [82]. The basic structure derived is shown in figure 6.1. This schematic representation of a stoichiometric methane-air flame is the result of the analysis of Peters and Williams [82]. Due to the approximations made when deriving the two step mechanism, the derived structure resembles only globally the result of a detailed simulation. A simulation with the Smooke mechanism [98] shown in figure 6.2, gives a detailed analysis of the flame front.

According to Peters and Williams [82] the stoichiometric methane-air flame consists out of a chemically inert preheat zone followed by a thin inner layer where fuel is consumed and hydrogen and carbon monoxide are produced. Downstream from this inner layer there is a broader but still thin layer where the hydrogen and carbon monoxide oxidation takes place. This is called the oxidation layer.

In this chapter it is shown that a premixed methane-hydrogen-air flame generally behaves

¹. The reader is referred to the work of Peters and Williams [80, 82] for an elaborated discussion on the derivation of the reduced four-step and three-step mechanism.

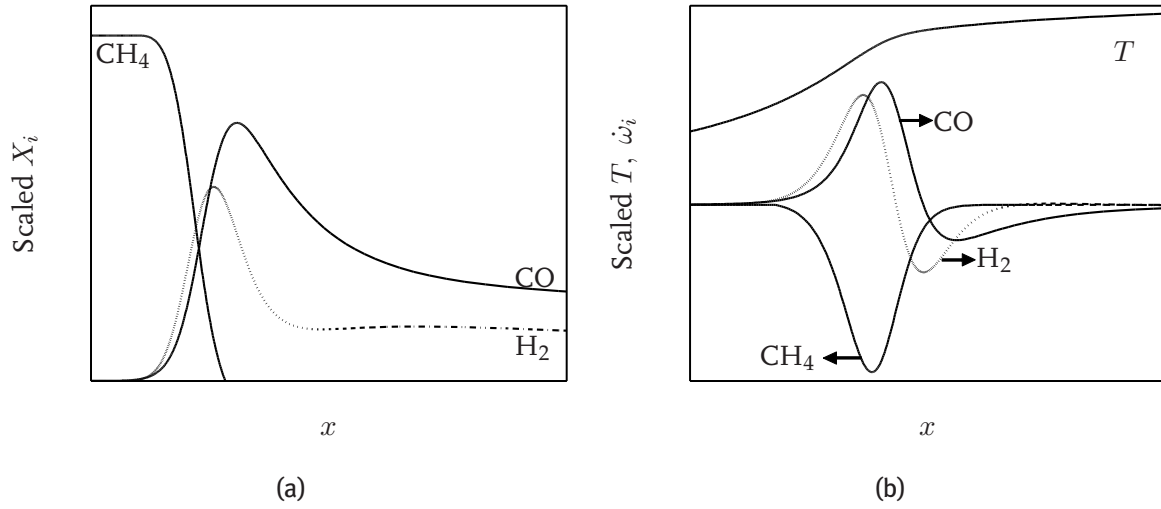


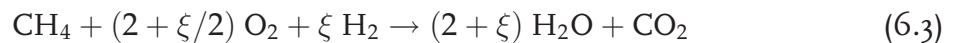
Figure 6.2: Left figure: Methane, hydrogen and carbon monoxide species concentrations profiles of a stoichiometric methane-air flames determined with the Smooke mechanism [98]. Right figure: the source terms of the same species and additionally the temperature profile.

as a methane-air flame in the sense that the methane is first converted into hydrogen and carbon monoxide in the inner layer, while these species are oxidised in the oxidation layer. The extra amount of hydrogen in the unburnt mixture survives the inner layer, where more of it is produced from the methane part. This was to be expected because the weaker C-H bonds in methane break-up at lower temperatures than the stronger H-H bonds in molecular hydrogen. The production rate of molecular hydrogen in the inner layer decreases in comparison with a pure methane flame, because less methane is available to break-up. Now the hydrogen formation by this methane break-up, although in smaller amounts, together with the hydrogen which is already available at the unburnt mixture causes this increase of hydrogen at the inner layer. This induces a change in the inner layer temperature, the adiabatic flame temperature and the laminar burning velocity. Analytical expressions describing these changes in inner layer temperature, adiabatic flame temperature and the resulting laminar burning velocity for increasing hydrogen contents are derived in this chapter.

The expressions derived here for premixed combustion of stoichiometric methane-hydrogen-air mixtures is studied as a function of the parameter ξ , which is defined as

$$\xi = \frac{X_{\text{H}_2, \text{u}}}{X_{\text{CH}_4, \text{u}}}, \quad (6.2)$$

being is the molar ratio of hydrogen and methane in the fuel. For studies of hydrogen addition on a mass basis, ξ has to be scaled with the ratio of molar masses, i.e. with a value $\approx 2/16$. Furthermore, for stoichiometric mixtures the global reaction may be written as follows



For complete combustion $2 + \xi/2$ moles of oxygen are used to burn the fuel instead of 2 moles for a pure methane flame. Hence, more oxygen is needed for complete combustion

The next section is divided into three main parts. In the first part the conservation equations which have been introduced in section 2.1.1 are written in a non-dimensionalised form. This is followed by a subsection where the three-step mechanism presented above, and reduced to an effective two-step mechanism. In the remaining section this two-step mechanism, which separates the flame in three layers, is being analysed.

6.1.1 Non-dimensionalised Conservation Equations

In this section the conservation equations are simplified and finally written in non-dimensionalised form. A similar non-dimensionalisation of the species balance equations has been applied as Peters and Williams [80, 82]. Here the variables are non-dimensionalised with respect to the pure methane situation $\xi = 0$. To emphasis the difference with the present theory: they non-dimensionalised with respect to the fuel. Instead of conservation equations written in terms of complex diffusion models, see section 2.1.1, the constant Lewis number approximation is used. The Lewis numbers describing species diffusion, are defined as the ratio of thermal diffusivity to species diffusivity. This gives for each species,

$$Le_i = \frac{\lambda_g}{\rho_u c_p D_{im}} \quad (6.4)$$

where ρ_u is the unburnt density of the gas mixture, λ_g the thermal conductivity, c_p the mean specific heat and the diffusion coefficient D_{im} which describes the diffusion of species i with respect to the mixture. The relation λ_g/c_p for hydrocarbon-air combustion can be approximated according to Smooke [98] by:

$$\frac{\lambda_g}{c_p} = 2.58 \times 10^{-3} \left(\frac{T}{T_{\text{ref}}} \right)^{0.69}, \quad (6.5)$$

where T^{ref} is 298 K.

Now, the steady 1D conservation equation (2.4) of the chemical species i , where u equals the laminar burning velocity S_L , for the three step mechanism can be expressed as:

$$\rho_u S_L \frac{\partial Y_i}{\partial x} - \frac{1}{Le_i} \frac{\partial}{\partial x} \left(\frac{\lambda_g}{c_p} \frac{\partial Y_i}{\partial x} \right) = M_i \sum_{j=1}^{N_r} (\nu''_{ij} - \nu'_{ij}) r_j, \quad i \in [1, N_s], \quad (6.6)$$

where x is the spatial coordinate and N_r the number of reactions involved, which are the reactions indicated with I, II and III and the number of species involved are $N_s = 6$, see equation (6.3). Similar, the steady 1D energy equation (2.3) presented here in terms of temperature can be written as:

$$\rho_u S_L \frac{\partial T}{\partial x} - \frac{\partial}{\partial x} \left(\frac{\lambda_g}{c_p} \frac{\partial T}{\partial x} \right) = \frac{1}{c_p} \sum_{j=1}^{N_r} Q_j r_j \quad (6.7)$$

with Q_j the heat of reaction and r_j is the reaction rate of reaction j .

A spatial non-dimensionalisation is applied to equations (6.6) and (6.7), using the parameter y , which refers to the spatial coordinate in terms of the flame thickness. This non-dimensional coordinate y is defined as,

$$y = \rho_u S_L \int_0^x \left(\frac{c_p}{\lambda_g} \right) dx', \quad (6.8)$$

and $y = 0$ is taken to coincide with the location of the centre of the inner layer. In the present analysis, the flame thickness is considered as a diffusion length scale by assuming that the preheat zone is chemically inert. Hence, according to Götting et al. [38] the flame thickness is given by

$$l_f = \frac{\lambda_g/c_p}{\rho_u S_L}, \quad (6.9)$$

where λ_g/c_p is evaluated at the inner layer. The variables Y_i , Q_j , T occurring in the species balance equation (6.6) and energy equation (6.7) are non-dimensionalised by referring the variables to the pure methane situation. The scaled temperature, is given by

$$\tau = \frac{\int_{T_u}^{T^\xi} c_p^\xi(t) dt}{\int_{T_u}^{T_{ad}^0} c_p^0(t) dt}, \quad (6.10)$$

where $c_p(t)$ is the temperature-dependent specific heat of the burnt gases and T_{ad} is the adiabatic flame temperature. The superscript 0 indicates that the variable is determined at the pure methane situation whereas the superscript ξ indicates that the variable is determined at a certain hydrogen content ξ . This equation for τ is a function of x , because T^ξ is a function of x . This scaled temperature τ is a measure for the relative temperature increase of the flame compared to the methane-air flame. The scaled heat of reaction is given by

$$Q'_j = \frac{Q_j Y_{CH_4}^0}{M_{CH_4}} \int_{T_u}^{T_{ad}^0} c_p^0(t) dt \quad (6.11)$$

where Q_j is the unscaled heat of reaction j . The non-dimensionalised mass fractions now become

$$X'_i = \frac{X_i^\xi}{X_{CH_4,u}^0} = \frac{Y_i M_{CH_4}}{Y_{CH_4,u}^0 M_i}, \quad \text{and} \quad x_i = \frac{X'_i}{Le_i}, \quad (6.12)$$

where Y_i and M_i , are the unscaled mass fractions and molar masses respectively. Note that X'_i in the remaining part of this chapter is *not* the commonly used molar fraction but the scaled mole fraction. Furthermore, it is important to realise that the fuel mass fraction of a stoichiometric methane-air mixture *without* hydrogen, is $Y_{CH_4,u}^0 = 0.055$, are used in the scaling procedure presented in equations (6.10) and (6.12). Scaling with the pure methane mass fraction is convenient because it allows for a direct comparison of methane-hydrogen-air flames with pure methane-air flames. Equation (6.12) together with equation (6.3) are used to determine $X'_{CH_4,u}$ and $X'_{H_2,u}$ which will be used frequently

in this chapter:

$$\begin{aligned} X'_{\text{CH}_4,\text{u}} &= \frac{2}{2 + \xi/2} = \frac{1}{1 + \xi/4}, \\ X'_{\text{H}_2,\text{u}} &= \frac{\xi}{1 + \xi/4}. \end{aligned} \quad (6.13)$$

Note that the ratio of $X'_{\text{H}_2,\text{u}}$ and $X'_{\text{CH}_4,\text{u}}$ is equal to ξ and for pure methane flames $\xi = 0$ and $X'_{\text{CH}_4,\text{u}} = 1$ as it should be according to equation (6.2).

Several variables have been scaled and non-dimensionalised above. The energy and species balance equations remain to be non-dimensionalised. These equations can be written in terms of 1D steady transport operators,

$$\mathcal{L}_i = Le_i \frac{d}{dy} - \frac{d^2}{dy^2}, \quad \mathcal{L}_\tau = \frac{d}{dy} - \frac{d^2}{dy^2}, \quad (6.14)$$

with \mathcal{L}_i and \mathcal{L}_τ the transport operators for respectively species and temperature. Using the species transport operators, gives for the species balance equation (6.6) the following non-dimensionalised relations:

$$\mathcal{L}_i(x_i) = Le_i \frac{dx_i}{dy} - \frac{d^2 x_i}{dy^2} = \sum_{j=1}^{N_r} \nu_{ij} w_j, \quad (6.15)$$

where the reaction rates are non-dimensionalised according to,

$$w_j = \frac{\lambda_g M_{\text{CH}_4} r_j}{c_p Y_{\text{CH}_4,\text{u}}^0 \rho_u^2 S_L^2}. \quad (6.16)$$

Similar, by writing the temperature balance equation (6.7) in a non-dimensionalised form by using the temperature operator results in:

$$\mathcal{L}_\tau(\tau) = \sum_{j=1}^{N_r} Q'_j w_j \quad (6.17)$$

The three step mechanism presented in equation (6.1) together with the non-dimensionalised conservation equations of this three step mechanism shown in equation (6.15) and (6.17) results in the following balance equations

$$\begin{aligned} \mathcal{L}_{\text{CH}_4}(x_{\text{CH}_4}) &= -w_{\text{I}} \\ \mathcal{L}_{\text{O}_2}(x_{\text{O}_2}) &= -w_{\text{I}} - w_{\text{III}} \\ \mathcal{L}_{\text{H}_2}(x_{\text{H}_2}) &= w_{\text{I}} + w_{\text{II}} - 2w_{\text{III}} \\ \mathcal{L}_{\text{CO}}(x_{\text{CO}}) &= w_{\text{I}} - w_{\text{II}} \\ \mathcal{L}_{\text{H}_2\text{O}}(x_{\text{H}_2\text{O}}) &= w_{\text{I}} - w_{\text{II}} + 2w_{\text{III}} \\ \mathcal{L}_{\text{CO}_2}(x_{\text{CO}_2}) &= w_{\text{II}} \\ \mathcal{L}_\tau(\tau) &= Q'_1 w_{\text{I}} + Q'_2 w_{\text{II}} + Q'_3 w_{\text{III}}. \end{aligned} \quad (6.18)$$

These non-dimensionalised equations and variables, presented in equations (6.8), (6.10) - (6.12), (6.16) and (6.18) are used in the remaining part of this chapter to analyse the flame structure of methane-hydrogen-air flames. However, before the flame structure can be analysed the three step mechanism in equation (6.1) is further reduced to an effective two-step mechanism.

6.1.2 Two-step Mechanism

The set of related conservation equations is reduced to a two-step system by using steady-state assumptions for reacting species with the smallest chemical time scales. If the amount of hydrogen in the fuel is not too large, identical equilibrium assumptions can be introduced as in the pure methane case and the same two-step mechanism is valid for methane-hydrogen-air mixtures. When a Damköhler number, Da , is sufficiently large (fast chemistry), which happens for instance with reaction II, then this reaction can be written as (either X'_i or X_i can be used),

$$X_{\text{CO}_2} X_{\text{H}_2} = K_{\text{II}}(T) X_{\text{H}_2\text{O}} X_{\text{CO}}, \quad (6.19)$$

where $K_{\text{II}}(T)$ is the equilibrium constant of this reaction. In the derivation of the two-step mechanism, one fixes the ratio α of the mole fractions of carbon monoxide and hydrogen in the reaction zone. This ratio is related to the water-gas-shift equilibrium of reaction II in the reaction layer according to

$$x_{\text{CO}} = \alpha x_{\text{H}_2}. \quad (6.20)$$

Hence, equation (6.19) can be written as,

$$\alpha = \frac{Le_{\text{H}_2} X_{\text{CO}_2}}{Le_{\text{CO}} X_{\text{H}_2\text{O}} K_{\text{II}}(T)}. \quad (6.21)$$

Throughout the reaction zones the ratio of water and carbon dioxide typically differs little from its value at downstream infinity [82], as a result α can be seen as a function of temperature only. By pretending that α is constant, which is one of the assumptions made in figure 6.1a, a further approximation of the flame structure can be achieved; the temperature T and X_i in equation (6.21) are taken at the inner layer. By introducing α , the reaction rate w_{II} can be eliminated from the conservation equations. From the conservation equations of the three step mechanism presented in equation (6.15) and (6.17) the following relations are found. When combining the balance equations of hydrogen, water and carbon dioxide with that of carbon monoxide:

$$\mathcal{L}_{\text{CH}_4}(x_{\text{CH}_4}) = -w_{\text{I}} \quad (6.22a)$$

$$\mathcal{L}_{\text{O}_2}(x_{\text{O}_2}) = -w_{\text{I}} - w_{\text{III}} \quad (6.22b)$$

$$\mathcal{L}_{\text{H}_2}(x_{\text{H}_2}) + \mathcal{L}_{\text{CO}}(x_{\text{CO}}) = 2w_{\text{I}} - 2w_{\text{III}} \quad (6.22c)$$

$$\mathcal{L}_{\text{H}_2\text{O}}(x_{\text{H}_2\text{O}}) - \mathcal{L}_{\text{CO}}(x_{\text{CO}}) = 2w_{\text{III}} \quad (6.22d)$$

$$\mathcal{L}_{\text{CO}_2}(x_{\text{CO}_2}) + \mathcal{L}_{\text{CO}}(x_{\text{CO}}) = w_{\text{I}} \quad (6.22e)$$

$$\mathcal{L}_{\tau}(\tau) - Q'_{\text{II}} \mathcal{L}_{\text{H}_2}(x_{\text{H}_2}) = (Q'_{\text{I}} - Q'_{\text{II}}) w_{\text{I}} + (Q'_{\text{III}} + 2Q'_{\text{II}}) w_{\text{III}}. \quad (6.22f)$$

None of the given coupling equations above rely anymore on the reaction rate w_{II} of the water-gas-shift reaction. Inserting equation (6.20) in equation (6.22c) together with the 1D transport operator of equation (6.14) gives:

$$\left(1 + \alpha \frac{Le_{\text{CO}}}{Le_{\text{H}_2}}\right) Le_{\text{H}_2} \frac{d}{dy} x_{\text{H}_2} - (1 + \alpha) \frac{d^2}{dy^2} x_{\text{H}_2} = 2w_{\text{I}} - 2w_{\text{III}}. \quad (6.23)$$

The convective terms in the reaction layers are small in comparison with the diffusion terms [82], so that equation (6.23) can be approximated by

$$(1 + \alpha) \mathcal{L}_{\text{H}_2}(x_{\text{H}_2}) \approx 2w_{\text{I}} - 2w_{\text{III}}. \quad (6.24)$$

As a consequence this equation can be seen as the conservation equation for hydrogen. The remaining relations which express the conservation of species and temperature, follow from the linear combinations of equation (6.22):

$$\mathcal{L}_{\text{CH}_4}(x_{\text{CH}_4}) = -w_I \quad (6.25a)$$

$$\mathcal{L}_{\text{O}_2}(x_{\text{O}_2}) = -w_I - w_{\text{III}} \quad (6.25b)$$

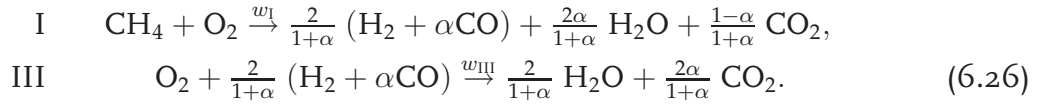
$$\mathcal{L}_{\text{H}_2}(x_{\text{H}_2}) = \frac{2}{1+\alpha}w_I - \frac{2}{1+\alpha}w_{\text{III}} \quad (6.25c)$$

$$\mathcal{L}_{\text{CO}}(x_{\text{CO}}) = \frac{2\alpha}{1+\alpha}w_I - \frac{2\alpha}{1+\alpha}w_{\text{III}} \quad (6.25d)$$

$$\mathcal{L}_{\text{H}_2\text{O}}(x_{\text{H}_2\text{O}}) = \frac{2\alpha}{1+\alpha}w_I + \frac{2}{1+\alpha}w_{\text{III}} \quad (6.25e)$$

$$\mathcal{L}_{\text{CO}_2}(x_{\text{CO}_2}) = \frac{1-\alpha}{1+\alpha}w_I + \frac{2\alpha}{1+\alpha}w_{\text{III}}. \quad (6.25f)$$

These balance equations correspond to a two-step stoichiometric methane-air reaction mechanism represented by the following reactions:



Here the first reaction with the reaction rate w_I is the source of the inner layer, where methane is converted into a mixture of carbon monoxide and hydrogen. The second reaction denoted with III and the reaction rate w_{III} is the source of the oxidation layer. In this layer carbon monoxide and hydrogen are converted into products which are assumed to be only carbon dioxide and water for stoichiometric mixtures. The mixture of carbon monoxide and hydrogen can be seen as a kind of intermediate species which is formed in reaction I and consumed in reaction III. Instead of considering the mole based ratio, in equation (6.20) one can also set the ratio's of reaction rates of carbon monoxide and hydrogen to α as well. This holds for a methane-air flame in the complete reaction zone. Indeed from equation (6.26) it is seen that $\alpha = \frac{w_{\text{I,CO}}}{w_{\text{I,H}_2}}$ and additionally $\alpha = \frac{w_{\text{III,CO}}}{w_{\text{III,H}_2}}$ as well.

Now, in the case of methane-hydrogen-air flames the ratio between carbon monoxide and hydrogen in the unburnt mixture cannot be equal to α anymore, because hydrogen is already present there while carbon monoxide is absent. This gives also a different ratio of production rates of $w_{\text{I,CO}}$ and $w_{\text{I,H}_2}$ in the inner layer by reaction I, because less hydrogen is formed due to a smaller amount of methane. The ratio between carbon monoxide and hydrogen production rates in the inner layer is now defined as:

$$\beta = \frac{w_{\text{I,CO}}}{w_{\text{I,H}_2}}. \quad (6.27)$$

In the oxidation layer corresponding to reaction III hydrogen and carbon monoxide are consumed and vanish both in the burnt gases. The ratio between them in this layer is constant although not equal to the pure methane situation since more hydrogen is produced in the inner layer. As $x_{\text{CO}} = \alpha x_{\text{H}_2}$ should hold in the oxidation layer, we must have that $w_{\text{III,CO}} = \alpha w_{\text{III,H}_2}$.

Summarising, we now find $w_{\text{I,CO}} = \beta w_{\text{I,H}_2}$ and $w_{\text{III,CO}} = \alpha w_{\text{III,H}_2}$. Using this parameter β in the transport equations (6.18) gives for a methane-hydrogen-air mixture the following transport equations:

$$\mathcal{L}_{\text{CH}_4}(x_{\text{CH}_4}) = -w_{\text{I}} \quad (6.28a)$$

$$\mathcal{L}_{\text{O}_2}(x_{\text{O}_2}) = -w_{\text{I}} - w_{\text{III}} \quad (6.28b)$$

$$\mathcal{L}_{\text{H}_2}(x_{\text{H}_2}) = \frac{2}{1+\beta} w_{\text{I}} - \frac{2}{1+\alpha} w_{\text{III}} \quad (6.28c)$$

$$\mathcal{L}_{\text{CO}}(x_{\text{CO}}) = \frac{2\beta}{1+\beta} w_{\text{I}} - \frac{2\alpha}{1+\alpha} w_{\text{III}} \quad (6.28d)$$

$$\mathcal{L}_{\text{H}_2\text{O}}(x_{\text{H}_2\text{O}}) = \frac{2\beta}{1+\beta} w_{\text{I}} + \frac{2}{1+\alpha} w_{\text{III}} \quad (6.28e)$$

$$\mathcal{L}_{\text{CO}_2}(x_{\text{CO}_2}) = \frac{1-\beta}{1+\beta} w_{\text{I}} + \frac{2\alpha}{1+\alpha} w_{\text{III}}. \quad (6.28f)$$

The derivation of this set of transport equations is analogous to equation (6.25). Note that for a pure methane flame β should be equal to α again, indicating that β is a function of the unburnt mixture condition. An important question is how β is related to α for a given mixture composition.

Coupling between α and β

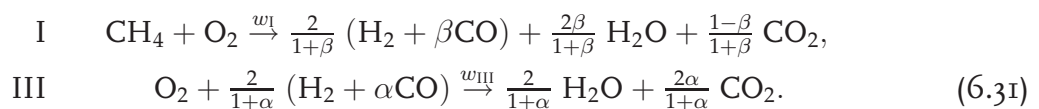
The coupling between β in the inner layer and α in the oxidation layer can be answered in two different ways. One way is to integrate the transport equations (6.28) over the complete flame structure. More specifically, integrating equations (6.28a), (6.28c) and (6.28d) for methane, hydrogen and carbon monoxide gives

$$\begin{aligned} -Le_{\text{CH}_4} x_{\text{CH}_4,\text{u}} &= - \int_{-\infty}^{\infty} w_{\text{I}}(y) \, dy, \\ -Le_{\text{H}_2} x_{\text{H}_2,\text{u}} &= \frac{2}{1+\beta} \int_{-\infty}^{\infty} w_{\text{I}}(y) \, dy - \frac{2}{1+\alpha} \int_{-\infty}^{\infty} w_{\text{III}}(y) \, dy, \\ 0 &= \frac{2\beta}{1+\beta} \int_{-\infty}^{\infty} w_{\text{I}}(y) \, dy - \frac{2\alpha}{1+\alpha} \int_{-\infty}^{\infty} w_{\text{III}}(y) \, dy, \end{aligned} \quad (6.29)$$

where the boundary conditions in the (un)burnt mixture are used. Assuming that carbon monoxide vanishes, while hydrogen does not in the unburnt mixture, the solution of this equation is

$$\frac{2(\beta - \alpha)}{\alpha(1 + \beta)} = \frac{X_{\text{H}_2,\text{u}}}{X_{\text{CH}_4,\text{u}}} = \frac{X'_{\text{H}_2,\text{u}}}{X'_{\text{CH}_4,\text{u}}} = \xi. \quad (6.30)$$

Another way to relate β to α is to derive the global reactions corresponding to equation (6.28) given by,



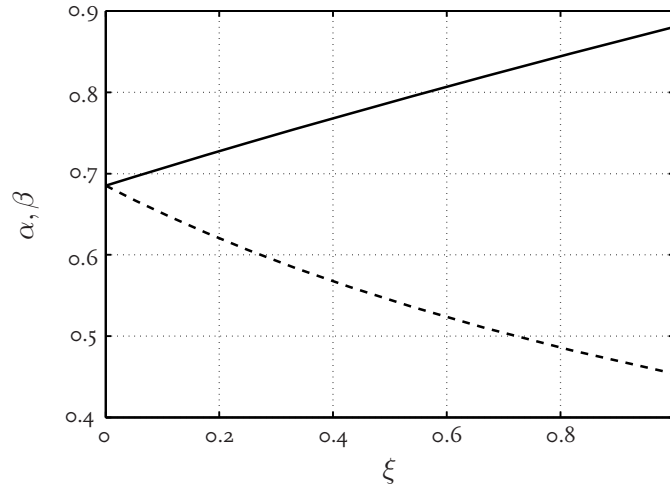
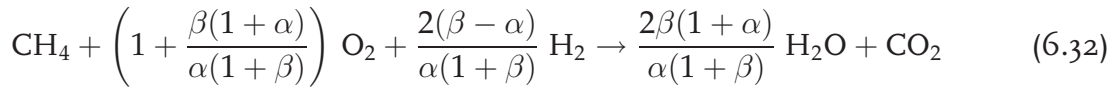


Figure 6.3: The ratio of the reaction rates of carbon monoxide and hydrogen for reactions I and III, defined by $w_{\text{I,CO}} = \beta w_{\text{I,H}_2}$ and $w_{\text{III,CO}} = \alpha w_{\text{III,H}_2}$ as a function of ξ . The ratio's are determined by equations (6.33), (6.21) and (6.63). The dashed line denotes α , and the solid line denotes β .

In the global reaction of a stoichiometric methane-hydrogen-air mixture, see equation (6.3), carbon monoxide does not occur, so the second equation has to be multiplied with $\frac{\beta(1+\alpha)}{\alpha(1+\beta)}$ and added to the first:



which should be equal to the global reaction in equation (6.3). This is only true if equation (6.30) holds. Hence, equation (6.30) determines the ratio of production rates in the inner layer:

$$\beta = \alpha \left(\frac{1 + \xi/2}{1 - \xi\alpha/2} \right). \quad (6.33)$$

Note however that the equilibrium of water and carbon dioxide in the flame indicated with α is also a function of ξ . To solve equation (6.33), α as a function of ξ needs to be determined. This is done by solving equation (6.21) at the inner layer, with the temperature at inner layer determined by equation (6.63), which will be introduced later. In figure 6.3 both α and β are plotted as a function of the hydrogen content given by equation (6.33). For $\xi = 0$ the pure methane relation is retrieved which means that $\beta = \alpha \approx 0.41$. With increasing hydrogen content α is decreasing mainly because of the significant decrease in inner layer temperature, whereas β is increasing moderately and almost linearly with increasing ξ .

Coupling relations between concentrations and temperature

The next step is to look at the coupling relations between the scalar variables x_i and the scaled temperature τ . Since we only have two different source terms w_{I} and w_{III} while there are 7 unknowns (x_i and τ), it is needed to derive 5 coupling relations between the

unknowns with a zero source from equation (6.28). The transport equation for τ now becomes:

$$\mathcal{L}_\tau(\tau) = \left(Q'_I + \frac{(1-\beta)}{(1+\beta)} Q'_{II} \right) w_I + \left(Q'_{III} + \frac{2\alpha}{(1+\alpha)} Q'_{II} \right) w_{III}, \quad (6.34)$$

where Q'_I , Q'_{II} and Q'_{III} are the heats of reaction of global reactions I, II and III relative to the heat of reaction Q of the total global methane-air reaction. Although, reaction II, has been eliminated above its heat of reaction is still appearing in equation (6.34). Peters and Williams observed that $q_{H_2} = Q'_{III}/2 = 0.3116$ and $q_{CO} = (Q'_{III}/2 + Q'_{II}) = 0.3479$. Using this, equation (6.34) can be written in terms of the sources of methane and hydrogen, which then gives together with equations (6.22a) and (6.22c):

$$\mathcal{L}_\tau(\tau) + (1 - \xi q_{CO} \alpha) \mathcal{L}_{CH_4}(x_{CH_4}) + (q_{H_2} + \alpha q_{CO}) \mathcal{L}_{H_2}(x_{H_2}) = 0. \quad (6.35)$$

This still holds for methane-hydrogen-air flames due to the scaling with methane-air situation, equation (6.10), and this scaling also leads to $Q'_I + Q'_{II} + Q'_{III} = 1$ as in the case without hydrogen. The numerical values of q_{H_2} and q_{CO} are sufficiently close together that they can be replaced by their mean, $q = 0.33$, as a first approximation [82]. Other combinations of equation (6.22) lead to the following coupling relations:

$$\begin{aligned} \mathcal{L}_{CO}(x_{CO}) + \mathcal{L}_{H_2}(x_{H_2}) + 4\mathcal{L}_{CH_4}(x_{CH_4}) - 2\mathcal{L}_{O_2}(x_{O_2}) &= 0 \\ \mathcal{L}_{H_2}(x_{H_2}) + 2\mathcal{L}_{CH_4}(x_{CH_4}) + \mathcal{L}_{H_2O}(x_{H_2O}) &= 0 \\ \mathcal{L}_{CO}(x_{CO}) + \mathcal{L}_{CH_4}(x_{CH_4}) + \mathcal{L}_{CO_2}(x_{CO_2}) &= 0 \end{aligned} \quad (6.36)$$

Note that the following relation is found between hydrogen, carbon monoxide and methane when using equations (6.24), equations (6.28c), equations (6.28d) and equations (6.30):

$$\mathcal{L}_{CO}(x_{CO}) - \alpha \mathcal{L}_{H_2}(x_{H_2}) + \alpha \xi \mathcal{L}_{CH_4}(x_{CH_4}) = 0. \quad (6.37)$$

If $\xi = 0$ is inserted in the equation (6.35) and equation (6.37), the coupling relations for pure methane as found by Peters and Williams are recovered.

The scaled adiabatic flame temperature τ is now found by integrating equation (6.35) over the flame and using equation (6.13)

$$\begin{aligned} \tau &= (1 - \xi q_{CO} \alpha) X'_{CH_4,u} + (q_{H_2} + \alpha q_{CO}) X'_{H_2,u} \\ &= (1 + q_{H_2} \xi) X'_{CH_4,u} \approx \left(\frac{1 + q_{H_2} \xi}{1 + \xi/4} \right). \end{aligned} \quad (6.38)$$

Since $q_{H_2} = 0.3116$, this equation indicates that τ increases slowly with increasing ξ .

Summarising, the balance equations have been non-dimensionalised in this section. The difference compared to the asymptotic theory of Peters and Williams [82] is the scaling with the pure methane situation. Furthermore, the three-step mechanism in equation (6.1) is reduced to a two-step mechanism, resulting in equation (6.31) The only difference of this two-step mechanism compared to the pure methane mechanism of Peters and Williams shown in equation (6.26) is that β instead of α is used in reaction I. The rates of these reactions are still the same as in the reactions I and III in the four and

three-step mechanism. According to Peters [80] the (unscaled) reaction rates are given by

$$\begin{aligned} r_I &= k_{11}X_{\text{CH}_4}X_{\text{H}}, \\ r_{II} &= \frac{k_{10}}{K_3} \frac{X_{\text{H}}}{X_{\text{H}_2}} \left(X_{\text{CO}}X_{\text{H}_2\text{O}} - \frac{1}{K_{II}}X_{\text{CO}_2}X_{\text{H}_2} \right), \\ r_{III} &= k_5X_{\text{H}}X_{\text{O}_2}X_M = pk_{III}X_{\text{O}_2}X_{\text{H}}, \end{aligned} \quad (6.39)$$

where $k_{III} = 1.6k_5/RT$. The concentration of H can be written as [80]

$$X_{\text{H}} = \frac{(K_{IV}X_{\text{O}_2}X_{\text{H}_2}^3)^{1/2}}{X_{\text{H}_2\text{O}}} \left(1 - \frac{k_{11}X_{\text{CH}_4}}{k_1} \right)^{1/2}, \quad (6.40)$$

which is found by assuming steady state of the H radical when reducing the four-step mechanism of Peters and Williams to the three-step mechanism given in equation (6.1). Note that reaction III with the rate r_{III} introduces the pressure dependence in the system of equations and will in the end determine the pressure dependence of the burning velocity.

6.2 Analysis of the Asymptotic Structure of Methane-Hydrogen-Air Flames

In this section the flame structure of methane-hydrogen-air flames is analysed by using the two-step mechanism shown in equation (6.31). The resulting flame structure of this two-step mechanism is shown in figure 6.4 and contains three layers similarly as in the theory of Peters and Williams:

- a chemical inert preheat zone of $\mathcal{O}(1)$ upstream,
- a thin inner layer of $\mathcal{O}(\delta)$ in which fuel is consumed by ω_I ,
- a thin oxidation layer of $\mathcal{O}(\epsilon)$ in which water and carbon dioxide are produced by ω_{III} .

By applying matched asymptotic analysis these three layers are coupled at the boundaries. The resulting analytic expressions, among them an implicit relation for the laminar burning velocity, give information concerning the basic flame structure. First the inner layer is analysed followed by the oxidation layer. Next a relation for inner layer temperature is retrieved and finally an equation for the laminar burning velocity is presented. In section 6.3 the relations found in this section are used to analyse the behaviour of hydrogen addition to a methane-air mixture. Note that in the remaining part of this chapter the following notation is used for subscripts and superscripts: the quantities determined at the inner layer are denoted with the subscript 0, the quantities which are a function of the hydrogen content are denoted with a superscript ξ , the quantities without hydrogen are denoted with a superscript 0. Finally the symbols denoted with a tilde are the quantities which are defined relative to the pure methane situation, e.g. $\widetilde{T}_{\text{ad}} = T_{\text{ad}}^\xi/T_{\text{ad}}^0$.

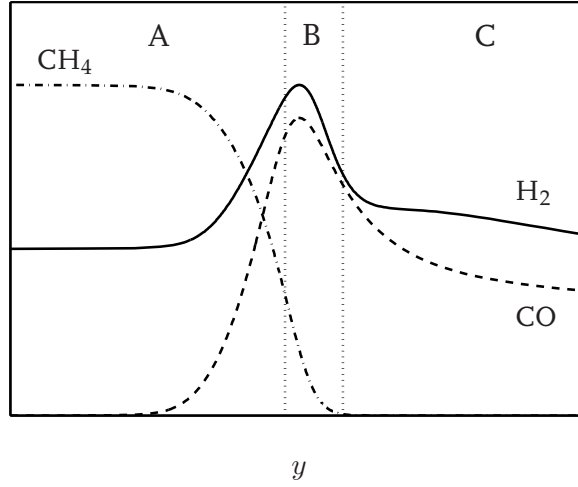


Figure 6.4: Schematic representation of the structure of a stoichiometric methane-hydrogen-air flame. The flame is divided into three layers, A) preheat zone, B) inner layer and C) oxidation layer.

Inner Layer

The procedure to analyse the inner layer is exactly the same as performed by Peters and Williams. Although in the present analysis the resulting boundary conditions will be different. In this layer all concentrations are assumed to be constant [82], except that of fuel which is being depleted. From equations (6.39) and (6.40) and using the scaled reaction rate of equations (6.16) gives,

$$w_I = Da_I x_{CH_4} \left(1 - \frac{x_{CH_4}}{\delta}\right)^{1/2}. \quad (6.41)$$

Here, the Damköhler number for reaction I, Da_I , is used. This is the ratio between diffusion and chemical time scales, and for the inner layer this is given by

$$Da_I = \frac{1}{\rho_u^2 S_L^2} \frac{Y_{CH_4,u}^0}{M_{CH_4}} \left(\frac{\lambda_g (K_{IV} X'_{O_2} X_{H_2}^3)^{1/2}}{c_p X'_{H_2O}} \right)_0 Le_{CH_4} k_{11}(T_0). \quad (6.42)$$

Also in equation (6.41) the inner layer thickness is introduced which is defined as,

$$\delta = \frac{k_1(T_0) X'_{O_2,0}}{k_{11}(T_0) Le_{CH_4}}. \quad (6.43)$$

This small parameter δ is the ratio of the rate coefficients of reaction 1 and 11. Since reaction rate k_1 is typically smaller than k_{11} and X'_{O_2} in the inner layer smaller than unity, this results in an inner layer thickness $\delta \approx 0.1$ which is small enough for asymptotic expansion. Figure 6.4 shows that the methane mole fraction in the preheat zone decreases rapidly, and the methane concentration in the inner layer is of $\mathcal{O}(\delta)$ and one may introduce the scaling

$$z' = \frac{x_{CH_4}}{\delta} \quad \text{and} \quad \zeta = \frac{y}{\delta}. \quad (6.44)$$

Combining this with equation (6.28a) and dropping the smaller convective term leads to a differential equation that governs the structure of the inner layer,

$$\frac{d^2 z'}{d\zeta^2} = \delta^2 Da_I z' \sqrt{1 - z'}. \quad (6.45)$$

Since reaction I is irreversible, and methane and oxygen are depleted far downstream for stoichiometric flames, the downstream boundary condition of equation (6.45) yields:

$$\zeta \rightarrow +\infty : z' = 0 \quad \text{and} \quad \frac{dz'}{d\zeta} = 0. \quad (6.46)$$

The matching with the preheat zone should give the second boundary condition. This upstream boundary condition should be able to reflect the change in methane when adding hydrogen to the unburnt mixture. The preheat zone methane concentration can be written as,

$$X'_{CH_4} = X'_{CH_4,u} (1 - \exp(Le_{CH_4} y)). \quad (6.47)$$

Now, using the expansion $\frac{dX'_{CH_4}}{dy} = -Le_{CH_4} X'_{CH_4}$ around $y = 0$, together with equation (6.44), results in the following upstream boundary condition for inner layer,

$$\zeta \rightarrow 0 : \frac{dz'}{d\zeta} = -X'_{CH_4,u}. \quad (6.48)$$

Note that this boundary condition is varying with hydrogen content, because the unburnt methane concentration, $X'_{CH_4,u}$ is decreasing with increasing hydrogen content. Integrating equation (6.45) and using the boundary conditions presented in equations (6.46) and (6.48), leads to

$$\delta^2 Da_I = \frac{15}{8} X'^2_{CH_4,u}. \quad (6.49)$$

This equation together with equation (6.42) could be used to determine the burning velocity if the inner layer temperature T_0 and all the other properties which have to be determined at the inner layer were known. In order to determine these properties also the structure of the oxidation layer should be resolved as is accomplished in the next subsection.

Oxidation Layer

The procedure to analyse the oxidation layer structure is again similar as in the theory of Peters and Williams. Also here, the boundary conditions of the oxidation layer changes, due to the added hydrogen to the unburnt mixture. Since most chemical activity in the oxidation layer takes place close to the inner layer, all properties are evaluated at $y = 0$. In the oxidation layer the fuel is depleted and $w_1 = 0$ and equations (6.24) and (6.35) can be written as

$$(1 + \alpha) \mathcal{L}_{H_2}(x_{H_2}) = 2w_{III} \quad (6.50a)$$

$$\mathcal{L}_\tau(\tau) + q(1 + \alpha) \mathcal{L}_{H_2}(x_{H_2}) = 0 \quad (6.50b)$$

by assuming $q_{\text{H}_2} \approx q_{\text{CO}} \approx q$. The stretchings

$$\begin{aligned} 2qy &= \epsilon\eta, & q(1 + \alpha)x_{\text{H}_2} &= \epsilon z, & x_{\text{O}_2} &= \epsilon z_{\text{O}_2}, \\ x_i &= x_{i,b} - \epsilon z_i & \text{with } i &= \text{H}_2\text{O}, \text{CO}_2, \\ \tau &= 1 - \epsilon t \end{aligned} \quad (6.51)$$

are introduced with ϵ the oxidation layer thickness which is assumed to be a small parameter. Integrating equations (6.36) and (6.50b) and using matching boundary conditions that the values and gradients of the quantities z_{H_2} , z_{CO} , $z_{\text{H}_2\text{O}}$, z_{CO_2} and t vanish at $\eta \rightarrow \infty$. This leads to the following relations as a first approximation

$$\begin{aligned} t &= z, & z_{\text{O}_2} &= \frac{z}{2q}, \\ z_{\text{H}_2\text{O}} &= \frac{z}{(1 + \alpha)q}, & z_{\text{CO}_2} &= \frac{\alpha z}{(1 + \alpha)q}. \end{aligned} \quad (6.52)$$

Now, only equation (6.50a) remains to be solved in the oxidation layer. The source terms appearing in equation (6.22c) can be written in terms of the stretchings, shown in equation (6.51), by using equations (6.39), (6.12), and (6.16), which gives for reaction III,

$$w_{\text{III}} = 2qDa_{\text{III}}\epsilon^3 z^3, \quad (6.53)$$

with the relevant Damköhler number for this reaction given by the expression:

$$Da_{\text{III}} = \frac{1}{\rho_u^2 S_L^2} \frac{Y_{\text{CH}_4,u}^0}{M_{\text{CH}_4}} \left(\frac{\lambda_g}{c_p} \frac{K_{\text{IV}} L e_{\text{O}_2}^3 L e_{\text{H}_2}^3}{2^5 (1 + \alpha)^3} \right)_0^{\frac{1}{2}} \frac{k_5 p k_{\text{III}}(T_0)}{q^4 X'_{\text{H}_2\text{O},0}}. \quad (6.54)$$

An expression for the variable z is found by

$$\frac{d^2 z}{d\eta^2} = \epsilon^4 Da_{\text{III}} z^3. \quad (6.55)$$

The value ϵ is chosen such that

$$\epsilon = Da_{\text{III}}^{-1/4}, \quad (6.56)$$

The upstream boundary condition can be determined from jump conditions across the inner layer. Hydrogen and carbon monoxide are already formed in the inner layer by reaction I, which causes that this reaction determines the change of slopes of the hydrogen and carbon monoxide mass fractions at the upstream boundary. Hence, integrating of equations (6.28c) and (6.28d) from $-\infty$ to the inner layer included, denoted with 0^- , results in

$$X'_{\text{H}_2}(0^-) - \frac{d}{dy} x_{\text{H}_2}(0^-) = \frac{2\beta}{1 + \beta} \frac{X'_{\text{CH}_4,u}}{\alpha} \quad (6.57a)$$

$$X'_{\text{CO}}(0^-) - \frac{d}{dy} x_{\text{CO}}(0^-) = \frac{2\beta}{1 + \beta} X'_{\text{CH}_4,u} \quad (6.57b)$$

Note that when combining equations (6.57a) and (6.57b) and dropping the *convective* term, the relation $x_{\text{CO}} = \alpha x_{\text{H}_2}$ is found as this should hold in the entire oxidation layer. Only

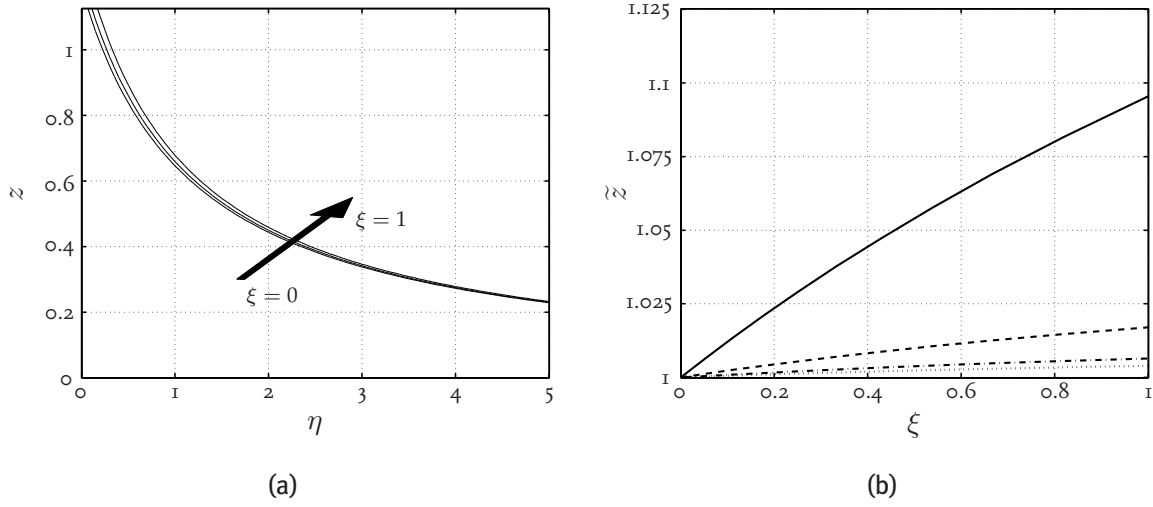


Figure 6.5: Left figure normalised hydrogen profile $z(\eta)$ in the oxidation layer. Right figure the scaling variable \tilde{z} as a function of the hydrogen content. For the positions: $\eta = 0$, solid line; $\eta = 5$, dashed line; $\eta = 15$, dashed-dotted line; $\eta = 25$, dotted line.

one of the equations (6.57a) or (6.57b) is required to determine the upstream boundary conditions for the oxidation layer. Here we take the slope of the scaled hydrogen mass fraction for the upstream edge

$$\frac{d}{dy}x_{H_2}(0^-) = -\frac{2\beta}{1+\beta} \frac{X'_{CH_4,u}}{\alpha}. \quad (6.58)$$

Combining this upstream boundary condition, the stretchings in equations (6.51), leads to

$$\left. \frac{dz}{d\eta} \right|_{\eta=0} = -\frac{(1+\alpha)\beta}{(1+\beta)\alpha} X'_{CH_4,u} \quad (6.59)$$

instead of $\frac{dz}{d\eta} = -1$, which is found by Peters and Williams. The solution

$$z(\eta) = \frac{1}{\frac{1}{z_0} + \frac{\eta}{\sqrt{2}}} \quad (6.60)$$

in the oxidation layer can now be derived and for $z_0 = z(0)$, at the edge of the inner layer, we obtain:

$$z_0 = 2^{\frac{1}{4}} \sqrt{\left(\frac{(1+\alpha)\beta}{(1+\beta)\alpha} X'_{CH_4,u} \right)}. \quad (6.61)$$

The relation of Peters and Williams is recovered for $\xi = 0$, i.e. when $\beta = \alpha$. In figure 6.5a the variable z is plotted as a function of the stretched coordinate η . Around $\eta = 0$, z is increasing with increasing hydrogen content. For $\eta \rightarrow \infty$, z decreases very slowly towards 0. This slow decrease towards $\eta = \infty$ can be explained the fact that the equilibrium situation of a flame is reached only far downstream. Furthermore, z_0 presented in equation (6.61) is increasing, this indicates that the hydrogen which is added to the

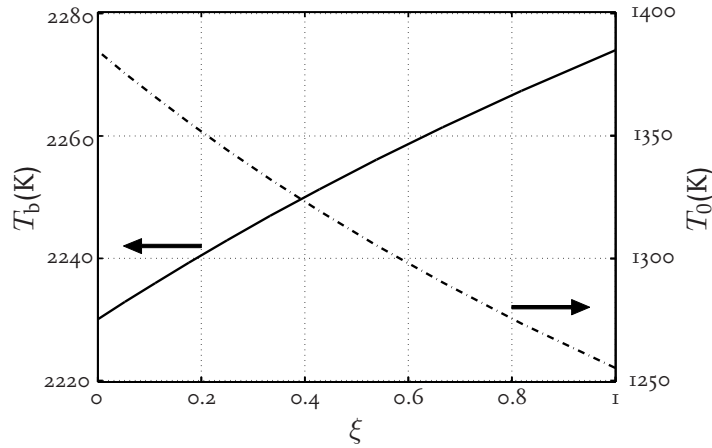


Figure 6.6: Adiabatic flame temperature T_b , —, and inner layer temperature T_0 , — —, as a function of the hydrogen content ξ .

unburnt mixture survives the inner layer, because in the inner layer more hydrogen is produced due to reaction I. This results in an increase of z at $\eta = 0$ compared to the pure methane situation. The difference between a pure methane situation $\xi = 0$ and a certain hydrogen content, e.g. $\xi = 1$ is becoming rather small further downstream. This is shown in figure 6.5b where \tilde{z} is plotted as a function of ξ for the stretched coordinate positions, $\eta = 0, 5, 15, 25$.

Inner Layer Temperature

The inner layer temperature follows from the ratio between the Damköhler numbers, equations (6.42) and (6.54), resulting in

$$\frac{Da_{III}}{Da_I} = \frac{8\delta^2}{15X_{CH_4,u}^2\epsilon^4}, \quad (6.62)$$

Inserting the Damköhler numbers equations (6.42) and (6.54), gives the following implicit equation for T_0^ξ :

$$\frac{R T_0^\xi k_1^2(T_0^\xi)}{k_{11}(T_0^\xi) k_5(T_0^\xi)} = 1.5 p \frac{Le_{CH_4}}{Le_{O_2}} \left(\frac{(1+\beta)\alpha}{(1+\alpha)\beta} \right)^2. \quad (6.63)$$

The last term in brackets is an additional factor compared to the methane-air analysis of Peters and Williams [80, 82]. However, when $\beta = \alpha$, which is a methane-air flame, then this term equals 1 and exact the same solution of Peters and Williams retrieved. In figure 6.6 the inner layer temperature is plotted as a function of ξ , T_0 is decreasing with increasing hydrogen content. The last term in equation (6.63) is the reason for this decrease. Equation (6.63) shows that with the rate coefficients fixed, the inner layer is a function of the pressure and hydrogen content only. It does not depend on the preheated unburnt gas temperature or nitrogen dilution in the mixture.

Laminar Burning Velocity

The equation for the laminar burning velocity is now found by inserting equation (6.63) in one of the equations for the Damköhler numbers. Using equation (6.42) for Da_1 we find:

$$(S_L^\xi)^2 = C A_0^\xi \left(\frac{T_u}{T_0^\xi} \right)^2 \left(\frac{T_b^\xi - T_0^\xi}{T_b^0 - T_u} \right)^2, \quad (6.64)$$

with:

$$A_0^\xi = \left(\frac{\lambda_g}{c_p} \frac{K_{IV}^{\frac{1}{2}} k_1^2}{(1 + \alpha)^{\frac{3}{2}} k_{11} X'_{H_2O}} \right)_0$$

$$C = \frac{8 Y_{CH_4,u}^0}{15 M_{CH_4}} \frac{Le_{O_2}^{\frac{5}{2}} Le_{H_2}^{\frac{3}{2}}}{Le_{CH_4} 2^{\frac{5}{2}} q^4}$$

Together with the relations given in equations (6.5), (6.21), (6.63) and the values listed in the table 6.3. This equation gives for a stoichiometric methane-air flame ($\xi = 0$) with an unburnt temperature of $T_u = 300$ K and pressure of $p = 1$ atm a (unscaled) laminar burning velocity of 54 cm/s is found. This is satisfactory in view of the many approximations that were made and the few kinetic rates that were retained [80, 82]. From equations (6.63) and (6.64) it is seen that only the reaction rates 1, 5 and 11 of the Smooke mechanism [98] influence the burning velocity in this approximation. Furthermore, the burning velocity vanishes according to equation (6.64) when inner layer temperature, T_0^ξ , reached the adiabatic flame temperature, T_b^ξ . Note that equation (6.64) gives different values for T_b^ξ when the mixture would have been preheated or diluted with nitrogen.

Flame Structure

The thickness of the inner layer and oxidation layer are analysed in this paragraph. The inner layer thickness, equation (6.43), as well as the oxidation layer thickness, equations (6.54), are strongly dependent on the inner layer temperature determined by equation (6.63). The resulting thicknesses are shown in figure 6.7a, indicating that the inner layer thickness is becoming thinner and the oxidation layer is becoming thicker with increasing hydrogen content. Note these values are relative to the total flame thickness given by equation (6.9). This flame thickness is plotted in figure 6.7b, showing that the flame is getting thinner with increasing hydrogen content. This is consistent with the findings of Göttgens [38] who determined the flame thickness for pure methane and pure hydrogen flames. The latter ones were significantly thinner compared to a pure methane one.

6.3 Results and Analysis

In this section some quantities predicted by the asymptotic theory will be compared with numerical and experimental data. The relations describing the adiabatic flame

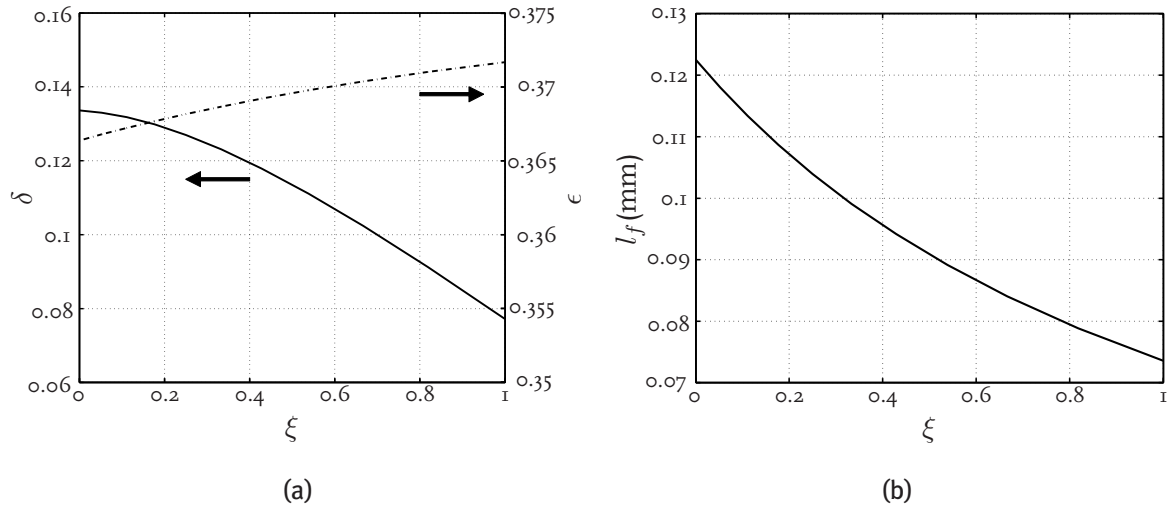


Figure 6.7: Flame structure as a function of the hydrogen fraction in the fuel ξ , the oxidation layer ϵ , solid line; and the inner layer δ , dashed dotted. Note that the preheat zone of $\mathcal{O}(1)$ is not shown. Right: flame thickness l_f as a function of ξ .

temperature, the inner layer temperature and the burning velocity, in respectively equations (6.38), (6.63) and (6.64) are used for that end. The predicted behaviour for the temperature variables will be compared with numerical results, while the predicted change in burning velocity is also compared with experiments.

Table 6.1: The applied Lewis numbers and reaction rates [80].

Species	Le_i	Reaction	A	b	$E_j = E_a/R$
CH ₄	0.97	k_1	2.00×10^{14}	0	8400
H ₂	0.30	k_5	2.30×10^{18}	-0.8	0
O ₂	1.11	k_{11}	2.20×10^4	3	4400
CO	1.10	K_{II}	0.035	0	3652
		K_{IV}	1.48	0	3652

Adiabatic Flame Temperature

The change in adiabatic flame temperature is found from equation (6.38). Using that $q_{H_2} = 0.3116$ and $X_{CH_4,u} = 1/(1+\xi/4)$, this equation indicates that τ increases slowly with $\approx 1+0.061\xi$ for relatively small ξ values. The change in T_b^ξ , as predicted by equation (6.38) is presented in figure 6.8 as function of ξ , together with results from detailed numerical simulations using the GRI 3.0 mechanism. Close to $\xi = 0$ the relative change e_b in T_b^ξ following from equation (6.38) can be expressed as $e_b = (T_b^\xi - T_b^0)/T_b^0 \approx 0.028\xi$ whereas the GRI 3.0 mechanism gives $e_b = 0.019\xi$. This slight overestimate of equation (6.38) is related to the inaccuracy in the asymptotic model related to the treatment of the equilibrium state.

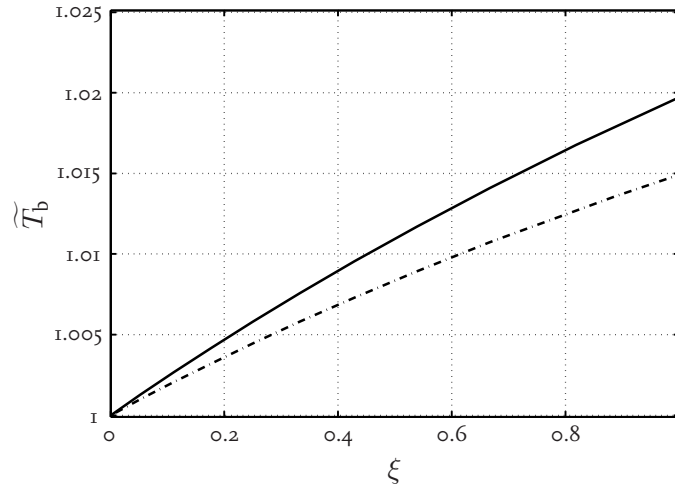


Figure 6.8: Adiabatic flame temperature, \widetilde{T}_b , as a function of the hydrogen content, ξ . Asymptotic theory equation (6.38), —; GRI 3.0 mechanism [97], - -.

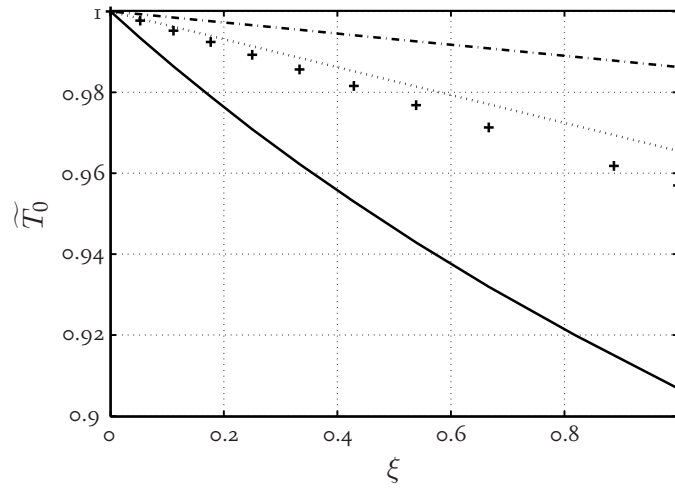


Figure 6.9: Scaled inner layer temperature, \widetilde{T}_0 , as a function of the hydrogen content, ξ . Analysis equation (6.63), —; Geometric, +; temperature at the position of the maximum CO mole fraction, - ·; temperature at the position of the maximum heat release, · · ·.

Inner Layer Temperature

Theoretically, equation (6.63) predicts the change in the inner layer temperature T_0^ξ . This result is plotted in figure 6.9 as function of ξ , using the temperature dependence of the reaction rates k_1 , k_{11} and k_5 (see table 6.3) in equation (6.63) at a pressure of $p = 1$ atm. It should be realised that there are several definitions in use for the inner layer. Beside equation (6.63), the position of the maximum heat release, the maximum temperature gradient (geometric definition introduced by Göttgens [38]) and the position of the maximum mole fraction of CO are alternatives, sometimes used in numerical studies. Numerical results for these different definitions are also presented in figure 6.9. The observed decrease of T_0^ξ as a function of ξ can be explained by the increase of the oxidation layer thickness due to the increasing amount of H_2 and CO to be oxidised in the

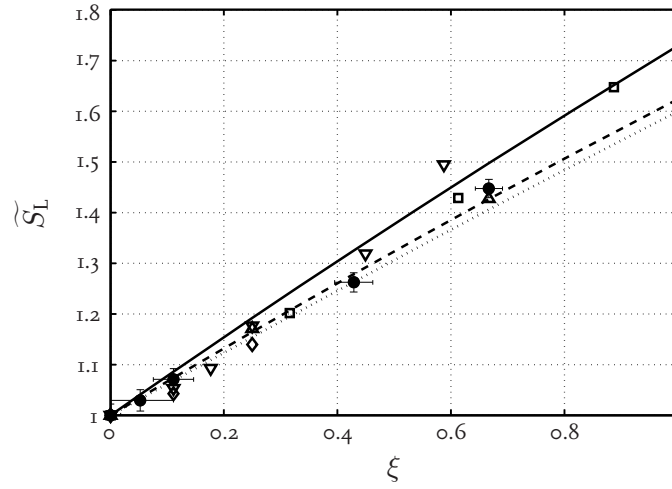


Figure 6.10: Scaled laminar burning velocity, \widetilde{S}_L , as a function of the hydrogen content, ξ . \widetilde{S}_L determined with equation (6.64), solid line; Smooke [98], dotted line; GRI 3.0 mech [97], dashed line; and the symbols: heat flux measurements, \circ ; Huang [52], \triangle ; Halter [42], \diamond ; Yu [116], \square ; Haniff [43], ∇ .

oxidation layer. If we write $T_0^\xi = T_0^0(1 + e_0)$, insert this into equation (6.63) and expand around $e_0 = 0$ this gives for the relative change e_0 in T_0^ξ close to $\xi = 0$: $e_0 \approx -0.12\xi$. In spite of the large differences in T_0^0 , the behaviour of e_0 as function of ξ , of all definitions in Figure 6.9 is quite similar: from the geometric definition we find $e_0 \approx -0.087\xi$, the maximum CO mole fraction gives $e_0 \approx -0.015\xi$ and for the maximum heat release we find $e_0 \approx -0.048\xi$.

Burning Velocity

In order to use equation (6.64) for evaluating the change in burning velocity, the change in α_0 and the water fraction $X_{\text{H}_2\text{O},0}$ at the interface between the inner layer and the oxidation layer have to be known. $X_{\text{H}_2\text{O},0}$ and $X_{\text{CO}_2,0}$ can be determined by integrating equations (6.28)a,e,f over the inner layer giving $X_{\text{H}_2\text{O},0} = X_{\text{CH}_4,u} 2\beta/(1 + \beta)$ and $X_{\text{CO}_2,0} = X_{\text{CH}_4,u} (1 - \beta)/(1 + \beta)$. On the other hand, the relation between β and α is given by equation (6.33), while α depends on the mole fractions of CO_2 and H_2 again: $\alpha = X_{\text{CO}_2} Le_{\text{O}_2}/(X_{\text{H}_2\text{O}} K_{\text{II}}(T) Le_{\text{CO}})$. This is a coupled system which can be solved iteratively. Both α_0 and $X_{\text{H}_2\text{O},0}$ change significantly as a function of ξ . From the analysis we find $1 - 0.38\xi$ for the relative change in $X_{\text{H}_2\text{O},0}$ and $1 - 0.23\xi$ for the relative change in $(1 + \alpha_0)$. It is not possible to neglect this change in the evaluation of the burning velocity. As a last step, we combine all the changes (e.g. e_0 , e_b , $1 + \alpha_0$ and $X_{\text{H}_2\text{O},0}$) to derive the change in the burning velocity as a function of ξ . If also use is made of the temperature dependence of K_{IV} (see table 6.3) and $\frac{\lambda(T)}{c_p(T)} \propto T^{0.7}$ this gives for the change in \widetilde{S}_L :

$$\left(\frac{\widetilde{S}_L^\xi}{\widetilde{S}_L^0}\right)^2 = \frac{A^\xi}{A^0} \left(\frac{T_0^0}{T_0^\xi}\right)^2 \left(\frac{T_b^\xi - T_0^\xi}{T_b^0 - T_0^0}\right)^4, \quad (6.65)$$

The obtained result of equation (6.65) is presented in figure 6.10, together with the numerical and experimental results for \widetilde{S}_L . We used $T_0^0 = 1384$ K and close to $\xi = 0$ the

asymptotic theory gives $\widetilde{S}_L \approx (1 + 0.80\xi)$. The theory predicts a slightly stronger increase in the burning velocity. The relatively strong change in the inner layer temperature T_0^ξ is the dominant factor governing the increase of the laminar burning velocity. The most sensitive part in equation (6.65) is the factor $(T_b^\xi - T_0^\xi)^4 / (T_b^0 - T_0^0)^4$. It is interesting to note though that the temperature difference $(T_b^\xi - T_0^\xi)$ in this factor is related to the effective activation energy of the reacting system.

6.4 Discussion

The theory for methane-hydrogen-air flames which is presented in this thesis is used for hydrogen contents up to 50 mol% ($\xi = 1$). A question concerning the working range of the theory remains to be answered. It is clear that the theory is not valid anymore for hydrogen-air mixtures. Simulations with complete kinetic mechanisms shown in the previous chapter reveal the dominating mechanism of methane-hydrogen-air flames, e.g. figure 5.8 and figure 5.9. Clearly visible in these figure is that above 70% of hydrogen in the fuel mixture laminar burning velocity increases non-linear. It is expected that for higher hydrogen contents the influence of the hydrogen mechanism becomes more pronounced and this is expected to be approximately the upper limit of the methane-hydrogen-air asymptotic theory.

The asymptotic theory presented in this thesis is based on the work presented by Peters in the Ercoftac lecture notes [80]. It turned out that later extensions of the theory used other reaction rates as the ones listed in table 6.3. When applying these modified reaction rates in the present theory the resulting scaled properties like the burning velocity and inner layer temperature do not change. However, the unscaled burning velocity for the pure methane situation ($\xi = 0$) increases from 54 to 86 cm/s. Both laminar burning velocities values are large in comparison to the measured and calculated values using kinetic mechanisms; which is ≈ 36 cm/s for stoichiometric methane-air flames. This overprediction of the laminar burning velocity can be improved by not taking the the water-gas shift reaction into equilibrium. This is presented by Peters and Williams [82] who showed that water is usually less than which would be predicted by the water-gas shift reaction and carbon monoxide is greater. Thus, assuming the water-gas shift reaction infinitely fast overestimates the amount of hydrogen produced in the inner layer. Because of the strong dependence of the Da_I on X_{H_2O} the influence on the results calculated here is expected to be important.

6.5 Conclusions

The asymptotic theory for stoichiometric methane-air flames presented by Peters and Williams has been successfully adapted and applied for stoichiometric methane-hydrogen-air flames. The theory predicts a slow increase in T_b^ξ if hydrogen is present in the fuel, which is supported by numerical results. Furthermore, a decrease in inner layer temperature T_0^ξ is predicted in agreement with numerical data. This change dominates

the change in burning velocity. However, the absolute value of T_0^ξ and the exact slope as predicted by the theory as function of ξ is more difficult to compare to numerical results. The theory predicts a slightly larger increase in the burning velocity than experiments and numerical simulations indicate. The analysis of presented in this chapter explains the influence of hydrogen on the basic flame structure of methane-hydrogen-air flames changes in comparison with the flame structure of premixed methane-air flames. This physical insight is important to guide the development of combustion systems in which mixtures of natural gas with hydrogen are used.

Concluding Remarks

The laminar adiabatic burning velocity S_L of a gaseous fuel-oxidiser mixture is a key parameter governing many properties of combustion. In this thesis the laminar burning velocity of methane-hydrogen-air mixtures is investigated experimentally using the heat flux method. The measured laminar burning velocities with 95% confidence error intervals of stoichiometric methane-hydrogen-air flames increases with increasing hydrogen content; from 36.4 ± 0.1 cm/s (at $\mathcal{R}_{H_2} = 0\%$) to 39.2 ± 0.03 cm/s (at $\mathcal{R}_{H_2} = 10\%$), 42.3 ± 0.02 cm/s (at $\mathcal{R}_{H_2} = 20\%$), 47.0 ± 0.02 cm/s (at $\mathcal{R}_{H_2} = 30\%$) and 53.5 ± 0.02 cm/s (at $\mathcal{R}_{H_2} = 40\%$). The typical uncertainty in the burning velocity is ± 0.02 cm/s for stoichiometric flames, and increases up to 1.0 cm/s for flames with low burning velocities (e.g. $\phi < 0.7$ and $\phi > 1.4$). Comparison with literature shows that the burning velocities of methane-air mixtures, measured using the heat flux method are consistent with recent results measured by other techniques such as the counterflow method and spherical bomb method.

A possible effect that the burner plate is acting as a catalyst has been investigated experimentally as well as numerically. This effect could influence the measurement of the laminar burning velocity when using the heat flux method. However, it turned out that the laminar burning velocity results are not notably influenced by the burner plate for the investigated parameter range. Although it is expected that when using the heat flux method with unburnt gas temperatures relevant for gas turbine conditions this effect of a burner plate which is acting as catalyst is becoming larger.

The investigation regarding laminar burning velocities presented in this thesis can be subdivided into three parts. The first part consists of laminar burning velocities of hydrogen-oxygen-nitrogen mixtures at ambient conditions. The second part describes the laminar burning velocities of methane-hydrogen-air mixtures also at ambient conditions whereas the last part describes the laminar burning velocities of methane-hydrogen-air mixtures at increased unburnt gas temperatures. The most important aspects and results of each of these subjects is summarised below.

Three sets of measurements have been performed and presented in chapter 4. The first set of measurements dealing with hydrogen-oxygen-nitrogen flames, highly diluted with

nitrogen, shows significant differences between heat flux data and experimental results of Egolfopoulos and Law. [26]. This discrepancy is considered as belonging to the non-linear stretch correction performed by Egolfopoulos and Law. The differences between the combustion reaction mechanisms and the heat flux data shows significant differences in the performance of the methane based combustion reaction mechanisms. Especially the commonly used GRI-mechanism [97] deviates from the experimental data. The SKGo₃ mechanism [96] performs quite well for a fairly large part of the measurement range. The performance of this mechanism is even comparable or even better compared to hydrogen based mechanisms for fuel lean flames to slightly fuel rich hydrogen-oxygen-nitrogen flames. Generally, the hydrogen based kinetic mechanisms perform quite well for the investigated parameter range; especially the Konnov mechanism [61].

The second set of measurements of methane-hydrogen-air mixtures at ambient conditions shows that the laminar burning velocity measurements of Halter et al [42] show comparable results with the present heat flux data. The results of other researchers show significant differences compared to the present data; again this can be considered as belonging to the non-linear stretch correction applied by these researchers. Comparing the measured laminar burning velocities with numerical data using several kinetic mechanisms shows comparable results for the investigated parameter range. The SKGo₃ mechanism [96] performs very well for these investigated methane-hydrogen-air mixtures. The commonly used GRI-mechanism [97] gives also good results although it deviates slightly from the measurements with increasing hydrogen contents.

When comparing the final set of measurements of the laminar burning velocity of pre-heated methane-hydrogen-air mixtures with numerical combustion mechanisms give similar results as for methane-hydrogen-air mixtures at ambient condition; both the SKGo₃ mechanism [96] and the GRI-mechanism [97] perform very well. Experimental data of the laminar burning velocity of methane-hydrogen-air flames is scarce. However, in the case of methane-air flames the measurements of Bosschaart [7] show comparable results with the present measurements. Generally the laminar burning velocity is increasing with approximately $0.25 \text{ cm s}^{-1} \text{ K}^{-1}$ and is slightly larger for hydrogen enhanced methane-air mixtures.

An expression describing the influence of the added hydrogen on the burning velocity can be useful as a design tool for analysing the behaviour of combustion equipment in the transition phase to a hydrogen economy. A correlation proposed by Coppens et al. [17] that covers the complete data set of burning velocities of methane-hydrogen-air flames with varying equivalence ratio is used in this thesis. The present heat flux results of methane-hydrogen-air flames have been successfully fitted to this correlation and the fit parameters differ only slightly from the values determined by Coppens et al. [17]. In the case of methane-hydrogen-air flames at increased unburnt gas temperature the heat flux results have been fitted to the correlation proposed by Metghalchi and Keck [76]. The temperature coefficient determined from the present measurements is comparable with the results from the combustion reaction mechanisms.

In order to get more insight in the basic properties which describe methane-hydrogen-air flames, the asymptotic theory of Peters and Williams [82] for stoichiometric methane-air flames is extended to stoichiometric methane-hydrogen-air flames. The present theory is able to describe the structure of stoichiometric methane-hydrogen-air flames. The theory

predicts a decreasing inner layer temperature, while the adiabatic flame temperature increases slightly with increasing amount of hydrogen in the fuel. These changes together lead to an increasing burning velocity as function of the amount of hydrogen in the fuel mixture. The predicted variations are compared with numerical results and the burning velocity is also compared with experiments and the agreement is reasonable. The derived analytical expressions can be used to guide the adaption of combustion systems running on natural gas when hydrogen is added to the fuel.

Combustion Reaction Mechanism

This appendix presents the Smooke combustion reaction mechanism [98] that is used in chapter 6 as a starting point for the asymptotic theory. In table A.1 this Smooke methane-air reaction mechanism is listed with the reaction constants. These reaction constants are used in the equations related to the chemical source term (section 2.1.3). The speed of a reaction is determined by the reaction constants A , E_a and b .

Enhanced Coefficients

In table A.1 some reactions require a third molecule, which does not react by itself, but is essential for the reaction to proceed, e.g.



The concentration of the effective third body species M must appear in the expression for the reaction rate variable. Accordingly, the reaction rate for third body reactions is slightly different from equation (2.21) by the first factor in the equation below:

$$r_j = \left(\sum_{i=1}^{N_s} \varsigma_{ij} n_i \right) \left(k_{j,f} \prod_{i=1}^{N_s} n_i^{\nu'_{ij}} - k_{j,b} \prod_{i=1}^{N_s} n_i^{\nu''_{ij}} \right), \quad (\text{A.2})$$

with ς_{ij} the so-called enhanced coefficient or collision efficiency for species i and reaction j . If all species in the mixture contribute equally as third bodies then all the $\varsigma_{ij} = 1$ and the first factor is the total concentration of the mixture. However, it is often the case that some species act more efficiently as third body species than others do. The ς_{ij} coefficients are then used to specify the increased efficiency of the i^{th} species in the j^{th} reaction. Also, if a species is to be excluded from acting as a third body species in a particular reaction then $\varsigma_{ij} = 0$ for that species. For the listed combustion reaction mechanisms in table A.1 the collision efficiencies are given by, $\varsigma_{\text{CH}_4} = 6.5$, $\varsigma_{\text{H}_2\text{O}} = 6.5$, $\varsigma_{\text{CO}_2} = 1.5$, $\varsigma_{\text{H}_2} = 1.0$, $\varsigma_{\text{CO}} = 0.75$, $\varsigma_{\text{N}_2} = 0.4$ and $\varsigma_{\text{O}_2} = 0.4$. All other species the collision efficiency equals 1.0.

Table A.1: Rate data for reactions employed in the asymptotic analysis.

Rate No.	Reaction	A	b	E_a
1	$\text{H} + \text{O}_2 \rightleftharpoons \text{OH} + \text{O}$	2.00×10^{14}	0.0	16800.0
2	$\text{O} + \text{H}_2 \rightleftharpoons \text{OH} + \text{H}$	1.80×10^{10}	1.0	8826.0
3	$\text{H}_2 + \text{OH} \rightleftharpoons \text{H}_2\text{O} + \text{H}$	1.17×10^9	1.3	3626.0
4	$\text{OH} + \text{OH} \rightleftharpoons \text{O} + \text{H}_2\text{O}$	6.00×10^8	1.3	0.0
5	$\text{H} + \text{O}_2 + \text{M} \rightleftharpoons \text{HO}_2 + \text{M}$	2.30×10^{18}	-0.8	0.0
6	$\text{H} + \text{HO}_2 \rightleftharpoons \text{OH} + \text{OH}$	1.50×10^{14}	0.0	1004.0
7	$\text{H} + \text{HO}_2 \rightleftharpoons \text{H}_2 + \text{O}_2$	2.50×10^{13}	0.0	700.0
8	$\text{OH} + \text{HO}_2 \rightleftharpoons \text{H}_2\text{O} + \text{O}_2$	2.00×10^{13}	0.0	1000.0
9	$\text{CO} + \text{OH} \rightleftharpoons \text{CO}_2 + \text{H}$	1.51×10^7	1.3	-758.0
10	$\text{CH}_4 + \text{M} \rightleftharpoons \text{CH}_3 + \text{H} + \text{M}$	2.30×10^{38}	-7.0	114360.0
11	$\text{CH}_4 + \text{H} \rightleftharpoons \text{CH}_3 + \text{H}_2$	2.20×10^4	3.0	8750.0
12	$\text{CH}_4 + \text{OH} \rightleftharpoons \text{CH}_3 + \text{H}_2\text{O}$	1.60×10^6	2.1	2460.0
13	$\text{CH}_3 + \text{O} \rightleftharpoons \text{CH}_2\text{O} + \text{H}$	6.80×10^{13}	0.0	0.0
14	$\text{CH}_2\text{O} + \text{H} \rightleftharpoons \text{HCO} + \text{H}_2$	2.50×10^{13}	0.0	3991.0
15	$\text{CH}_2\text{O} + \text{OH} \rightleftharpoons \text{HCO} + \text{H}_2\text{O}$	3.00×10^{13}	0.0	1195.0
16	$\text{HCO} + \text{H} \rightleftharpoons \text{CO} + \text{H}_2$	4.00×10^{13}	0.0	0.0
17	$\text{HCO} + \text{M} \rightleftharpoons \text{CO} + \text{H} + \text{M}$	1.60×10^{14}	0.0	14700.0
18	$\text{CH}_3 + \text{O}_2 \rightleftharpoons \text{CH}_3\text{O} + \text{O}$	7.00×10^{12}	0.0	25652.0
19	$\text{CH}_3\text{O} + \text{H} \rightleftharpoons \text{CH}_2\text{O} + \text{H}_2$	2.00×10^{13}	0.0	0.0
20	$\text{CH}_3\text{O} + \text{M} \rightleftharpoons \text{CH}_2\text{O} + \text{H} + \text{M}$	2.40×10^{13}	0.0	28812.0
21	$\text{HO}_2 + \text{HO}_2 \rightleftharpoons \text{H}_2\text{O}_2 + \text{O}_2$	2.00×10^{12}	0.0	0.0
22	$\text{H}_2\text{O}_2 + \text{M} \rightleftharpoons \text{OH} + \text{OH} + \text{M}$	1.30×10^{17}	0.0	45500.0
23	$\text{H}_2\text{O}_2 + \text{OH} \rightleftharpoons \text{H}_2\text{O} + \text{HO}_2$	1.00×10^{13}	0.0	1800.0
24	$\text{OH} + \text{H} + \text{M} \rightleftharpoons \text{H}_2\text{O} + \text{M}$	2.20×10^{22}	-2.0	0.0
25	$\text{H} + \text{H} + \text{M} \rightleftharpoons \text{H}_2 + \text{M}$	1.80×10^{18}	-1.0	0.0

Gas Flow Control

In this appendix two topics will be addressed both related to the gas flow control. The first topic describes briefly how the MFC setpoints are calculated. The second topic governs the calibration of the mass flow controllers.

B.1 Mass Flow Controller Setpoints

The gas mixture which is supplied to the heat flux burner is regulated by Mass Flow Controllers of Bronkhorst Hi-Tec [50]. In chapter 3, the crucial parameter is the laminar adiabatic burning velocity. This is determined by varying the gas velocity delivered by mass flow controllers (MFCs) at a certain equivalence ratio, temperature, pressure and gas mixture composition. A general description for the resulting settings for the mass flow controllers is presented in this section. The equivalence ratio ϕ is defined as

$$\phi = \nu_m \frac{\dot{m}_{fu}}{f_{O_2} \dot{m}_{ox}}, \quad (B.1)$$

where f_{O_2} is the mass fraction of oxygen in air and ν_m the (mass based) stoichiometric coefficient. By rewriting this equation and combining with the ideal gaslaw, the gas flow is given by

$$U_g = \frac{R_0 T_u}{p_u A} \left(\frac{\dot{m}_{fu}}{M_{fu}} + \frac{\dot{m}_{ox}}{M_{ox}} \right). \quad (B.2)$$

The conversion to normal litres per minute takes place in order to be able to calculate the correct setpoint of a Mass flow Controller, which has a maximum flow $Q_{\max,i}$ defined in nl/min,

$$Q_i = \frac{\dot{m}_i}{\rho_i} \cdot 60 \cdot 1000, \quad (B.3)$$

where ρ_i is the mass density of component i . And the setpoint of every component is defined as:

$$Sp_i = \frac{Q_i}{Q_{\max,i}} \cdot 100\% \quad (B.4)$$

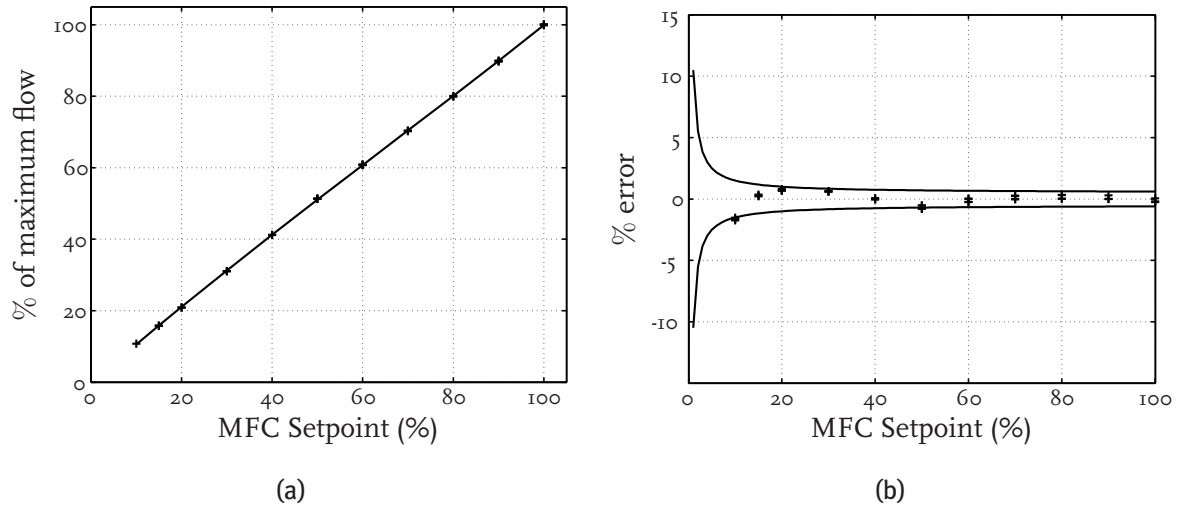


Figure B.1: Mass flow controller calibration curves. Left MFC setpoint as a function of the measured flow with the calibration setup. In the right figure the error estimate as a function of the MFC setpoint.

These relations for the setpoints are derived for a perfect mass flow controller. However, non-linear effects occur in the devices and electronic circuits. By calibrating the mass flow controllers and using a third order polynomial we correct the calculated setpoints for these non-linear effects. This procedure will be shown in the next section.

B.2 Mass Flow Controller Calibration

According to the manufacturer the mass flow controllers need to be calibrated on a regular basis to provide accurate mass flows. The calibration setup and procedure described by Bosschaart [7] is used resulting in a brief description here. The only difference compared to the Bosschaart is the resulting uncertainty factor determined for every mass flow controller. The calibration data are fitted to a third order polynomial curve. An example measurement is shown in figure B.1a. In this figure the symbols denote the calibration measurements and the lines the fit. Hence, the data are very close to the fit. The residuals are plotted in figure B.1b. These residuals can be used as an indication of the uncertainty estimate of a mass flow controller. According to Bronkhorst High-tech [49] when using a polynomial fit after calibration of the mass flow controller the uncertainty is defined as

$$\Delta \dot{m} = 0.5\% \text{off Reading} + 0.1\% \text{Full Scale.} \quad (\text{B.5})$$

In this thesis this relation is used to determine the uncertainty of a mass flow controller. This is the only difference compared to Bosschaart [7] who used a constant value of 0.5% Full scale as an uncertainty estimate. Moreover, the third order polynomial fit is used to correct the determined setpoints in equation (B.4) in order to reduce the non-linear effects occurring in the devices.

Background of the Heat Flux Method

In chapter 3 the basic principle of the heat flux method is explained. In this appendix an additional (physical) background of the heat flux method is presented. This background is based on an analysis of de Goey et al. [35]. The main idea of the heat flux method is that the heat fluxes from the flame to burner equal the heat fluxes from the burner to the unburnt gas in the case of an adiabatic flat flame. The burning velocity corresponding to this situation equals the laminar adiabatic burning velocity. In this appendix the energy equations of both freely propagating flames and burner stabilised flames are analysed and show in the end that an adiabatic flame can be stabilised on the heat flux burner. In the first section of this appendix, the energy equation of freely propagating flames is used to describe the laminar adiabatic burning velocity. In the second section the energy equations of burner stabilised flames are analysed showing that the burning velocity of a flame which is stabilised on the heat flux burner equals the laminar adiabatic burning velocity.

C.1 Freely Propagating Flames

A useful start is analysing the energy equation of freely propagating flat flames. The energy equation (see also chapter 2), of an adiabatic flat (1D) flame can be written as,

$$\dot{m}c_p \frac{\partial T_g}{\partial x} - \frac{\partial}{\partial x} \left(\lambda_g \frac{\partial T_g}{\partial x} \right) = \dot{\omega}_T, \quad \text{with} \quad \dot{\omega}_T = - \sum_{i=1}^{N_s} h_i \dot{\omega}_i, \quad (\text{C.1})$$

where \dot{m} is the constant mass flux, T_g the temperature of the gas, c_p the specific heat at constant pressure, λ_g the thermal conductivity of the gas and $\dot{\omega}_T$ the heat source term of the reactions taking place. The preheating zone of a flame is defined in the region $-\infty < x < x_c$. In this preheating zone $\dot{\omega}_T$ is assumed to be zero. Integrating equation (C.1) from $x = -\infty$ to a point $x < x_c$, and taking into account that $\frac{\partial T_g}{\partial x} = 0$ for $x = -\infty$, gives

$$\lambda_g \frac{\partial T_g(x)}{\partial x} = \dot{m}c_p (T_g(x) - T_u), \quad (\text{C.2})$$

with the unburnt gas temperature $T_u = T_g(-\infty)$. When using $\dot{m} = \rho U_g = \rho S_L$ in equation (C.2) a general expression for the laminar burning velocity S_L is found

$$S_L = \frac{\lambda_g}{\rho c_p (T_g(x_c) - T_u)} \left. \frac{\partial T_g}{\partial x} \right|_{x=x_c}. \quad (\text{C.3})$$

The derivative $\frac{\partial T_g}{\partial x}$ at $x = x_c$ can be determined exactly when $\dot{\omega}_T$ is known. However, the exact value of the temperature gradient is not needed in the present analysis. The derivative is uniquely defined by the energy equation (C.1) in the reaction zone, $x > x_c$. Its value can be determined when applying the boundary conditions for the energy equation in the reaction zone $T_g = T_c$ at $x = x_c$ and $T_g = T_{ad}$ at $x = +\infty$. Note that T_{ad} is the adiabatic flame temperature. In the remaining part of this section the stabilising mechanism of flames is explained by using this temperature gradient.

C.1.1 Stabilising Mechanism

Conduction of heat from the flame to the burner is the main stabilising mechanism of flames on conventional burners. This implies that $\frac{\partial T_g}{\partial x} > 0$ at $x = x_p$, where x_p is the top of the burner plate in streamwise direction. These flames are *only* adiabatic when they blow-off, which means that $\frac{\partial T_g}{\partial x} = 0$ at $x = x_p$. In practical situations however, it appears that blow-off occurs even before the adiabatic propagation velocity is reached. This might be due to, for example, disturbances of the surrounding atmosphere, or irregularities in the burner plate. In the case of the heat flux burner the situation of early blow-off is avoided by preheating the burner plate. An external heating jacket keeps the burner plate edge at a constant temperature T_R which is ≈ 60 K higher than the unburnt gas temperature T_u . T_R is chosen such, that $T_u < T_R < T_g(x_c)$ ¹. Now, the unburnt gas is heated by the burner plate. The flame will not blow off, but remains flat and stabilises on the burner by losing heat to the burner plate. In the adiabatic case when $U_g = S_L$ the heat loss of the flame is equal to the heat gain of the unburnt gases by the burner plate. Consequently the radial temperature gradient in the burner plate can be neglected. Since the heat fluxes to and from the burner are now equal and non-zero, the flame is not only stable because of $\frac{\partial T_g}{\partial x} > 0$ at $x = x_p$, but also adiabatic because the energy is preserved over the burner plate. As long as T_R is high enough to prevent partial blow-off, the actual value of T_R is not important once the adiabatic state is established. Concluding, by heating the burner edge T_R above the unburnt gas temperature T_u the flame is in fact an adiabatic burner stabilised flame.

C.2 Adiabatic Burner Stabilised Flames

The temperature profiles of an adiabatic free flame and a flame which is stabilised on the heat flux burner is shown schematically in figure C.1. The burner plate ranges from $x = 0$ to $x = x_p$ with a temperature profile T_p in axial direction. Now the question arises how the physical properties of an adiabatic burner stabilised flame (e.g. temperature and

¹. In conventional burners T_R is almost equal to T_u for $U_g \approx S_L$.

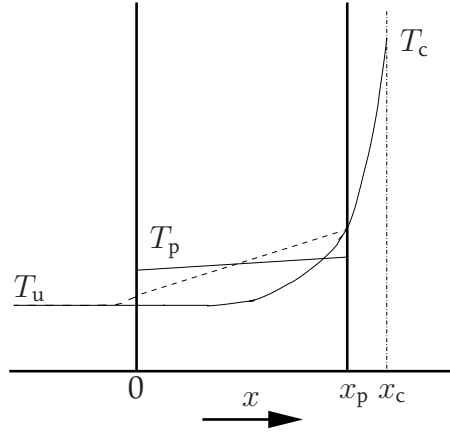


Figure C.1: Temperature profile of a free adiabatic flame (solid line) compared to the temperature profile of a flame stabilised on the burner plate (dashed line). T_p indicates the temperature of the burner plate.

mass-fraction profiles, burning velocity) compare with those of a freely propagating flat flame. Again, the energy equations of the adiabatic burner-flame system are considered to determine this problem. Assuming that the burnerplate of the heat flux burner, see figure 3.4b, can be approximated in a 1D situation by averaging the holes and plate material in radial direction, the 1D energy equation of the open parts in the burner plate, which is in fact the gas, can be written as:

$$\chi_g \rho \left(\frac{U_g}{\chi_g} \right) c_p \frac{\partial T_g}{\partial x} - \frac{\partial}{\partial x} \left(\lambda_g \chi_g \frac{\partial T_g}{\partial x} \right) = \dot{\omega}_T + \alpha (T_p - T_g). \quad (\text{C.4})$$

In this equation, α is the heat transfer coefficient between the gas and the plate within the perforations and χ_g the porosity of the gas inside the burner plate. Conservation of energy within the burner plate material, with thermal heat conductivity λ_p leads to the following equation for the axial temperature profile $T_p(x)$ of the burner plate,

$$-\frac{\partial}{\partial x} \left(\lambda_p \chi_p \frac{\partial T_p}{\partial x} \right) = -\alpha (T_p - T_g). \quad (\text{C.5})$$

Note that the sum of the porosity's must sum up to one, $\chi_g + \chi_p = 1$. Moreover for $x > x_p$ and $x < 0$, $\alpha = 0$ and $\chi_g = 1$. Furthermore, the flames analysed here are assumed to be adiabatic and 1D, and stabilised on a burner. Hence, all heat transport terms in radial direction can be omitted in equations (C.4) and (C.5). Therefore when integrating the left-hand side of equation (C.5) from $x = 0$ to $x = x_p$ should be zero for an adiabatic flame. Consequently, when equations (C.4) and (C.5) are added and integrated from $x = -\infty$ to a point $x_p < x < x_c$, the relations of the freely propagating flame in equations (C.2) and (C.3) are retrieved again. The boundary conditions $T_g(x_c) = T_c$ and $T_g(\infty) = T_{ad}$ are also unchanged, meaning that the temperature profile $T_g(x)$ for $x > x_p$ and the burning velocity are equivalent to the corresponding properties of a free adiabatic flame.

Temperature of the Burnerplate

In this appendix two topics will be addressed, both related to the temperature of the burnerplate. The first topic describes the influence of the temperature dependence of the heat conductivity term on the burner plate temperature. The second gives an overview of the axial temperature variation in the burner plate. The final relation gives insight in the systematic error of the thermocouple measurements in the burner plate.

D.1 Temperature Dependency of the Heat Conductivity

In this section a relation is derived for the average plate temperature with a temperature dependent heat conductivity. The derivation starts with the 1D energy of the burner plate:

$$-\frac{1}{r} \frac{d}{dr} \left(\lambda_{p,r}(r) r \frac{d}{dr} \bar{T}_p(r) \right) = \frac{q(r)}{h}. \quad (\text{D.1})$$

This equation can be solved with proper boundary conditions (as is shown in chapter 3) resulting in

$$\bar{T}_p(r) = T_c \left(1 + C r^2 \right), \quad \text{with} \quad C = -\frac{q}{4\lambda_{p,r} h T_c} \quad (\text{D.2})$$

indicating that the average temperature distribution in the burner plate appears to be a parabola, with the centre of the burner plate as the symmetry axis. However, this relation uses a temperature independent heat conduction term, $\lambda_{p,r}$. A similar relation for the burner deck temperature can be retrieved by taking a temperature dependent heat conduction term. For example van Maaren [72] used a linear function of the temperature for the heat conductivity of brass, which is based on experimental data:

$$\lambda_{br}(T) = a + b \cdot T, \quad (\text{D.3})$$

with the constants $a = 73.1 \text{ W m}^{-1} \text{ K}^{-1}$ and $b = 0.160 \text{ W m}^{-1} \text{ K}^{-2}$. This is the heat conductivity in the case of a solid brass plate, in the case of a heat flux burner system small

holes and a certain perforation pattern are used, the heat conductivity now becomes,

$$\lambda_{p,r}(T) = \epsilon \cdot \lambda_{br}(T), \quad (D.4)$$

where $\epsilon = 0.362$ as has been determined numerically by Sonnemans [101] and experimentally confirmed by van Maaren [72]. The plate temperature with a temperature dependent heat conductivity of the brass plate can be solved by using equations (D.1), (D.3) and (D.4). An analytical solution for plate temperature can be retrieved by integrating equation (D.1), and using the boundary condition $T_p(r = 0) = T_c$:

$$\bar{T}_p(r) = -\frac{a}{b} + \sqrt{\left(\frac{a}{b} + T_c\right)^2 - \frac{r^2 q}{2\epsilon b h}}. \quad (D.5)$$

D.2 Axial Temperature Dependency

Van Maaren [72] showed that the axial temperature variations inside the plate, $\mathcal{O}(1)$ K, are negligible small compared to the radial temperature variations, $\mathcal{O}(20)$ K. Therefore, the resulting plate temperature T_p will have only small errors due to these variations. However, Bosschaart [7] divided these fluctuations in a systematic error and a random error. In order to gain insight in the physical background of the systematic differences found in the temperature profiles shown in figure 3.7a the 2D energy equation will be solved. Since most of the heat transfer takes place from the flame to the top of the burner plate by conduction, the heat transfer inside the burner plate is neglected. Now the 2D energy equation can be approximated with a 2D conduction equation given by

$$\frac{1}{\epsilon} \frac{\partial^2}{\partial x^2} T_p(x, r) + \frac{1}{r} \frac{\partial}{\partial r} T_p(x, r) + \frac{\partial^2}{\partial r^2} T_p(x, r) = 0. \quad (D.6)$$

where T_p is the plate temperature and ϵ defined is as:

$$\epsilon = \frac{\lambda_{p,r}}{\lambda_{br}} \quad (D.7)$$

To be able to solve the 2D conduction equation the temperature $T_p(x, r)$ is separated into two functions $T_p(x, r) = Y(x)S(r)$ which only depend on one variable. Together with equation (D.6) and subsequent separating and introducing the constant α^2 , gives

$$r^2 \frac{d^2}{dr^2} S(r) + r \frac{d}{dr} S(r) + \alpha^2 r^2 S(r) = 0, \quad (D.8)$$

$$\frac{d^2}{dx^2} Y(x) = \epsilon \alpha^2 Y(x). \quad (D.9)$$

Equation (D.8) is a special form of the Bessel equation and its solution yields

$$S(r) = c_1 J_0(\alpha r) + c_2 Y_0(\alpha r), \quad (D.10)$$

with the Bessel function of the first kind J_0 and second kind Y_0 . From symmetry boundary conditions holds that $c_2 = 0$. The solution of the other differential equation (D.9) is

$$Y(x) = d_1 e^{\sqrt{\epsilon} \alpha x} + d_2 e^{-\sqrt{\epsilon} \alpha x}, \quad (D.11)$$

where the constants d_1 and d_2 are determined from the boundary conditions. Applying $T_p(x, r) = T_c$ as a boundary condition to find c_1 and using power series expansions for the exponential functions gives,

$$T_p(x, r) = T_c J_0(\alpha r) (1 + c\epsilon\alpha^2 hx) \quad (\text{D.I2})$$

with $c = q_-/q$ assumed to be constant. Moreover, assuming that α is small, then the Bessel function can be written as $J_0(\alpha r) \approx 1 - \frac{1}{4}(\alpha r)^2$. According to Bosschaart [7] typical values for α are in the order of 0.04 mm^{-2} . This value justifies the assumption that α is small and thus that the use of power-series is expected to be accurate. Now the temperature distribution can be written as,

$$T_p(x, r) = T_c \left(1 - \frac{1}{4}\alpha^2 r^2\right) (1 + c\epsilon\alpha^2 hx) \quad (\text{D.I3})$$

Rewriting in a similar form as equation (3.8) gives

$$T_p(x, r) = (T_c + \mathcal{C}r^2) (1 + c\epsilon\alpha^2 hx) \quad \text{with} \quad \mathcal{C} = -\frac{T_c}{4}\alpha^2. \quad (\text{D.I4})$$

This shows that the plate temperature is extended with a height dependent term.

Tabulated Laminar Burning Velocity Results

In this appendix the measured laminar burning velocities using the heat flux burner are listed in tables. The experimental data is presented together with the corresponding error estimates. The measurements are performed at ambient conditions unless otherwise mentioned. Pressure is $p_u = 1$ atm and unburnt gas temperature generally is $T_u = 298 \pm 1$ K.

E.1 Hydrogen-Oxygen-Nitrogen Flames

Table E.1: Experimental laminar burning velocity results using the heat flux method. The tabulated data are hydrogen-oxygen-nitrogen mixtures at $\mathcal{R}_{O_2} = 7.7 \pm 0.1\%$ with varying equivalence ratio.

$\mathcal{R}_{O_2} = 7.7\%$		continue $\mathcal{R}_{O_2} = 7.7\%$		continue $\mathcal{R}_{O_2} = 7.7\%$	
ϕ	S_L	ϕ	S_L	ϕ	S_L
	(cm/s)		(cm/s)		(cm/s)
0.65 ± 0.05	5.2 ± 0.4	1.15 ± 0.03	29.7 ± 0.2	2.10 ± 0.05	36.3 ± 0.2
0.70 ± 0.04	6.4 ± 0.4	1.20 ± 0.03	32.8 ± 0.2	2.30 ± 0.05	34.1 ± 0.1
0.75 ± 0.02	6.6 ± 0.3	1.25 ± 0.03	35.2 ± 0.1	2.30 ± 0.05	34.2 ± 0.2
0.85 ± 0.02	8.6 ± 0.3	1.30 ± 0.03	36.9 ± 0.2	2.40 ± 0.06	33.1 ± 0.1
0.90 ± 0.02	10.1 ± 0.3	1.35 ± 0.03	37.9 ± 0.2	2.50 ± 0.06	31.5 ± 0.1
0.95 ± 0.02	11.6 ± 0.9	1.40 ± 0.03	38.8 ± 0.2	2.60 ± 0.06	30.2 ± 0.2
1.00 ± 0.03	15.7 ± 0.6	1.50 ± 0.03	39.4 ± 0.2	2.70 ± 0.07	29.0 ± 0.1
1.00 ± 0.02	15.9 ± 0.3	1.60 ± 0.04	39.5 ± 0.2	2.80 ± 0.07	27.5 ± 0.2
1.05 ± 0.03	20.1 ± 0.4	1.70 ± 0.04	39.0 ± 0.3	2.90 ± 0.07	26.2 ± 0.4
1.05 ± 0.03	20.8 ± 0.4	1.70 ± 0.04	39.5 ± 0.4	3.00 ± 0.08	24.8 ± 0.3
1.10 ± 0.03	25.5 ± 0.4	1.90 ± 0.04	38.3 ± 0.2	3.10 ± 0.08	23.4 ± 0.5

Table E.2: Experimental laminar burning velocity results using the heat flux method. The tabulated data are hydrogen-oxygen-nitrogen mixtures at $\mathcal{R}_{\text{O}_2} = 10.7 \pm 0.1\%$ with varying equivalence ratio and constant equivalence ratio ($\phi = 1.06 \pm 0.02$) with varying oxygen content.

$\mathcal{R}_{\text{O}_2} = 10.7\%$		$\phi = 1.06$	
ϕ	S_L	\mathcal{R}_{O_2}	S_L
	(cm/s)	(%)	(cm/s)
0.70 ± 0.02	16.2 ± 1.6	7.0 ± 0.2	15.1 ± 1.0
0.75 ± 0.02	19.4 ± 0.6	7.5 ± 0.1	20.8 ± 0.2
0.80 ± 0.02	25.7 ± 0.4	8.0 ± 0.1	26.8 ± 0.2
0.85 ± 0.02	33.3 ± 0.2	8.8 ± 0.1	38.1 ± 0.1
0.90 ± 0.02	42.6 ± 0.2	9.0 ± 0.1	41.4 ± 0.3
0.95 ± 0.02	52.6 ± 0.3	9.3 ± 0.1	46.5 ± 0.2
		10.0 ± 0.1	58.8 ± 0.3

E.2 Methane-Hydrogen-Air Flames

Table E.3: Experimental laminar burning velocity results using the heat flux method. The tabulated data are methane-hydrogen-air mixtures at $\mathcal{R}_{\text{H}_2} = 0, 10$ and 20% with varying equivalence ratio.

$\mathcal{R}_{\text{H}_2} = 0\%$		$\mathcal{R}_{\text{H}_2} = 10\%$		$\mathcal{R}_{\text{H}_2} = 20\%$	
ϕ	S_L	ϕ	S_L	ϕ	S_L
	(cm/s)		(cm/s)		(cm/s)
0.65±0.01	12.0±0.8	0.70±0.03	19.0±0.6	0.60±0.03	11.4±1.1
0.70±0.01	16.7±0.6	0.75±0.03	23.8±0.5	0.65±0.02	16.4±0.7
0.75±0.01	21.5±0.4	0.80±0.03	28.2±0.3	0.70±0.02	21.3±0.6
0.80±0.01	25.8±0.2	0.85±0.03	32.2±0.3	0.75±0.02	26.2±0.3
0.85±0.01	29.6±0.1	0.90±0.03	35.1±0.3	0.80±0.02	30.9±0.3
0.90±0.01	32.7±0.2	0.95±0.03	37.6±0.3	0.85±0.02	34.9±0.2
0.95±0.01	34.9±0.1	1.00±0.03	39.2±0.3	0.90±0.02	37.9±0.2
1.00±0.01	36.4±0.1	1.05±0.03	40.1±0.2	0.95±0.02	40.5±0.2
1.00±0.01	36.4±0.1	1.10±0.03	40.1±0.2	1.00±0.02	42.3±0.2
1.05±0.01	37.2±0.1	1.15±0.03	38.9±0.3	1.00±0.02	42.1±0.2
1.10±0.01	37.0±0.1	1.20±0.03	36.2±0.3	1.05±0.02	43.7±0.3
1.15±0.02	35.6±0.1	1.25±0.03	31.8±0.3	1.10±0.02	43.9±0.2
1.20±0.02	32.7±0.1	1.30±0.04	26.7±0.3	1.15±0.02	42.8±0.2
1.25±0.02	28.3±0.2	1.35±0.04	20.9±0.5	1.20±0.03	40.4±0.2
1.30±0.02	23.0±0.3	1.40±0.05	17.4±0.6	1.25±0.03	36.4±0.3
1.35±0.02	18.9±0.2	1.45±0.05	14.5±0.5	1.30±0.03	30.8±0.3
1.40±0.02	15.6±0.2	1.50±0.06	12.3±0.6	1.35±0.03	24.3±0.5
1.45±0.03	13.3±0.3			1.40±0.04	19.5±0.5
1.50±0.03	11.6±0.2			1.45±0.04	16.2±0.5
				1.50±0.05	13.7±0.6

Table E.4: Experimental laminar burning velocity results using the heat flux method. The tabulated data are methane-hydrogen-air mixtures at $\mathcal{R}_{\text{H}_2} = 30$ and 40% with varying equivalence ratio.

$\mathcal{R}_{\text{H}_2} = 30\%$		$\mathcal{R}_{\text{H}_2} = 40\%$	
ϕ	S_L (cm/s)	ϕ	S_L (cm/s)
0.60±0.02	12.4±0.8	0.60±0.02	17.2±1.0
0.65±0.02	17.5±0.6	0.65±0.02	23.0±0.7
0.70±0.02	22.9±0.5	0.70±0.02	28.8±0.4
0.75±0.02	27.9±0.2	0.75±0.02	34.5±0.3
0.80±0.02	33.6±0.3	0.80±0.02	39.5±0.2
0.85±0.02	37.6±0.1	0.85±0.02	44.3±0.3
0.90±0.02	41.0±0.1	0.90±0.02	48.5±0.2
0.95±0.02	44.4±0.2	0.95±0.02	51.8±0.3
1.00±0.02	47.0±0.2	1.00±0.02	53.5±0.3
1.00±0.02	46.9±0.3	1.05±0.02	54.4±0.3
1.05±0.02	48.4±0.3	1.10±0.02	53.7±0.3
1.10±0.02	48.4±0.2	1.15±0.02	51.5±0.3
1.15±0.02	47.4±0.2	1.20±0.02	47.9±0.3
1.20±0.02	44.6±0.2	1.25±0.03	42.9±0.3
1.25±0.02	41.2±0.1	1.30±0.03	36.9±0.3
1.30±0.03	35.5±0.2	1.35±0.03	30.8±0.3
1.35±0.03	28.7±0.3	1.40±0.03	25.3±0.3
1.40±0.03	22.5±0.2	1.45±0.04	21.0±0.4
1.45±0.04	18.8±0.2	1.50±0.04	17.4±0.3
1.50±0.04	15.9±0.2	1.55±0.04	14.9±0.3
		1.60±0.05	13.2±0.2
		1.65±0.05	11.7±0.2
		1.70±0.05	10.6±0.2

E.3 Methane-Hydrogen-Air Flames at Increased Unburnt Temperature

Table E.5: Experimental laminar burning velocity results using the heat flux method. The tabulated data are methane-hydrogen-air mixtures at increased unburnt gas temperatures for equivalence ratio $\phi = 0.80 \pm 0.02$ at $\mathcal{R}_{\text{H}_2} = 0, 10, 20$ and 30% with varying equivalence ratio.

$\mathcal{R}_{\text{H}_2} = 0\%$		$\mathcal{R}_{\text{H}_2} = 10\%$		$\mathcal{R}_{\text{H}_2} = 20\%$		$\mathcal{R}_{\text{H}_2} = 30\%$	
T_u	S_L	T_u	S_L	T_u	S_L	T_u	S_L
(K)	(cm/s)	(K)	(cm/s)	(K)	(cm/s)	(K)	(cm/s)
298±1	26.1±0.2	298±1	28.1±0.2	298±1	30.6±0.1	298±1	33.6±0.3
308±1	27.4±0.3	308±1	29.5±0.2	308±1	31.8±0.2	308±1	35.1±0.1
318±1	29.1±0.2	318±1	31.0±0.2	318±1	33.5±0.3	318±1	36.9±0.2
328±1	30.6±0.2	328±1	32.7±0.2	328±1	35.4±0.2	328±1	38.9±0.1
343±1	32.9±0.6	343±1	35.9±0.5	343±1	38.6±0.9	343±1	42.4±0.7
358±1	36.3±0.6	358±1	38.7±0.5	358±1	41.8±0.9	358±1	45.7±0.7
373±1	39.2±0.5	373±1	41.8±0.6	373±1	45.1±1.0	373±1	49.3±0.6
388±1	42.3±0.6	388±1	45.1±0.5	388±1	48.6±0.9	388±1	53.1±0.9
403±1	45.4±0.5	403±1	48.5±0.5	403±1	52.2±0.8	403±1	57.1±0.7
418±1	48.8±0.6	418±1	52.0±0.6	418±1	56.1±1.0	418±1	61.4±0.8
433±1	51.6±0.6	433±1	55.5±0.6	433±1	59.3±1.0	433±1	65.6±0.8

Table E.6: Experimental laminar burning velocity results using the heat flux method. The tabulated data are methane-hydrogen-air mixtures at increased unburnt gas temperatures for equivalence ratio $\phi = 1.00 \pm 0.02$ at $\mathcal{R}_{\text{H}_2} = 0, 10, 20$ and 30% with varying equivalence ratio.

$\mathcal{R}_{\text{H}_2} = 0\%$		$\mathcal{R}_{\text{H}_2} = 10\%$		$\mathcal{R}_{\text{H}_2} = 20\%$		$\mathcal{R}_{\text{H}_2} = 30\%$	
T_u	S_L	T_u	S_L	T_u	S_L	T_u	S_L
(K)	(cm/s)	(K)	(cm/s)	(K)	(cm/s)	(K)	(cm/s)
298±1	36.4±0.1	298±1	39.1±0.1	298±1	42.1±0.2	298±1	47.0±0.2
308±1	38.4±0.1	308±1	40.7±0.1	308±1	44.2±0.1	308±1	49.5±0.2
318±1	40.2±0.1	318±1	42.8±0.1	318±1	46.4±0.3	318±1	52.0±0.2
328±1	42.1±0.3	328±1	44.8±0.1	328±1	49.0±0.2	328±1	54.7±0.5
343±1	44.9±0.5	343±1	48.1±0.5	343±1	52.9±0.4	343±1	58.5±0.4
358±1	48.9±0.5	358±1	52.8±0.4	358±1	56.5±0.4	358±1	62.9±0.5
373±1	52.4±0.5	373±1	56.0±0.4	373±1	60.5±0.4		
388±1	56.0±0.5	388±1	59.9±0.4				
403±1	59.8±0.5						

Table E.7: Experimental laminar burning velocity results using the heat flux method. The tabulated data are methane-hydrogen-air mixtures at increased unburnt gas temperatures for equivalence ratio $\phi = 0.80 \pm 0.03$ at $\mathcal{R}_{\text{H}_2} = 0, 10, 20$ and 30% with varying equivalence ratio.

$\mathcal{R}_{\text{H}_2} = 0\%$		$\mathcal{R}_{\text{H}_2} = 10\%$		$\mathcal{R}_{\text{H}_2} = 20\%$		$\mathcal{R}_{\text{H}_2} = 30\%$	
T_u	S_L	T_u	S_L	T_u	S_L	T_u	S_L
(K)	(cm/s)	(K)	(cm/s)	(K)	(cm/s)	(K)	(cm/s)
298±1	32.7±0.1	298±1	35.7±0.8	298±1	39.5±0.1	298±1	44.6±0.2
308±1	35.0±0.1	308±1	37.9±0.1	308±1	42.1±0.1	308±1	47.4±0.2
318±1	36.2±0.1	318±1	39.6±0.1	318±1	44.0±0.1	318±1	49.4±0.2
328±1	38.7±0.1	328±1	42.1±0.1	328±1	46.5±0.1	328±1	52.1±0.1
343±1	42.0±0.4	343±1	45.7±0.4	343±1	50.5±0.4	343±1	56.4±0.4
358±1	45.2±0.7	358±1	49.0±0.6	358±1	54.0±0.8	358±1	60.1±0.7
373±1	48.6±0.6	373±1	52.6±0.7	373±1	57.9±0.7		
388±1	52.0±0.7	388±1	56.3±0.8	388±1	61.9±0.9		
403±1	56.7±0.7	403±1	60.3±0.8				
418±1	59.4±0.8						

Nomenclature

Roman symbols

A_t	Area	m^2
A	Pre-exponential factor	*
\mathcal{A}_i	Symbol of species i	-
b	Reaction constant (temperature coefficient)	-
\mathcal{C}	Parabolic coefficient	K m^{-2}
c	Constant	-
c	Speed of sound	m s^{-1}
c_p	Specific heat capacity at constant pressure	$\text{J kg}^{-1} \text{K}^{-1}$
c_v	Specific heat capacity at constant volume	$\text{J kg}^{-1} \text{K}^{-1}$
d	Diameter	m
Da_j	Damköhler number of reaction j	-
D_{ij}	Binary diffusion coefficient	$\text{m}^2 \text{s}^{-1}$
E_a	Activation energy	J
g	Gravity	m s^{-2}
h	Specific enthalpy	J kg^{-1}
h	Thickness of the burner plate	m
\mathbf{I}	Unit tensor	-
K_j	Equilibrium constant of reaction j	*
$k_{j,\text{eq}}$	Equilibrium constant of reaction j	*
k_j	Reaction rate coefficient for reaction j	*
\mathcal{L}	Steady transport operator	-
Le_i	Lewis number	—
l_f	Flame thickness	m
\bar{M}	Mean molar mass	kg mol^{-1}
\dot{m}	Mass flow	$\text{kg m}^{-2} \text{s}^{-1}$
Ma	Mach number	-
M_i	Molar mass of species i	kg mol^{-1}
n_i	Concentration of species i	mol m^{-3}
N_r	Number of reactions	-
N_s	Number of species	-

p	Pitch of the burner plate	m
p	Pressure	Pa
p_{amb}	Ambient pressure	Pa
q	Heat flux	$J m^{-2} s^{-1}$
r	Radial coordinate	m
r_j	Reaction rate for reaction j	$mol m^{-3} s^{-1}$
R	Universal gas constant	$J mol^{-1} K^{-1}$
R	Radius of the burner plate	m
\mathcal{R}_{H_2}	Molil based ratio between hydrogen and methane	-
\mathcal{R}_{O_2}	Mole based ratio between oxygen and nitrogen	-
s	Relative sensitivity coefficient	-
s	Sensitivity coefficient	$K s m^{-3}$
S_L	Laminar burning velocity	$m s^{-1}$
T	Temperature	K
t	Time	s
T_c	Temperature at $r = 0$ of the burnerplate	K
T_R	Temperature of the heating jacket	K
T_u	Unburnt gas Temperature	K
\mathbf{u}	Gas mixture velocity	$m s^{-1}$
U_g	Gas velocity	$m s^{-1}$
U_i	Diffusion velocity of species i	$m s^{-1}$
u	Velocity in x-direction	$m s^{-1}$
v	Velocity in y-direction	$m s^{-1}$
w	Velocity in z-direction	$m s^{-1}$
w_j	Non-dimensionalised reaction rate	-
X_i	Species mole fraction	$mol mol^{-1}$
x_p	Downstream side of the burnerplate	m
y	Non-dimensional coordinate	-
Y_i	Species mass fraction	$kg kg^{-1}$
z	Non-dimensional coordinate	-

Greek symbols

α	Heat transfer coefficient	$J m^{-2} s^{-1} K^{-1}$
α	Ratio between CO and H ₂ , mole based	-
α	Volumetric heat transfer coefficient	$J m^{-3} s^{-1} K^{-1}$
β	Production rate ratio between CO and H ₂ at the inner layer	-
Δ	Error estimate	*
δ	Inner layer thickness	-
ϵ	Geometrical constant	-
ϵ	Oxidation layer thickness	-
η	Dynamic viscosity	$kg m^{-1} s^{-2}$
κ	Volumetric viscosity	$m^2 s$
λ'	Thermal heat conductivity	$J m^{-1} s^{-1} K^{-1}$
λ_{br}	Thermal heat conductivity of brass	$J m^{-1} s^{-1} K^{-1}$
ν	Stoichiometric coefficient	-

Π	Stress-tensor	$\text{kg m}^{-1} \text{s}^{-2}$
ρ	Density	kg m^{-3}
ρ_i	Density of species i	kg m^{-3}
σ	Uncertainty	*
ς_{ij}	Collision efficiency between species	-
τ	Scaled temperature	-
$\boldsymbol{\tau}$	Viscous stress-tensor	$\text{kg m}^{-1} \text{s}^{-2}$
ϕ	Fuel equivalence ratio	-
$\dot{\omega}_i$	Chemical source term	$\text{kg m}^{-3} \text{s}^{-1}$
$\dot{\omega}_T$	Heat release	$\text{J m}^{-3} \text{s}^{-1}$
ξ	Ratio between hydrogen and methane	-

Superscripts

0	Without hydrogen
ξ	With hydrogen
ref	Reference
\sim	Scaled value, the hydrogen value divided by the pure value
T	Transposed

Subscripts

$-\infty$	Initial
g	Adiabatic
b	Reverse reaction
c	Centre
eq	Equilibrium
f	Forward reaction
g	Gas phase
i	Species
j	Elements
k	Species
p	Burnerplate

* depends on the situation

Bibliography

- [1] Andrews, G.E. and Bradley, D., Determination of burning velocities: A critical review. *Combust. Flame* 18(1):133–153 (1961).
- [2] Aung, K.T., Hassan, M.I. and Faeth, G.M., Effects of pressure and nitrogen dilution on flame/stretch interactions of laminar premixed $H_2/O_2/N_2$ flames. *Combust. Flame* 112(1–2):1–15 (1998).
- [3] Barassin, A., R., Lisbet., Combourieu, J. and Laffitte, P., Étude de l'influence de la température initiale sur la vitesse normale de déflagration de mélanges méthane-air. *Bulletin de la Société Chimique de France* 104(7):2521–2526 (1967).
- [4] Baulch, D.L., Cobos, C.J., Cox, R.A., Esser, C., Frank, P., Just, Th., Kerr, J.A., Pilling, M.J., Troe, J., Walker, R.W. and Warnatz, J., Evaluated kinetic data for combustion modeling. *J. Phys. Chem. Ref. Data* 21:411 (1992).
- [5] Bell, S.R. and Gupta, M., Extension of the lean operating limit for natural gas fueling of a spark ignited engine using hydrogen blending. *Combust. Sci. Technol.* 123:23–48 (1997).
- [6] Bird, R.B., Stewart, W.E. and Lightfoot, E.N., Eds., *Transport Phenomena*, Wiley, New York, 1960.
- [7] Bosschaart, K.J. *Analysis of the Heat Flux Method for Measuring Burning Velocities*. Ph.D. thesis, Technische Universiteit Eindhoven, 2002.
- [8] Bosschaart, K.J. and de Goey, L.P.H., Detailed analysis of the heat-flux method for measuring burning velocities. *Combust. Flame* 132(1–2):170–180 (2003).
- [9] Bosschaart, K.J. and de Goey, L.P.H., The laminar burning velocity of flames propagating in mixtures of hydrocarbons and air measured with the heat flux method. *Combust. Flame* 136(3):261–269 (2004).
- [10] Botha, J.P. and Spalding, D.B., The laminar flame speeds of propane/air mixtures with heat extraction from the flame. *Proc. R. Soc. Lon. ser-A* 255(1160):71–95 (1954).
- [11] Bowman, C.T., Hanson, R.K., Davidson, D.F., Gardiner Jr., W.C., Lissianski, V.V., Smith, G.P., Golden, D.M., Frenklach, M. and Goldenberg, M. GRI-mech 2.11. http://www.me.berkeley.edu/gri_mech/, 1995.
- [12] Bradley, D., Gaskell, P.H., Gu, A.J., Lawes, M. and Scott, M.J., Premixed turbulent flame instability and NO formation in a lean-burn swirl burner. *Combust. Flame* 115:515–538 (1998).
- [13] Buckmaster, J.D. and Takeno, T., *Mathematical Modeling in Combustion Science*, vol. 299 of *Lecture Notes in Physics*, Springer-Verlag, New York, 1988.

- [14] Burcat, A., Third millennium ideal gas and condensed phase thermochemical database for combustion. Tech. Rep. (TAE) Report #867, Technion Aerospace Engineering, 2001. Available at: <ftp://ftp.technion.ac.il/pub/supported/aetdd/thermodynamics>.
- [15] Burwasser, H. and Pease, R.N., Burning velocities of hydrogen-air flames. *J. Am. Chem. Soc.* 77(22):5806–5808 (1955).
- [16] CHEM1D. Eindhoven University of Technology, 2002. <http://www.combustion.tue.nl/chem1d>.
- [17] Coppens, F.H.V., De Ruyck, J. and Konnov, A.A., Effects of hydrogen enrichment on adiabatic burning velocity and no formation in methane + air flames. *Exp. Therm. Fluid Sci.* 31(5):437–444 (2007).
- [18] Dagaut, P. and Nicolle, A., Experimental and detailed kinetic modeling study of hydrogen-enriched natural gas blend oxidation over extended temperature and equivalence ratio ranges. *Proc. Combust. Inst.* 30:2631–2638 (2005).
- [19] Davis, S.G. and Searby, G., The use of counterflow flames for the evaluation of burning velocities and stretch effects in hydrogen/air mixtures. *Combust. Sci. Technol.* 174:93–110 (2002).
- [20] Di Sarli, V. and Di Benedetto, A., Laminar burning velocity of hydrogen-methane/air premixed flames. *Int. J. Hydrogen Energ.* (2007). in press.
- [21] Dong, Y., Vagelopoulos, C.M., Spedding, G. and Egolfopoulos, F.N., Measurements of laminar flame speeds through digital particle image velocimetry: Mixtures of methane and ethane with hydrogen, oxygen, nitrogen, and helium. *Proc. Combust. Inst.* 29:1419–1426 (2002).
- [22] Dowdy, D.R., Smith, D.B., Taylor, S.C. and Williams, A., The use of expanding spherical flames to determine burning velocities and stretch effects in hydrogen/air mixtures. *Proc. Combust. Inst.* 23:325–332 (1990).
- [23] Dugger, G.L. and Heimel, S., Flame speeds of methane-air, propane-air, and ethylene-air mixtures at low initial temperatures. Tech. rep., NACA, 1952.
- [24] Dyakov, I.V., Konnov, A.A., de Ruyck, J., Bosschaart, K.J., Brock, E.C.M. and de Goey, L.P.H., Measurements of adiabatic burning velocity in methane-oxygen-nitrogen mixtures. *Combust. Sci. Technol.* 172:81–96 (2001).
- [25] Egolfopoulos, F.N., Cho, P. and Law, C.K., Laminar flame speeds of methane-air mixtures under reduced and elevated pressures. *Combust. Flame* 76(3–4):375–391 (1989).
- [26] Egolfopoulos, F.N. and Law, C.K., An experimental and computational study of the burning rates of ultra-lean to moderately-rich H_2 - O_2 - N_2 laminar flames with pressure variations. *Proc. Combust. Inst.* 23:333–340 (1990).
- [27] El Bakali, A., Dagaut, P., Pillier, L., Desgroux, P., Pauwels, J.-F., Rida, A. and Meunier, P., Experimental and modeling study of the oxidation of natural gas in a premixed flame, shock tube, and jet-stirred reactor. *Combust. Flame* 137(1–2) (2004).
- [28] Ern, A. and Giovangigli, V., Thermal conduction and thermal diffusion in dilute polyatomic gas mixtures. *Physica A* 214:526–546 (1995).
- [29] Ern, A. and Giovangigli, V. Eglib user manual, 1996. Available at: <http://blanche.polytechnique.fr/www.eglib>.

- [30] Evans, M.W., Current theoretical concepts of steady-state flame propagation. *Chem. Rev.* 51(3):363–429 (1952).
- [31] Fine, B., Stability limits and burning velocities of laminar hydrogen-air flames at reduced pressures. Tech. Rep. TN-3833, NACA, 1956.
- [32] Fotache, C.G., Kreutz, T.G. and Law, C.K., Ignition of hydrogen-enriched methane by heated air. *Combust. Flame* 110(4):429–440 (1997).
- [33] Frijters, P.J.M., 2006. Private Communication.
- [34] Fukutani, S. and Kunioshi, N., Fuel mixing effects on propagation of premixed flames. *B. Chem. Soc. Jpn.* 65(10):2569–2572 (1992).
- [35] de Goey, L.P.H., van Maaren, A. and Quax, R.M., Stabilization of adiabatic premixed laminar flames on a flat flame burner. *Combust. Sci. Technol.* 92:201–207 (1993).
- [36] de Goey, L.P.H., Plessing, T., Hermanns, R.T.E. and Peters, N., Analysis of the flame thickness of turbulent flamelets in the thin reaction zones regime. *Proc. Combust. Inst.* 30:859–866 (2005).
- [37] de Goey, L.P.H., Somers, L.M.T., Bosch, W.M.M.L. and Mallens, R.M.M., Modeling of small scale structure of flat burner-stabilized flames. *Combust. Sci. Technol.* 104:387–400 (1995).
- [38] Göttgens, J., Mauss, F. and Peters, N., Analytic approximations of burning velocities and flame thicknesses of lean hydrogen, methane, ethylene, ethane, acetylene, and propane flames. *Proc. Combust. Inst.* 24:129–135 (1992).
- [39] Gu, X.J., Haqa, M.Z., Lawes, M. and Woolley, R., Laminar burning velocity and markstein lengths of methane–air mixtures. *Combust. Flame* 121(1–2):41–58 (2000).
- [40] Gülder, Ö.L. Correlations of laminar combustion data for alternative S.I. engine fuels. SAE Tech. Pap. Ser. SAE 841000, 1984.
- [41] Günther, R. and Janisch, G., Measurements of burning velocity in a flat flame front. *Combust. Flame* 19(1):49–53 (1972).
- [42] Halter, F., Chauveau, C., Djebaïli-Chaumeix, N. and Gökalp, I., Characterization of the effects of pressure and hydrogen concentration on laminar burning velocities of methane-hydrogen-air mixtures. *Proc. Combust. Inst.* 30:201–208 (2005).
- [43] Haniff, M.S., Melvin, A., Smith, D.B. and Willians, A., The burning velocities of methane and SNG mixtures with air. *J. I. Energy* 62:229–236 (1989).
- [44] Hasegawa, T. and Sato, M., Study of ammonia removal from coal-gasified fuel. *Combust. Flame* 114(1–2):246–258 (1998).
- [45] Hassan, M.I., Aung, K.T. and Faeth, G.M., Measured and predicted properties of laminar premixed methane/air flames at various pressures. *Combust. Flame* 115(4):539–550 (1998).
- [46] Heimel, S., Effect of initial mixture-temperature on burning velocity of hydrogen-air mixtures with preheating and simulated preburning. Tech. Rep. TN-4156, NACA, 1957.
- [47] Herbon, J.T., Hanson, R.K., Golden, D.M. and Bowman, C.T., A shock tube study of the enthalpy of formation of OH. *Proc. Combust. Inst.* 29:1201–1208 (2002).
- [48] Hermanns, R.T.E., Konnov, A.A., Bastiaans, R.J.M. and de Goey, L.P.H., Laminar burning velocities of diluted hydrogen-oxygen-nitrogen mixtures. *Energy and Fuels* (2007). accepted.
- [49] Hi-Tec, Bronkhorst. Polynomial calibration, 1999.

- [50] Hi-Tec, Bronkhorst. <http://www.bht.nl>, 2006.
- [51] Hirschfelder, J.O., Curtiss, C.F. and Bird, R.B., Eds., *Molecular Theory of Gases and Liquids*, Wiley, New York, 1964.
- [52] Huang, Z., Zhang, Y., Zeng, A., Wang, Q. and Jiang, D., Measurements of laminar burning velocities for natural gas–hydrogen–air mixtures. *Combust. Flame* 146(1–2):302–311 (2006).
- [53] Hughes, K.J., Turanyi, T. and Pilling, M.J. Leeds methane oxidation mechanism version 1.5. <http://garfield.chem.elte.hu/Combustion/methane.htm>, 2001.
- [54] Iijima, T. and Takeno, T., Effects of temperature and pressure on burning velocity. *Combust. Flame* 65(1):35–43 (1986).
- [55] Jahn, G. In *Combustion Flames and Explosions of Gases*, Lewis, B. and von Elbe, G., Eds., 2nd ed. Academic Press, 1961, pp. 381–389.
- [56] Joens, J.A., The dissociation energy of OH(X_{23/2}) and the enthalpy of formation of OH(X_{23/2}), ClOH, and BrOH from thermochemical cycles. *J. Phys. Chem. A* 105:11041–11044 (2001).
- [57] Karim, G.A., Wierzba, I. and Al-Alousi, Y., Methane hydrogen mixtures as fuels. *Int. J. Hydrogen Energ.* 21(7):625–631 (1996).
- [58] Karpov, V.P., Lipatnikov, A.N. and Wolanski, P., Finding the markstein number using the measurements of expanding spherical laminar flames. *Combust. Flame* 109(3):436–448.
- [59] Kobayashi, H., Kawabata, Y. and Maruta, K., Experimental study on general correlations of turbulent burning velocity at high pressure. *Proc. Combust. Inst.* 27:941–948 (1998).
- [60] Konnov, A.A. Detailed reaction mechanism for small hydrocarbons combustion. <http://homepages.vub.ac.be/~akonnov/>, 2000. version 0.5.
- [61] Konnov, A.A., Refinement of the kinetic mechanism of hydrogen combustion. *Khim. Fiz.* 23(8):5–18 (2004).
- [62] Konnov, A.A. and de Ruyck, J., Impact of the lower enthalpy of formation of OH radical on NO formation in flames of hydrogen and air. In *Proceedings of the 17th Symposium on Gas Kinetics* (2002), University of Essen. Pap. CP16.
- [63] Konnov, A. A. and Dyakov, I. V. and, Measurement of propagation speeds in adiabatic cellular premixed flames of CH₄ + O₂ + CO₂. *Exp. Therm. Fluid Sci.* 29(8):901–907 (2005).
- [64] Kuo, K.K., *Principles of Combustion*, 2nd ed., John Wiley & Sons, Inc., Hoboken, New Jersey, 2005.
- [65] Kwon, O.C. and Faeth, G.M., Flame/stretch interactions of premixed hydrogen-fueled flames: Measurements and predictions. *Combust. Flame* 124(4):590–610 (2001).
- [66] Law, C.K., A compilation of experimental data on laminar burning velocities. In *Reduced Kinetic Mechanisms for Applications in Combustion Systems*, Peters, N. and Rogg, B., Eds., vol. 15 of *Lecture Notes in Physics*. Springer-Verlag, 1993, pp. 19–31.
- [67] Law, C.K., 2003. Personal communication.
- [68] Li, J., Zhao, Z., Kazakov, A. and Dryer, F.L., An updated comprehensive kinetic model of hydrogen combustion. *Int. J. Chem. Kinet.* 36(10):566–575 (2004).

- [69] Lifshitz, A., Scheller, K., Burcat, A. and Skinner, G.B., Shock-tube investigation of ignition in methane-oxygen-argon mixtures. *Combust. Flame* 16(3):311–321 (1971).
- [70] Lipatnikov, A.N. and Chomiak, J., Turbulent flame speed and thickness: phenomenology, evaluation, and application in multi-dimensional simulations. *Prog. Energ. Combust.* 28:1–74 (2002).
- [71] Liu, D.D.S. and MacFarlane, R., Laminar burning velocities of hydrogen-air and hydrogen-air-steam flames. *Combust. Flame* 49(1–3):59–71 (1983).
- [72] van Maaren, A. *One-step chemical reaction parameters for premixed laminar flames*. Ph.D. thesis, Technische Universiteit Eindhoven, 1994.
- [73] van Maaren, A. and de Goey, L.P.H., Laser doppler thermometry in flat flames. *Combust. Sci. Technol.* 99:105–118 (1994).
- [74] van Maaren, A. and de Goey, L.P.H., Stretch and the adiabatic burning velocity of methane- and propane-air flames. *Combust. Sci. Technol.* 102(1–6):309–314 (1994).
- [75] Manton, J. and Milliken, B.B. In *Proceedings of the Gas Dynamics Symposium (Aerothermochem.)* (1955), p. 151.
- [76] Metghalchi, M. and Keck, J.C., Laminar burning velocity of propane-air mixtures at high temperature and pressure. *Combust. Flame* 38(1):143–154 (1980).
- [77] Mueller, M.A., Kim, T.J., Yetter, R.A. and Dryer, F.L., Flow reactor studies and kinetic modeling of the H_2/O_2 reaction. *Int. J. Chem. Kinet.* 31(2):113–125 (1999).
- [78] Ó Conaire, M., Curran, H.J., Simmie, J.M., Pitz, W.J. and Westbrook, C.K., A comprehensive modeling study of hydrogen oxidation. *Int. J. Chem. Kinet.* 36(11) (2004).
- [79] Peters, N., Numerical and asymptotic analysis of systematic reduced reaction schemes for hydrocarbon flames. In *Numerical Simulation of Combustion Phenomena*, Glowinski, R., Larrouturou, B., and Temam, R., Eds., vol. 241 of *Lecture Notes in Physics*. Springer-Verlag, 1985, pp. 90–109.
- [80] Peters, N., *Fifteen Lectures on Laminar and Turbulent Combustion*, Ercoftac lecture notes, Ercoftac, 1992.
- [81] Peters, N., *Turbulent Combustion*, Cambridge University Press, 2000.
- [82] Peters, N. and Williams, F.A., The asymptotic structure of stoichiometric methane-air flames. *Combust. Flame* 68(2):185–207 (1987).
- [83] Petrova, M.V. and Williams, F.A., A small detailed chemical-kinetic mechanism for hydrocarbon combustion. *Combust. Flame* 144(3):526–544 (2006).
- [84] Pitsch, H., Peters, N. and Seshadri, K., Numerical and asymptotic studies of the structure of premixed iso-octane flames. *Proc. Combust. Inst.* 26:763–771 (1996).
- [85] Poinso, T. and Veynante, D., *Theoretical and Numerical Combustion*, Edwards, Philadelphia, 2001.
- [86] Powling, J., A new burner method for the determination of low burning velocities and limits of inflammability. *Fuel* 28(2):25–28 (1949).
- [87] Ren, J.-Y., Qin, W., Egolfopoulos, F.N., Mak, H. and Tsotsis, T.T., Methane reforming and its potential effect on the efficiency and pollutant emissions of lean methane-air combustion. *Chemical Engineering Science* 56:1541–1549 (2001).
- [88] Ruscic, B., Feller, D., Dixon, D.A., Peterson, K.A., Harding, L.B., Asher, R.L. and Wagner, A.F., Evidence for a lower enthalpy of formation of hydroxyl radical and a lower gas-phase bond dissociation energy of water. *J. Phys. Chem. A* 105:1–4 (2001).

- [89] Scholte, T.G. and Vaags, P.B., The burning velocity of hydrogen-air mixtures and mixtures of some hydrocarbons with air. *Combust. Flame* 3:495–501 (1959).
- [90] van den Schoor, F., Hermanns, R.T.E., van Oijen, J.A., Verplaetsen, F. and de Goey, L.P.H., Comparison and evaluation of methods for the calculation of flammability limits, applied to methane/hydrogen/air mixtures. *Journal of Hazardous Materials* (2007). accepted.
- [91] Seshadri, K., Bai, X. S., Pitsch, H. and Peters, N., Asymptotic analysis of the structure of moderately rich methane-air flames. *Combust. Flame* 113(4):589–602 (1998).
- [92] Seshadri, K., Bollig, M. and Peters, N., Numerical and asymptotic studies of the structure of stoichiometric and lean premixed heptane flames. *Combust. Flame* 108(4):518–536 (1997).
- [93] Seshadri, K. and Peters, N., The inner structure of methane-air flames. *Combust. Flame* 81(2):96–118 (1990).
- [94] Seshadri, K., Peters, N. and Williams, F.A., Asymptotic analyses of stoichiometric and lean hydrogen-air flames. *Combust. Flame* 96(4):407–427 (1994).
- [95] Simmie, J.M., Detailed chemical kinetic models for the combustion of hydrocarbon fuels. *Prog. Energ. Combust.* 29(6) (2003).
- [96] Skreiberg, Ø., Kilpinen, P. and Glarborg, P., Ammonia chemistry below 1400 K under fuel-rich conditions in a flow reactor. *Combust. Flame* 136(4):501–518 (2004).
- [97] Smith, G.P., Golden, D.M., Frenklach, M., Moriarty, N.W., Eiteneer, B., Goldenberg, M., Bowman, C.T., Hanson, R.K., Song, S., Gardiner Jr., W.C., Lissianski, V.V. and Qin, Z. GRI-mech 3.0. http://www.me.berkeley.edu/gri_mech/, 2000.
- [98] Smooke, M.D. In *Reduced Kinetic Mechanisms and Asymptotic Approximations for Methane-Air Flames*, Smooke, M.D., Ed., vol. 384 of *Lecture Notes in Physics*. Springer-Verlag, 1991, p. 23.
- [99] Smooke, M.D., Miller, J.A. and Kee, R.J., Determination of adiabatic flame speeds by boundary value methods. *Combust. Sci. Technol.* 34:79–90 (1983).
- [100] Somers, L.M.T. *The Simulation of Flat Flames with Detailed and Reduced Chemicals Models*. Ph.D. thesis, Technische Universiteit Eindhoven, 1994.
- [101] Sonnemans, P.J.M. *Application of body-fitted-coordinates in heat conduction problems*. Ph.D. thesis, Technische Universiteit Eindhoven, 1992.
- [102] Stull, D.R. and Prophet, H., Eds., *JANAF thermochemical tables*, vol. 37, NSRDS-NBS, Washington, 1971.
- [103] Tanoue, K., Goto, S., Shimada, F. and Hamatake, T. *Trans. Jpn. Soc. Mech. Eng. B* 69:162–168 (2003).
- [104] Tse, S.D., Zhu, D.L. and Law, C.K., Morphology and burning rates of expanding spherical flames in H₂/O₂/inert mixtures up to 60 atmospheres. *Proc. Combust. Inst.* 28:1793–1799 (2000).
- [105] Vagelopoulos, C.M. and Egolfopoulos, F.N., Direct experimental determination of laminar flame speeds. *Proc. Combust. Inst.* 27:513–519 (1998).
- [106] Vagelopoulos, C.M., Egolfopoulos, F.N. and Law, C.K., Further considerations on the determination of laminar flame speeds with the counterflow twin-flame technique. *Proc. Combust. Inst.* 25:1341–1347 (1994).

- [107] Verhelst, S., Woolley, R., Lawes, M. and Sierens, R. and, Laminar and unstable burning velocities and markstein lengths of hydrogen–air mixtures at engine-like conditions. *Proc. Combust. Inst.* 30:209–216 (2005).
- [108] Warnatz, J., Concentration-, pressure-, and temperature-dependence of the flame velocity in hydrogen-oxygen-nitrogen mixtures. *Combust. Sci. Technol.* 26:203–213 (1981).
- [109] Warnatz, J. In *Combustion Chemistry*, Gardiner, W.C., jr., Ed. Springer-Verlag, 1984, pp. 167–360.
- [110] Warnatz, J., Maas, U. and Dibble, R.W., *Combustion*, Springer, 1997.
- [111] Wilke, C.R., A viscosity equation for gas mixtures. *Journal of Chemical Physics* 18:217 (1950).
- [112] Williams, F.A., Elementary derivation of the multicomponent diffusion equation. *Amer. J. Phys.* 26:467–469 (1958).
- [113] Williams, F.A., *Combustion Theory*, Addison-Wesley Publishing Company, 1985.
- [114] Williams, F.A., Overview of asymptotics for methane flames. In *Reduced Kinetic Mechanisms and Asymptotic Approximations for Methane-Air Flames*, Smooke, M.D., Ed., vol. 384 of *Lecture Notes in Physics*. Springer-Verlag, 1991, pp. 68–85.
- [115] Wu, C.K. and Law, C.K., On the determination of laminar flame speeds from stretched flames. *Proc. Combust. Inst.* 22:1941–1949 (1984).
- [116] Yu, G., Law, C.K. and Wu, C.K., Laminar flame speeds of hydrocarbon + air mixtures with hydrogen addition. *Combust. Flame* 63(3):339–347 (1986).

Abstract

In a future sustainable society, hydrogen is likely to play an important role as an energy carrier. In an EET-project called *Greening of Gas* (VG²) the transition path from pure natural gas towards the use of mixtures containing more and more hydrogen is investigated. The research carried out at the TU/e is focused on the safety of burner devices. A crucial parameter for the safety of burner devices is the laminar burning velocity. In this thesis the laminar burning velocity of methane-hydrogen mixtures is experimentally determined and compared to numerical data using several combustion reaction mechanisms. An asymptotic theory for stoichiometric methane hydrogen flames is presented. This theory is validated with the experimental and numerical data.

To measure the laminar burning velocity accurately the heat flux burner is used, which is developed previously at TU/e. Based on the earlier works of van Maaren and Bosschaart the heat flux method is further analysed in this thesis. This analysis results in a better understanding of several aspects of the method. For example it is shown that the influence of the heating jacket is negligible when using a temperature difference of at least 30 K between the unburnt gas temperature and the temperature of the heating jacket should be maintained. Furthermore, it is not likely that the burner surface influences the heat flux experiments in the presented measurement range. However when higher unburnt gas temperatures will be used this influence should be regarded.

In the present research, three sets of laminar adiabatic burning velocities have been measured and presented using 95% confidence error intervals. The first set consists of hydrogen-oxygen-nitrogen mixtures at various fuel equivalence ratios and several nitrogen dilutions. The second set of measurements deals with methane-hydrogen-air mixtures at various fuel equivalence ratios and hydrogen contents up to 40%. The last set of measurements show a glimpse towards gas turbine situations. Here the unburnt gas temperature is increased from 298 K up to 420 K for methane-hydrogen-air mixtures.

The laminar burning velocity measurement data of hydrogen-oxygen-nitrogen mixtures, show significant differences with experimental results of other authors. This discrepancy is probably related to the non-linear stretch correction performed by them. The differences between the combustion reaction mechanisms and the heat flux data show significant differences in the performance of the methane based combustion reaction mechanisms in the case of hydrogen-oxygen-nitrogen mixtures. Especially the commonly used GRI-mechanism deviates from the experimental data. Remarkably the performance of the methane based SKGo3 mechanism is comparable or even better compared to

hydrogen based mechanisms for fuel lean flames to slightly rich hydrogen-oxygen-nitrogen flames. Generally, the hydrogen based kinetic mechanisms perform quite well for the investigated parameter range; especially the Konnov mechanism.

When comparing the measurements of the laminar burning velocities at ambient conditions as well as increased unburnt gas temperatures of methane-hydrogen-air mixtures with numerical combustion mechanisms it is shown that both the SKGo₃ mechanism and the GRI-mechanism perform very well. Experimental data of the laminar burning velocities of methane-air flames show that the measurements of Bosschaart give comparable results with the present measurements. Regrettably experimental data of methane-hydrogen-air flames is scarce; the data of Halter et al. show comparable results.

In order to get more insight in the basic properties describing methane-hydrogen-air flames, the asymptotic theory of Peters and Williams for stoichiometric methane-air flames is adapted to stoichiometric methane-hydrogen-air flames. This theory is validated both with experiments performed using the heat flux burner and numerical simulations using CHEM1D. With this theory for stoichiometric flames the laminar burning velocity as a function of the hydrogen content can be predicted qualitatively even for higher pressures and temperatures. The resulting equations show that the driving force for the increase in burning velocity of a methane-hydrogen flame is the increase in temperature difference between the inner layer temperature and the adiabatic flame temperature.

Samenvatting

In het toewerken naar een duurzame energievoorziening kan in de toekomst een energiedrager op basis van waterstof een belangrijke rol gaan spelen. In het EET-project *Vergroening van Gas* (VG^2) wordt de transitie van het huidige aardgas naar mengsels met meer en meer waterstof onderzocht. Het onderzoek aan de TU/e is gericht op de veiligheid van brander systemen. Een belangrijke parameter voor de veiligheid van brander systemen is de laminaire verbrandingssnelheid. In dit proefschrift is de laminaire verbrandingssnelheid van methaan-waterstof mengsels experimenteel bepaald en vergeleken met numerieke resultaten. Deze numerieke resultaten zijn bepaald zijn met behulp van diverse verbrandings reaktiemechanismen. Tevens is een asymptotische theorie voor stoichiometrische methaan-waterstof mengsels gepresenteerd in dit proefschrift. Deze theorie is vervolgens gevalideerd met behulp van experimentele en numerieke resultaten.

Om de laminaire verbrandingssnelheid nauwkeurig te bepalen, wordt gebruik gemaakt van een warmte flux brander. De brander is de afgelopen jaren reeds ontwikkeld aan de TU/e door van Maaren en Bosschaart. In dit proefschrift is de warmte flux methode verder geanalyseerd, wat geresulteerd heeft in een beter begrip van diverse aspecten van de meetmethode. Zo is de invloed van de verwarmingsring op de meetresultaten bijvoorbeeld verwaarloosbaar klein indien het temperatuur verschil tussen de verwarmingsring en het onverbrande gas minimaal 30 K bedraagt. Tevens is het onwaarschijnlijk dat het branderplaatje de metingen van de warmte flux brander beïnvloedt voor het gepresenteerde meetgebied in dit proefschrift. In het geval dat hogere onverbrande gastemperaturen gebruikt gaan worden, moet wel rekening gehouden worden met een eventuele invloed van de branderplaat.

In deze studie zijn drie groepen metingen verricht van laminaire verbrandingssnelheden met 95% betrouwbaarheidsinterval. De eerste groep metingen bestaat uit waterstof-zuurstof-stikstof mengsels voor verschillende brandstof-lucht verhoudingen en diverse stikstof gehalten. De tweede groep metingen zijn methaan-waterstof-lucht mengsels voor diverse brandstof-lucht verhoudingen en diverse waterstof percentages; tot 40%. De laatste groep metingen bestaat ook uit methaan-waterstof-lucht vlammen, maar nu lijken de meetcondities meer op gasturbine situaties; de onverbrande gastemperatuur is van 298 K verhoogd naar 420 K.

De meetresultaten van de laminaire verbrandingssnelheid voor waterstof-zuurstof-stikstof vlammen laten significante verschillen zien ten opzichte van experimentele

gegevens van andere auteurs. Dit verschil is waarschijnlijk veroorzaakt doordat een niet-lineaire krommingscorrectie is gebruikt door de betreffende auteurs. De verbrandings reactiemechanismen laten in vergelijking tot de metingen met de warmte flux methode significante verschillen zien voor waterstof-zuurstof-stikstof mengsels in het gedrag; met name de op methaan gebaseerde verbrandings mechanismen. Vooral het veel gebruikte GRI-mechanisme wijkt af van de metingen. Het gedrag van het op het methaan gebaseerde SKGo₃ mechanisme is vergelijkbaar en soms zelfs beter dan de op waterstof gebaseerde mechanismen; vooral in het gebied van brandstof arme vlammen tot licht brandstof rijke vlammen. In het algemeen geldt dat mechanismen die op waterstof gebaseerd zijn best goede resultaten geven in het onderzochte meetgebied; vooral het Konnov mechanisme is hiervoor geschikt.

Wanneer de metingen van de laminaire verbrandingssnelheid onder omgevings condities en de metingen voor verhoogde onverbrande gastemperatuur van methaan-waterstof-lucht mengsels worden vergeleken met numerieke resultaten met verbrandings mechanismen dan blijkt dat zowel het SKGo₃ mechanisme als het GRI-mechanisme goede resultaten geven. De gemeten verbrandingssnelheden van methaan-lucht mengsels zijn vergelijkbaar met de metingen van Bosschaart. Metingen aan methaan-waterstof-lucht vlammen zeldzaam tot nu toe, maar de in dit proefschrift gepresenteerde metingen komen overeen met de beschikbare data van Halter e.a..

Om meer inzicht te verkrijgen in de eigenschappen die een methaan-waterstof-lucht vlam beïnvloeden is de asymptotische theorie voor stoichiometrische methaan-lucht vlammen van Peters en Williams aangepast voor stoichiometrische methaan-waterstof-lucht vlammen. Deze theorie is gevalideerd met experimenten uitgevoerd met de warmte flux brander en numerieke resultaten bepaald met CHEM1D. Met deze theorie is het mogelijk om de laminaire verbrandingssnelheid als een functie van het waterstofpercentage kwalitatief te voorspellen; zelfs voor hogere drukken en onverbrande gastemperaturen. De resulterende set vergelijkingen laat zien dat de drijvende kracht achter de toename van de laminaire verbrandingssnelheid van methaan-waterstof-lucht vlammen het grotere verschil in temperatuur tussen de *inner layer* temperatuur en de adiabatische vlam temperatuur is.

Curriculum Vitae

Roy Hermanns was born in Beesel on March 12th 1973. From 1985 until 1991 he attended Hoger Algemeen Voortgezet Onderwijs (HAVO). After that, he studied Applied Physics at the Hogeschool Eindhoven. In his third year of this study he stayed one year in Germany at the Hochschule für Technik und Wirtschaft in Mittweida. In 1997 he did his bachelors' project at Philips Natlab. After receiving his bachelors' degree, Roy started working in the group of prof.dr.ir. A.A. van Steenhoven at the Faculty of Mechanical Engineering of Eindhoven University of Technology. In 2002 Roy started as a Ph.D student supervised by dr.ir. R.J.M. Bastiaans in the group Combustion Technology of prof.dr. L.P.H. de Goey. During his Ph.D project Roy presented results at international conferences in Aachen (Germany, 2003), Louvain-La-Neuve (Belgium, 2004), Montréal (Canada 2005), Heidelberg (Germany, 2006). In 2007 Roy started working at the Oel-Wärme-Institut gGmbH (OWI) Herzogenrath in Germany.

List of Publications

Journal Publications Related To This Thesis

- 1 Hermanns, R.T.E., Konnov, A.A., Bastiaans, R.J.M., and de Goey, L.P.H., Laminar Burning Velocities of Diluted Hydrogen-Oxygen-Nitrogen Mixtures, *Energ. Fuel.* 21(4):1977-1981 (2007).
- 2 van den Schoor, F., Hermanns, R.T.E., van Oijen, J.A., Verplaetsen, F., and de Goey, L.P.H., Comparison and evaluation of methods for the calculation of flammability limits, applied to methane/hydrogen/air mixtures, *J. Hazard. Mater.* (Accepted 2007).
- 3 de Goey, L.P.H., Hermanns, R.T.E. and Bastiaans, R.J.M., Analysis of the asymptotic structure of stoichiometric premixed CH₄-H₂-air flames, *Proc. Combust. Inst.* 31:1031-1038 (2006).

Other Journal Publications

- 1 de Goey, L.P.H., Plessing, T., Hermanns, R.T.E., Peters, N., Analysis of the flame thickness of turbulent flamelets in the thin reaction zones regime. *Proc. Combust. Inst.* 30:859–866 (2005).
- 2 Evertsen, R., van Oijen, J.A., Hermanns, R.T.E., de Goey, L.P.H., ter Meulen, J.J., Measurements of the absolute concentration of HCO and rCH_2 in a premixed atmospheric flat flame by cavity ring-down spectroscopy, *Combust. Flame* 135(1):57–64 (2003).
- 3 Evertsen, R., van Oijen, J.A., Hermanns, R.T.E., de Goey, L.P.H., ter Meulen, J.J., Measurements of absolute concentrations of CH in a premixed atmospheric flat flame by cavity ring-down spectroscopy, *Combust. Flame* 132(1):34–42 (2003).

Refereed Proceedings

- 1 Hermanns, R.T.E., Bastiaans, R.J.M., de Goey, L.P.H., Burning Velocities of Stoichiometric Methane-Hydrogen-Air Flames at Gasturbine Like Conditions. In *20th ICDEERS* (2005), Shepherd, J., Ed., Montréal, Canada, Paper 117.
- 2 Hermanns, R.T.E., Bastiaans, R.J.M., de Goey, L.P.H., Asymptotic Analysis of Methane-Hydrogen-Air Mixtures. In *Proc. of the European Combustion Meeting* (2005), Vandooren, J., Ed., Louvain-La-Neuve, Belgium, Paper 87.
- 3 Hermanns, R.T.E., Bastiaans, R.J.M., de Goey, L.P.H., Analysis of the laminar burning velocity of methane-hydrogen-air mixtures. In *18th Journées d'Etudes* (2004), Vandooren, J., Ed., Louvain-La-Neuve, Belgium, 3p.
- 4 Hermanns, R.T.E., Bastiaans, R.J.M., de Goey, L.P.H., Laminar burning velocities of hydrogen-oxygen-nitrogen mixtures. In *Proc. of the European Combustion Meeting* (2003), Chauveau, C. and Vovelle, C., Eds., Orleans, France, paper 121.
- 5 Hermanns, R.T.E., Bastiaans, R.J.M., de Goey, L.P.H., Laminar burning velocities of methane-hydrogen-air mixtures. In *Third European Conference on Small Burner Technology and Heating Equipment* (2003), Koehne and Lucka, Eds., pp. 240–247.
- 6 Lycklama à Nijeholt, J.A., Komen, E.M.J., Hermanns, R.T.E., de Goey, L.P.H., van Beek, M.C., Verhage, A.J.L., CFD modelling of biogas cofiring in a gasturbine. In *Proc. of the ASME Turboexpo 2002 47th Int. Gas Turbine and Aerospace Technical Congress* (2002), Benvenuti, E., Ed., Amsterdam, Netherlands.

Dankwoord

Tijdens de afgelopen jaren van mijn promotie hebben vele mensen mij geholpen bij mijn onderzoek. Een aantal van hen wil ik hier speciaal bedanken. Allereerst natuurlijk Prof.dr. Philip de Goey jou wil ik speciaal bedanken voor het meedenken, het klaar staan, en alle steun. En daarbij denk ik ook aan alle vertrouwen en 'regel-moeite' bij de start van mijn promotie. Dr.ir. Rob Bastiaans, soms in het 'altijd zonnige Californië', maar altijd bereid om samen te puzzelen. Jou uitdagende vragen zal ik ook niet snel vergeten: dankje! Bovendien wil ik jullie beide, én Prof.dr.ir. Schouten, Prof.dr. Levinsky, Prof.dr. Gökalp, bedanken voor het proeflezen en van mijn proefschrift.

Mijn onderzoek maakt deel uit van het project *Vergroening van Gas* met diverse partners uit verschillende vakgebieden. Ik heb erg genoten van de 'scenario-vergaderingen' met jullie: leuk om samen een blik te werpen op een toekomst met waterstof.

Het onderzoek is uitgevoerd binnen de divisie Thermal Fluids Engineering van de faculteit Werktuigbouwkunde aan de Technische Universiteit Eindhoven. Aan de medewerkers van deze divisie: heel erg bedankt voor de prettige sfeer en gezelligheid de afgelopen jaren. Ook mijn teamgenoten van het voetbalteam 'Vlammen Maar'; dank voor de leuke wedstrijden en de interessante nabesprekingen ☺.

Een speciaal woord voor jou Jeroen, je stond altijd klaar om dingen helder uit te leggen en natuurlijk wil ik je ook bedanken voor de fijne samenwerking de afgelopen jaren bij de ontwikkeling van CHEM1D. En Karel-Joop, je hebt me in korte tijd geleerd om de heat flux brander goed onder controle te krijgen: op deze manier verliep het begin van mijn promotie meteen vloeiend.

Geert-Jan, Gerard, Gerard, Henri en Peter zonder jullie zou het onmogelijk zijn om de experimenten in het lab zo precies uit te voeren. Verbazingwekkend wat jullie kunnen maken, ik denk dan bijvoorbeeld aan het lijmen van de heel dunne thermokoppels in de kleine gaatjes van de branderplaatjes. Tja en Edwin jij erg bedankt voor de hulp bij het opbouwen en gereedmaken van het nieuwe branderlab. Op deze manier zijn mijn metingen toch nog redelijk op tijd voltooid.

En natuurlijk ook een bedankje voor mijn stagiairs en afstudeerders: Dana, Erik, Jappe, Jeroen, Johan, Maarten, Marco, Mariska, Michiel, Oliver, Stanley, Stephan en Ton. Jullie hebben me op allerlei terreinen ontzettend veel geholpen (en werk bezorgd ☺). Johan, jou wil ik speciaal bedanken voor je inspanningen bij het aanpassen van de meetopstelling.

en natuurlijk ook voor de eerste meetresultaten.

In de afgelopen 10 jaar aan de universiteit heb ik inmiddels aardig wat kamergenoten 'versleten': Jan, Marcus, Hans, Arief, Robert en Xander. Jullie allen wil ik bedanken voor de leuke tijd die we samen doorgebracht hebben. En natuurlijk ook mijn nieuwe collega's bij OWI; voor de mogelijkheid om dit proefschrift af te kunnen ronden.

En tenslotte wil ik Marja speciaal bedanken voor alle steun, begrip en hulp. Je weet uit eigen ervaring wat er allemaal bij komt kijken bij een promotieonderzoek! Zonder jou zou ik deze stap misschien niet eens gemaakt hebben.

Bedankt allemaal!

Roy Hermanns, september 2007.